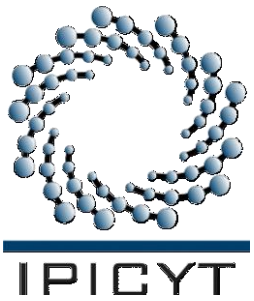

INSTITUTO POTOSINO DE INVESTIGACIÓN CIENTÍFICA Y TECNOLÓGICA, A.C.

POSGRADO EN CIENCIAS EN BIOLOGIA MOLECULAR

Carbon nanomaterials: biocompatibility and reinforcement material for 3D bioprinting ink

Tesis que presenta

José Gil Munguía López

Para obtener el grado de

Doctor en Ciencias en Biología Molecular

Director de la Tesis:

Dr. Antonio De León Rodríguez

San Luis Potosí, S.L.P., Enero de 2017

IPICYT

Constancia de aprobación de la tesis

La tesis ***"Carbon nanomaterials: biocompatibility and reinforcement material for 3D bioprinting ink"*** presentada para obtener el Grado de Doctor en Ciencias en Biología Molecular fue elaborada por **José Gil Munguía López** y aprobada el **diecinueve de enero del dos mil diecisiete** por los suscritos, designados por el Colegio de Profesores de la División de Biología Molecular del Instituto Potosino de Investigación Científica y Tecnológica, A.C.

Dr. Antonio de León Rodríguez
Director de la tesis

Dra. Ana Paulina Barba de la Rosa
Miembro del Comité Tutoral

Dra. María del Carmen González Castillo
Miembro del Comité Tutoral

Dr. Carlos Barajas López
Miembro del Comité Tutoral

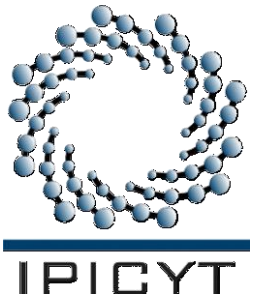

Créditos Institucionales

Esta tesis fue elaborada en el Laboratorio de Bioingeniería y Biotecnología Molecular de la División de Biología Molecular y el Laboratorio de Nanoestructuras de Carbono de la División de Materiales avanzados del Instituto Potosino de Investigación Científica y Tecnológica, A.C., bajo la dirección del Dr. Antonio De León Rodríguez.

Asimismo, parte de este trabajo fue realizado en el Department of Bioengineering, McGill University, bajo la supervisión del Prof. Joseph Matt Kinsella.

Durante la realización del trabajo el autor recibió una beca académica del Consejo Nacional de Ciencia y Tecnología (No. 250279), becas mixtas CONACYT (No. 290936) y del Instituto Potosino de Investigación Científica y Tecnológica, A.C.

IPICYT

Instituto Potosino de Investigación Científica y Tecnológica, A.C.

Acta de Examen de Grado

El Secretario Académico del Instituto Potosino de Investigación Científica y Tecnológica, A.C., certifica que en el Acta 090 del Libro Primero de Actas de Exámenes de Grado del Programa de Doctorado en Ciencias en Biología Molecular está asentado lo siguiente:

En la ciudad de San Luis Potosí a los 19 días del mes de enero del año 2017, se reunió a las 12:00 horas en las instalaciones del Instituto Potosino de Investigación Científica y Tecnológica, A.C., el Jurado integrado por:

Dr. Carlos Barajas López	**Presidente**	**IPICYT**
Dra. María del Carmen González Castillo	**Secretaria**	**UASLP**
Dra. Ana Paulina Barba de la Rosa	**Sinodal**	**IPICYT**
Dr. Antonio De León Rodríguez	**Sinodal**	**IPICYT**

a fin de efectuar el examen, que para obtener el Grado de:

DOCTOR EN CIENCIAS EN BIOLOGÍA MOLECULAR

sustentó el C.

José Gil Munguía López

sobre la Tesis intitulada:

Carbon nanomaterials: biocompatibility and reinforcement material for 3D bioprinting ink

que se desarrolló bajo la dirección de

Dr. Antonio De León Rodríguez

El Jurado, después de deliberar, determinó

APROBARLO

Dándose por terminado el acto a las 13:50 horas, procediendo a la firma del Acta los integrantes del Jurado. Dando fe el Secretario Académico del Instituto.

A petición del interesado y para los fines que al mismo convengan, se extiende el presente documento en la ciudad de San Luis Potosí, S.L.P., México, a los 19 días del mes de enero de 2017.

Dr. Horacio Flores Zúñiga
Secretario Académico

Mtra. Ivonne Lizette Cuevas Vélez
Jefa del Departamento del Posgrado

INSTITUTO POTOSINO DE INVESTIGACIÓN CIENTÍFICA Y TECNOLÓGICA, A.C.
IPICYT
SECRETARIA ACADEMICA

Dedicatorias

A mis padres
Donato Munguía Andrade
Yolanda López Cueva

A mis hermanas
Araceli Berenice Munguía López
Adriana Lorena Munguía López

A mis sobrinos, Jonathan, Ditzia y Fernando

A Alma Yadira Covarrubias de la Mora

A todos mis amigos de todas las etapas de mi vida…

Por haberme acompañado en los buenos y malos ratos de la vida.

Agradecimientos

A mi director de tesis el Dr. Antonio De León Rodríguez por compartir sus conocimientos, disponibilidad, apoyo y asesoría que me brindó durante la realización de este trabajo.

A la Dra. Ana Paulina Barba de la Rosa, Dra. María del Carmen González Castillo y al Dr. Carlos Barajas López por sus valiosas aportaciones para mejorar el presente trabajo.

Al Dr. Emilio Muñoz Sandoval por su valiosa asesoría y ayuda en la producción de nanomateriales para el presente trabajo y además por sus grandiosos comentarios.

A Leandro Gabriel Ordoñez Acevedo y Víctor Emmanuel Balderas Hernández por su gran apoyo técnico, disponibilidad y facilidades otorgadas.

Al Profesor Joseph Matt Kinsella por recibirme con los brazos abiertos en su laboratorio durante mi estancia doctoral, sus comentarios y todo el apoyo académico y personal que me brindó.

A Audrey Ferlatte, Rosalie Nardelli y Antonella Fratino por su apoyo técnico y administrativo.

A mis amigos Néstor Jiménez, Mabel Guzmán, Raúl Loera, Gonzalo Chavira, Gamaliel Baltazar, Tao Jiang, Areli Aceves, Carlos Tovar, Cynthia Torrecilla, Mariana Vasconcelos, Audrey Ferlatte, Viola Tokarova, Ondrej Kaspar, Laura Cervera, Linda Balabanian, Haruka Yoshie, Cuitlahuac Chavez, Ángel Hidalgo, Sergio Calderón, Rodrigo Juárez y Tomas Ortiz por su apoyo incondicional en todo momento.

A mis compañeros del Laboratorio 4 del IPICyT y a mis compañeros y amigos del departamento de bioingeniería de la Universidad de McGill.

Al Consejo Nacional de Ciencia y Tecnología por la beca otorgada No. 250279, becas mixtas No. 290936, al Instituto Potosino de Investigación Científica y Tecnológica, A. C. y a la Universidad de McGill.

Al Dr. Miguel Ávalos por el apoyo en el Laboratorio Nacional de Investigaciones en Nanociencias y Nanotecnología (LINAN) del IPICYT y a la maestra Lucia Aldana por su ayuda en la revisión del inglés.

Por último agradezco a mi familia por todo su apoyo y a todas las personas que conocí fuera de la institución por su amistad y palabras de aliento en momentos difíciles. A todos muchas gracias.

Contenido

Anexos

Resumen

Nanomateriales de carbón: biocompatibilidad y reforzamiento de materiales para tintas de bioimpresión 3D

Los nanotubos de carbono (CNTs, por sus siglas en inglés) y el grafeno (G) son formas alotrópicas del elemento carbono. Estos materiales de carbono exhiben propiedades físicas, mecánicas, térmicas y ópticas únicas, las cuales los hacen atractivos para diversas aplicaciones industriales y biomédicas. Debido a que los CNTs tienen forma similar a las fibras de asbesto, estos pueden presentar un riesgo potencial para la salud humana y por ello es crucial una caracterización toxicológica completa del material. El objetivo de este trabajo fue evaluar la biocompatibilidad/toxicidad de CNTs y G sobre células de mamíferos empleando diferentes metodologías de exposición, concentraciones, dispersante y tiempo de exposición. Demostramos que G es biocompatible con células mononucleares de sangre periférica. También, encontramos que la síntesis de CN_x produce diferentes morfologías de nanomateriales que generan diversas respuestas celulares en fibroblastos de ratón y células hematopoyéticas humanas. Sin embargo, los CN_x pertenecientes a la región de alta producción son biocompatibles con células de mamíferos y estas células pueden embeberlos. Por otro lado y de manera conjunta, se desarrolló un biomaterial (hidrogel) mejorado para cultivos en 3D. Este material está compuesto por dos polímeros biocompatibles, alginato y gelatina, los cuales son ampliamente usados en biomedicina como soporte celular. Estos hidrogeles fueron modificados mediante la incorporación de CNTs en su matriz, mejorando las propiedades del material. Los nanomateriales así como el composito formado por nanomateriales-hidrogel representan una alternativa para el desarrollo modelos 3D *in vitro*, que pudieran ser empleados en biomedicina.

PALABRAS CLAVE: Nanomateriales, nanotubos de carbono nitrógeno dopados, bio-impresión, hidrogeles, células de mamíferos, biocompatibilidad.

Abstract

Carbon nanomaterials: biocompatibility and reinforcement material for 3D bioprinting ink

Carbon nanotubes (CNTs) and graphene (G) are allotropic forms of carbon element. These carbon materials exhibit physics, mechanics, thermal and optical properties making them attractive for several industrial and biomedical applications. Since CNTs have similar shape to asbestos fibers, they could represent a potential risk for human health, and therefore, it is crucial a full characterization of CNTs. The aim of this work was to evaluate the biocompatibility/toxicity of CNTs and G on mammalian cells using different exposure methodologies, concentration, dispersant and time of exposure. We demonstrated that G are biocompatible with peripheral blood mononuclear cells. Also, we found that synthesis of CNTs produces different nanomaterials morphologies, which generate differences in the cellular response on fibroblasts and human hematopoietic stem cells. However, CN_x belonging to high region are biocompatible with mammalian cells and they can embed CN_x. Furthermore, an improved biomaterial (hydrogel) for 3D culture was made. This material is composed by two biocompatible polymers, alginate and gelatin, which are widely used in biomedicine for cellular support (scaffolds). These hydrogels were modified by the incorporation of CNTs to their matrix, improving the material's properties. The nanomaterials as well as the composite formed by nanomaterials-hydrogel represent an alternative for constructing 3D *in vitro* models, which could use them in the biomedical field.

KEY WORDS: Nanomaterials, nitrogen-doped carbon nanotubes, bioprinting, hydrogels, mammalian cells, biocompatibility.

1. General introduction

Carbon is presented in nature as several allotropic forms such as diamond, graphite, fullerene and amorphous carbon, for example (Figure 1a-d) [1, 2]. Other carbon allotropes are carbon nanotubes (CNTs, Figure 1e) and graphene (G, Figure 1f), which have an identical composition with a meshwork of sp^2-hybridized carbon atoms. However, these carbon materials have different structures [2].

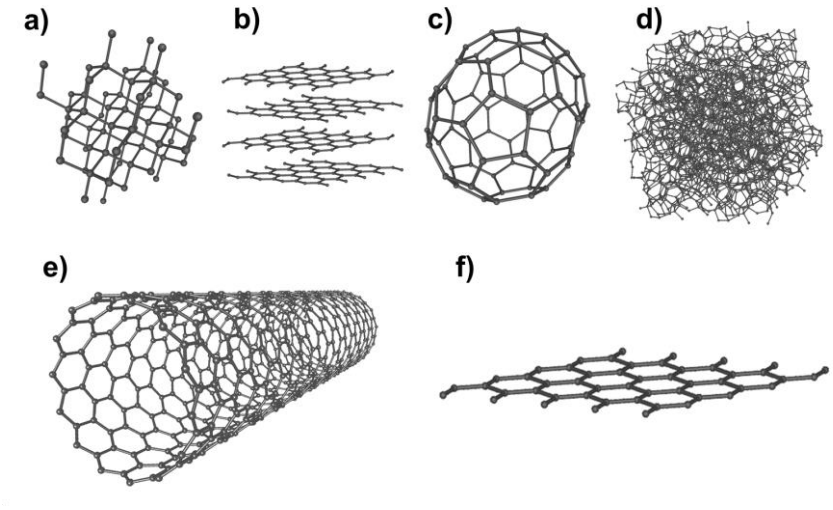

Figure 1. Carbon allotropes. a) diamond; b) graphite; c) fullerene (C70); d) amorphous carbon; e) carbon nanotube; f) graphene [3].

Since the carbon nanotubes (CNTs) were discovered by accident in 1991 [1], scientists were delighted with their unique physic, mechanic, thermal and optical properties of this new form of carbon [2]. In 2004, another carbon nanomaterial, graphene (G), started to gain more attention of the researches due to its properties [2, 4].

Both CNTs and G are materials ranging from nanometers (nm) to millimeters (mm) dimensions. CNTs are hollow cylinders of graphene sheets with a diameter range of 0.2 to hundreds of nm and lengths from 2 nm up to 10 mm [5, 6].

Meanwhile G is a 2D honey-comb lattice material with a carbon-carbon bond length of 0.142 nm [7, 8], which is presented as flakes with variable diameters and thickness in the order of nm and lengths from nm to mm [9].

In the industry, CNTs and graphene have been used for different applications. Furthermore, in biomedicine, both materials have been proposed for several uses such as cellular scaffold, drug delivery devices, imaging contrast agents, and for reinforcement of materials such as hydrogels, by using this hydrogel/carbon material as ink to create a 3D models employing 3D technology [4, 10-14]. However, considering the importance of using a new material in biomedicine, it is crucial to determine the biocompatibility or toxicity of the material. The present thesis focuses on the effects produced by CNT and G on different biological models as well as the development of hydrogels containing CNTs for 3D bioprinting ink.

This thesis is organized by chapters and is presented as follows: **chapter I** is focused on graphene oxide (GO) studies, the potential biological application of this carbon material has made that several research groups pay attention on the cellular response to GO, since a lot of studies lacking of a complete characterization of toxic degree and their only take in consideration two parameter to determine the biocompatibility/toxicity of the material using bacterial as a biological model. For that reason, we made a careful characterization of GO, analyzing their sizes and structural properties, using different methods of exposure with GO dispersed in two biocompatible solvents. We tested the GO against bacterial as well as peripherial blood mononuclear cells. According to our results, GO had 2D sizes of ~100 nm and >2 μm. we found that bacterial growth is

inhibited by the size of the GO, suggesting a toxic effect exposure method dependent. However, the GO was compatible with blood cells after 24 h of exposure. Our experiments provide vital information for future applications of GO in suspension. If its antibacterial properties are to be potentiated, care should be taken to select 2D sizes in the micrometer range, and exposure should not be carried out in the presence of grow media.

Chapter II is related with the toxicity of nitrogen-doped multiwalled carbon nanotubes (CN_x). We evaluated the toxicity of CN_x on mammalian cells applying three parameters: 1) different concentrations of CN_x, 2) exposure time and 3) the exposure route. Finding that CN_x are more toxic when they are incubated simultaneously with cells, compare with CN_x added to cultures 24 h after cell dissociation. Besides, we found cytotoxicity effect concentration and time dependent. Furthermore, during the chemical synthesis of CN_x, we observed that a high heterogenic material was produced with substantial differences on length and diameter size, which have distinctive cytotoxic effects on the proliferation of NIH-3T3 cells. However, concentrations of 7 µg/ml of these nanomaterials seemed to be well tolerated by the cells, and they could be used in biomedical applications.

Encouraged to find a biocompatible CN_x, in **chapter III** are presented the previous results of the effect of these nanomaterials with human and murine cells. By improving the recovery and purification process of CN_x, it was possible to select CN_x with specific properties. CN_x were classified based on their synthesis zone and we used different concentration and exposure time to evaluate their biocompatibility and toxicity. According to our results the CN_x that had belonged to high region of production were biocompatible with both kinds of cells; meanwhile,

CN_x from middle region were toxic for cells, suggesting a heterogeneous production of CN_x with different properties. Therefore, we demonstrated that heterogeneous morphologies of CN_x synthesized in the same batch generate differences in the cellular response. Furthermore, we have shown that CN_x belonging to high region (CN_x-HR) are biocompatible with mammalian cells and they can be uptaken.

Due to the CN_x have similar surface roughness as collagen fibers of the extracellular matrix [15]; the next step was the incorporation of these nanomaterials to hydrogels. The **chapter IV** is the compilation of the results obtained of hydrogel preparation and their use as a 3D bioprinted culture model. First, we evaluated the biocompatibility and suitability of the hydrogel for cell migration, and second, we added nanomaterials to reinforce the hydrogel (**chapter V**). We used fibroblast-associated to cancer cells and breast cancer cells as biological models, which were embedded in an alginate/gelatin hydrogel and extruded using a 3D printed. According to our results, this 3D hydrogel model allowed cells to grow and proliferate as well as to achieve a higher viability than conventional 2D cell culture. Also, the 3D hydrogel created an environment that mimics the natural environment of tumor cells since it allowed the formation of multicellular tumor spheroids which increase in size over time. This study provides insights into reconstructing biomimetic *in vitro* tissue co-culture models to study cell-cell and cell-matrix interactions, and tumorigenesis mechanisms.

Finally, in **chapter V**, we incorporated nanomaterials to the alginate/gelatin hydrogel. Since alginate is lacking of tunable physical properties, we modified these characteristics by addition of CN_x and chemical modification of alginate with

nanomaterials. Due to the low quantity of nanomaterials used, the mechanical properties of alginate hydrogel was not modified; however, the cellular response to hydrogel-CN_x was better (more biocompatible) in contrast to the hydrogel alone, suggesting that CN_x play and important role in the proliferation of cells in 3D cultures. Similar results were obtained when we used aginate/gelatin hydrogels (with or without nanomaterials) showed biocompatibility with cells, as well as alginate-wrapped CN_x hydrogels. As a proof of concept, we used alginate/gelatin+CN_x hydrogel to create 3D structures using a bioprinted, where the structures demonstrated a high stability after printed and well dispersion of cells in the gel. The alginate/gelatin+CN_x composite hydrogel can enable the ability to tune properties such as the mechanical, electrical, or optical characteristics of the otherwise inert alginate gel.

In conclusion, we present a full compilation of biocompatibility/toxicity of two kinds of carbon nanomaterials as well as their potential used for several biomedical applications such as material reinforcement, cellular scaffold and drug delivery.

2. Chapter I

Effect of graphene oxide on bacteria and peripheral blood mononuclear cells

Driven by the potential biological applications of graphene, many groups have studied the response of cells exposed to graphene oxide (GO). In particular, investigations of bacteria indicate that there are 2 crucial parameters, which so far have only been investigated separately: GO size and exposure methodology. Our study took into account both parameters. We carefully characterized the samples to catalog sizes and structural properties, and tested different exposure methodologies: exposure in saline solution and in the presence of growth media. Furthermore, we performed experiments with peripheral blood mononuclear cells exposed to our GO materials. Atomic force microscopy, scanning electron microscopy, Raman spectroscopy, X-ray photoelectron spectroscopy and transmission electron microscopy were used to characterize the morphology and composition of different samples of GO: GO-H_2O, GO–phosphate-buffered saline (GO-PBS) and GO manually ground and dispersed in water (GO-MG).Our samples had 2D sizes of ~100 nm (GO-H_2O and GO-PBS) and >2 μm (GO-MG). We tested antibacterial activity and cytotoxicity toward peripheral blood mononuclear cells of 3 different GO samples. A size-dependent growth inhibition of *Escherichia coli* (DH5 α) in suspension was found, which proved that this effect depends strongly on the protocol followed for exposure. Hemocompatibility was confirmed by exposing peripheral blood mononuclear cells to materials for 24 hours; viability and apoptosis tests were also carried out. Our experiments provide vital information for future applications of GO in suspension. If its antibacterial properties are to be potentiated, care should be taken to select 2D sizes in the micrometer range, and exposure should not be carried out in the presence of grow media.

Effect of graphene oxide on bacteria and peripheral blood mononuclear cells

Jessica Campos-Delgado, Kelly L.S. Castro, Jose G. Munguia-Lopez, Ana K. González, Martin E. Mendoza, Benjamin Fragneaud, Raphael Verdan, Joyce R. Araujo, Francisco J. González, Hugo Navarro-Contreras, Ivan N. Pérez-Maldonado, Antonio de León-Rodríguez, Carlos A. Achete

Journal of Applied Biomaterials & Functional Materials

DOI: 10.5301/jabfm.5000325

1. Introduction

The attention that graphene has attracted since its isolation in 2004 is undeniable [1]. Over the years, an increasing number of scientific groups have been seduced by its amazing electronic, mechanical, optical and thermal properties, and evidently, by its innumerable potential applications [2]. However, due to the hydrophobic nature of pristine graphene, in biomedicine, graphene oxide (GO) is considered a better alternative thanks to its hydrophilicity, amphiphilicity and availability of functional groups attached to its surface or edges [3]. Along with the debut of graphene and GO in biological applications has come the necessity of studying their biocompatibility [4-13]. Of particular interest have been the reported antibacterial properties of GO [5, 7-11, 14].

Akhavan and Ghaderi [7] argued that the adverse effect of graphene on bacteria is to be attributed to membrane damage by the numerous sharp edges of

GO, while others have focused on oxidative stress as the toxic mechanism [8]. A recent paper by Mangadlao and coauthors [15] reported on the fabrication of GO films through the Langmuir-Blodgett technique, where graphene sheets lie flat on a polyethylene terephthalate (PET) substrate. Thus the sharp edges of GO were not available to pierce the membranes, and yet antibacterial activity was still observed, suggesting that the antibacterial activity of GO does not rely on membrane damage by its sharp edges.

Liu and coauthors [14] conducted experiments that showed that the antibacterial effect of GO depends on the sheet size, suggesting that large graphene sheets wrap bacteria and block interactions, isolating them from the environment, while small sheets interact with bacterial surfaces in a non-harmful way. These results confirmed the encapsulation by graphene reported previously by another group in 2011 [16]. Many groups have studied the response of bacteria exposed to GO, and although many researchers have agreed on its antibacterial effect [5, 7, 8, 11, 13], a couple of research groups have reported a contrary effect [9, 10]. Ruiz et al [9] confirmed a GO enhancement effect on *Escherichia coli* proliferation, and Das et al [10] confirmed the kinetic growth of *Pseudomonas aeruginosa* and *E. coli* in the presence of GO. These early controversial reports have led to more investigations into the subject. Recently, Hui and coworkers [17] conducted experiments where they demonstrated that the discrepancies regarding the antibacterial effects of GO lie in the way that GO is exposed to the bacteria.

When bacteria is exposed to GO in pure saline solution, the antibacterial effect is observed; however, this antibacterial activity decreases progressively when increasing amounts of Luria-Bertani (LB) broth are added to the saline

solution. They attribute this decrease of bactericidal activity to the absorption of LB molecules on the surface of the graphene; hence, the more the graphene surface is free from adsorbates, the greater the antibacterial effect it will have. Although this piece of research is very valuable and clarifies the controversial results above discussed, it lacks important information about the characterization of the GO used and does not take into account the size-dependent antibacterial effect reported by Liu and coauthors [14]. Moreover, an inspection of the GO materials shown on their figures demonstrates a size-heterogeneous sample.

As described above, different groups have attempted to study the antibacterial effect of graphene and have found 2 major influential parameters: size and exposure methodology. Our study brought together both approaches. We carefully characterized the samples to catalog the sizes and structural properties and tested different exposure methodologies: exposure in saline solution and exposure in the presence of growth media. Our results indicated that the antibacterial effect was not only size dependent but also depended on the exposure technique.

When it comes to cytotoxicity toward mammalian cells, the picture is not any more uniform [4, 12, 13, 18-25]. Some groups have reported on the biocompatibility of graphene [4, 13, 18, 21-23, 25], while others have discussed its toxicity in terms of concentration and degree of oxidation [12, 19, 20, 26]. The same dilemma applies to its hemocompatibility [12, 22, 27, 28]. In any case, many authors who have written reviews on this topic [23-25, 29, 30] have agreed on the need to standardize protocols for the evaluation of cytotoxicity, be-cause many studies are not comparable due to differences in synthesis and processing

methods of GO which yield a wide spectrum of physicochemical properties. Sheet size, surface functionalization, degree of oxidation, purity and defects are some of the parameters of GO that vary from one report to the other, rendering it very difficult to draw conclusions from the available literature.

We carried out atomic force microscopy (AFM), scanning electron microscopy (SEM), Raman spectroscopy and X-ray photoelectron spectroscopy (XPS) to study the morphology and structure of different GO materials. We also performed an exhaustive series of experiments to test the effects of our GO samples on bacteria and mammalian cells. We produced graphite oxide (GtO) from expanded graphite using the modified Hummers method, followed by a purification process. Using this GtO, we obtained 3 different materials: GO dispersed in water for 6 hours in an ultrasonic bath (GO-H_2O), GO dispersed in phosphate-buffered saline (PBS) for 6 hours in an ultrasonic bath (GO-PBS) and GO manually ground and dispersed in water (GO-MG). We confirmed that the antibacterial effect of GO is size dependent and proved that the protocol for exposure plays a crucial role. Our experiments with peripheral blood mononuclear cells (PBMCs) confirmed the hemocompatibility of our different GO materials for the exposure protocol used.

2. Materials and methods

2.1 Graphite Oxide (GtO) production

We obtained graphite oxide from expanded graphite (from Nacional de Grafite, Brasil) using the modified Hummers method [31], followed by a purification process. Concentrated H_2SO_4 (9.2 mL) was added to a mixture of expanded

graphite (Provided by Nacional de Grafite, Brasil, 0.4 g) and $NaNO_3$ (0.2 g) in an ice bath. $KMnO_4$ (1.2 g) was added slowly to keep the temperature of reaction lower than 20 °C. The mixture was warmed to 35 °C and stirred for 30 min. After, water (18.2 mL) was added slowly to the medium promoting a large exothermic reaction and increasing the temperature up to 98 °C. An external heating was used to maintain the reaction temperature at 98 °C for 15 min, then a water bath was used to cool the reaction for 10 min. Additional water (55.3 mL) and 30% v/v H_2O_2 (0.4 mL) were added to stop reaction, producing another exothermic process.

After the oxidation reaction the brown-colored slurry was washed with HCl solution (180 mL of water and 20 mL of 30% v/v HCl solution) for removal of metallic ions. Then, the solution was exhaustively washed with water and centrifuged to remove impurities until the pH of the supernatant become neutral. The residual water was removed through freeze drying process.

GO materials preparation

The different materials used in this study (GO-H_2O, GO-PBS, GO-MG) were derived from graphite oxide (GtO) which was obtained by the modified Hummers method followed by the purification process described above.

For the preparation of GO-H_2O, 6 mg of GtO were added to 3 ml of Milli-Q grade water leading to a concentration of 2 mg/ml, then this solution was dispersed using an ultrasonic bath for 6 hours. The resulting material consisted of a dark colored solution that showed to be very stable and as time passed no segregation of the material occurred.

To prepare GO-PBS, 6 mg of GtO were diluted in 6 ml of sterile PBS (phosphate-buffered saline) (concentration 1 mg/ml), followed by 6 hours of

dispersion by ultrasonic bath. The resulting solution was homogenous however after time passed the GO tended to segregate at the bottom of the vial. The color of the solution was similar to that of GO-H_2O (black brown).

GO-MG was prepared using a mortar, 6 mg of GtO were manually ground for 5 minutes, during this time 2 ml of Milli-Q H_2O were added to the mortar and the other 4 ml were used to wash away the material from the mortar and to recover it in a vial (final concentration 1 mg/ml), then the material was subjected to 8 min dispersion in an ultrasonic bath. The morphology of the sample was very different to that of GO-H_2O and GO-PBS, the color of the solution was dark gray and small dark particles were visible, segregation of the material occurred when left overnight.

2.2 Raman spectroscopy

Raman spectroscopy analyses were carried out on a Witec Alfa 300 spectrometer, with a 532 - nm laser line in backscattering configuration using a microscope with a •50 objective. The laser power was kept under 0.1 mW to avoid local heat damage to samples. All spectra were acquired with 10 accumulations of 10 seconds of integration time in the region between 100 cm^{-1} and 3,600 cm^{-1}.

2.3 Atomic force microscopy

To carry out AFM imaging of the different GO samples, we deposited a diluted solution of each GO on a Si/SiO_2 wafer by drop casting. The drop was carefully rolled over the wafer to uniformly disperse single layers and a few layers

of GO. Finally, the excess of solution was blown off with nitrogen (N_2). The samples were dried in ambient conditions for 24 hours. The AFM images were obtained in intermittent contact mode with a JPK Nanowizard 3 using a silicon nitride tip (spring constant of 40 N/m).

2.4 Transmission electron microscopy

Dispersed solutions of the different GO materials were used to deposit them on Cu holey carbon grids (300 mesh). A probe-corrected FEI Titan 80-300 microscope was used at 80 kV to minimize beam damage effects. Conventional bright field images and high-resolution transmission electron microscopy (HRTEM) images were taken. Electron energy loss spectroscopy (EELS) measurements were done in spectroscopy mode (STEM-PEELS) using a GIF 866 camera under the following experimental conditions: α = 58.5 mrad, GIF aperture = 2.5 mrad, dispersion = 0.02 eV/ch with ZLP_{FWHM} resolution of 0.8 eV.

2.5 Scanning electron microscopy

The GO solutions were diluted to a concentration of 5 µg/mL using deionized water. One drop of each solution was deposited on a 300-nm SiO_2/Si substrate kept at 50°C on a hot plate and allowed to dry. SEM images were obtained at 15 kV and 50 pA, with secondary electron detection using the Through Lens Detector (TLD-detector) in FEI Helios Nanolab 650.

2.6 X-ray photoelectron spectroscopy

XPS analyses were performed in an ultrahigh vacuum medium (pressure of

10^{-9} mbar) using an Mg, Kα (hv = 1,253.6 eV) X-ray source, with power given by emission of 20 mA, at a voltage of 15 kV. For the carbon element, the high-resolution spectra were obtained with analyzer pass energy of 20 eV in steps of 0.05 eV. The binding energies were referred to the carbon 1s level of a neat graphite sample, set as 284.8 eV.

2.7 Bacteria growth experiments

In the literature, many groups have tested the antibacterial activity of GO. Although the early reports were contradictory, a recent study attempted to elucidate the nature of these controversial effects [17]. The authors state that the observed antibacterial effect is directly related to the availability of graphene's basal planes, and they further affirm that when GO is exposed to bacteria, its effect is determined by the media in which the 3-hour exposure takes place. If the exposure is carried out in a saline solution, then GO will have an antibacterial effect; when this exposure is carried out in LB broth growth medium, no antibacterial effect was evidenced.

Having these results in mind and to avoid masking antibacterial effects by the medium components, we decided to test the effect our GO-H_2O material for the growth of the gram-negative bacteria *E. coli* (DH5 α), probing 3 different exposure times: 0, 1 and 3 hours in saline solution. Briefly, the experiment consisted of growing *E. coli* in LB broth base (Invitrogen) at 37°C overnight. Then the culture was changed with fresh medium and allowed to grow again to the exponential phase. *E. coli* at $7x10^7$ cells/mL was resuspended in saline solution (0.9% NaCl) and incubated to a final concentration of 200 µg/mL of GO-H_2O for 1 and 3 hours

at 37°C and under agitation. As control, we used samples exposed to Milli-Q grade water. After this step (referred to as exposure), cells along with the materials were harvested by centrifugation at 10,000 RPM for 5 min to collect the cells along with the materials and resuspended in 60 mL of fresh medium in flasks to get a final cell concentration of $1.2x10^6$ cells/mL; then, flasks were incubated at 37°C under agitation (the recovery step) for 500 minutes. For the 0-hour-exposure experiments, the cells were put in contact with the material and immediately allowed to undergo the recovery step. After 500 minutes, the optical density at 600 nm (OD_{600}) of the cell cultures was measured, readings were recorded 3 times and all experiments were performed in triplicate.

To assess the growth of *E.coli* in contact with GO-PBS and GO-MG, the same protocol was followed. $4x10^7$ cells were put in contact with 200 μl of GO-PBS (GO-MG) at different final concentrations (200 μg/mL, 20 μg/mL and 2 μg/mL), for the control 200 μl of stile PBS (Milli-Q H_2O) were added and 800 μl of sterile saline solution (0.9 % NaCl) were added to each tube to adjust to 1 mL.

After this preparation the tubes followed an “exposure” step of 1 hour at 37°C under agitation, then, were centrifuged at 10,000 RPM for 5 min, removing the saline solution and resuspending the pellets in flasks with 60 ml of fresh LB broth, leading to a concentration of $6.4x10^5$ cells/mL. The flasks were placed at 37°C under agitation for 420 minutes, during this time lapse systematic OD_{600} measurements were recorded (at 0, 120, 180, 210, 240, 270, 300, 330, 360, 390, 420 minutes). For each measurement three readings were recorded and each experiment was performed in triplicate.

We calculated the specific growth rate for the all kinetics of *E. coli* as another parameter to determine the antimicrobial activity. We treated the data for the control and the three different concentrations used (2 µg/ml, 20 µg/ml and 200 µg/ml), for the three different kinds of GO tested (GO-H_2O, GO-PBS, GO-MG).

2.8 Peripheral blood mononuclear cells experiments.

We tested our materials on mammalian cells by exposing PBMCs to different concentrations of GO-H_2O, GO-PBS and GO-MG, and performed cell viability and apoptosis tests after 24 hours. We separated peripheral blood mononuclear cells (PBMCs) from freshly extracted blood from healthy individuals (8-12 ml). The cells were isolated using Ficoll density gradient (1.077 g/cm^3) by centrifugation at 2,500 rpm for 20 min. PBMCs were collected, washed with PBS and centrifuged at 1,500 rpm for 15 min. The supernatant was decanted, and the cells were resuspended in RPMI-1640 medium (Sigma-Aldrich) with L-glutamine, 10% fetal bovine serum (FBS) (Gibco) and 1 % penicillin-streptomycin (Gibco) and counted using a hemocytometer.

Then the cells were exposed to our materials at concentrations of 2, 20 and 200 µg/mL on multiwell culture plates and incubated for 24 hours at 37°C in a 5% CO_2 humidified incubator, including a positive and a negative control. The negative control consisted of only medium and cells, and positive control was 0.3% H_2O_2. We performed trypan blue cell viability tests counting live/dead cells using a hemocytometer. Experiments were performed in triplicate, that is, PBMCs from three different individuals were used.

Apoptosis was measured using Annexin-V-FITC Apoptosis Detection Kit (eBioscience). PBMCs were exposed to GO at different concentration for 24 h, following the procedure describe above. Cells were collected by centrifugation 1,500 rpm for 5 min. The cell pellet was resuspended in 100 µL of Annexin V Binding Buffer and stained with Annexin V-FITC Apoptosis Detection Kit, according to the manufacturer instructions. The samples were incubated at 4°C for 20-30 min. Later, the cells were analyzed using a flow cytometer BD®FacsCalibur.

3. Results

3.1 Sample characterization

We thoroughly studied the physical and chemical properties of our GO materials. AFM, SEM and TEM were used to figure out the morphological characteristics of the different samples, and EELS and XPS to understand their chemistry. Our studies revealed that the GO-H_2O sample contained small fragments of GO with average 2D sizes of 100 nm and 1 or 2 layers on thickness (Figure 1a, d and g). The sample GO-PBS was very similar in morphology to GO-H_2O, as can be confirmed in Figure 1b and e. This was not a surprise since both samples were subjected to the same preparation treatment (6 hours in ultrasonic bath); however, the difference between the samples lay in the medium of dispersion (i.e., for GO-PBS, PBS was used). This difference resulted in many PBS residuals that accompanied the GO sheets. Figure 1h shows a TEM image of GO-PBS where an impurity can be seen. Furthermore, Figure 2a and b shows an SEM image where the impurities are clearly localized on top of the GO, and our XPS

analysis revealed signals from Na, Cl, K and P that evidently came from PBS residues.

Sample GO-MG showed very different characteristics. Figure 1c, f and i reveal that GO-MG contained larger-area GO sheets, averaging several microns, showing similar morphological characteristics to those of exfoliated graphene. Nevertheless, structural damage in the honeycomb structure was detected.

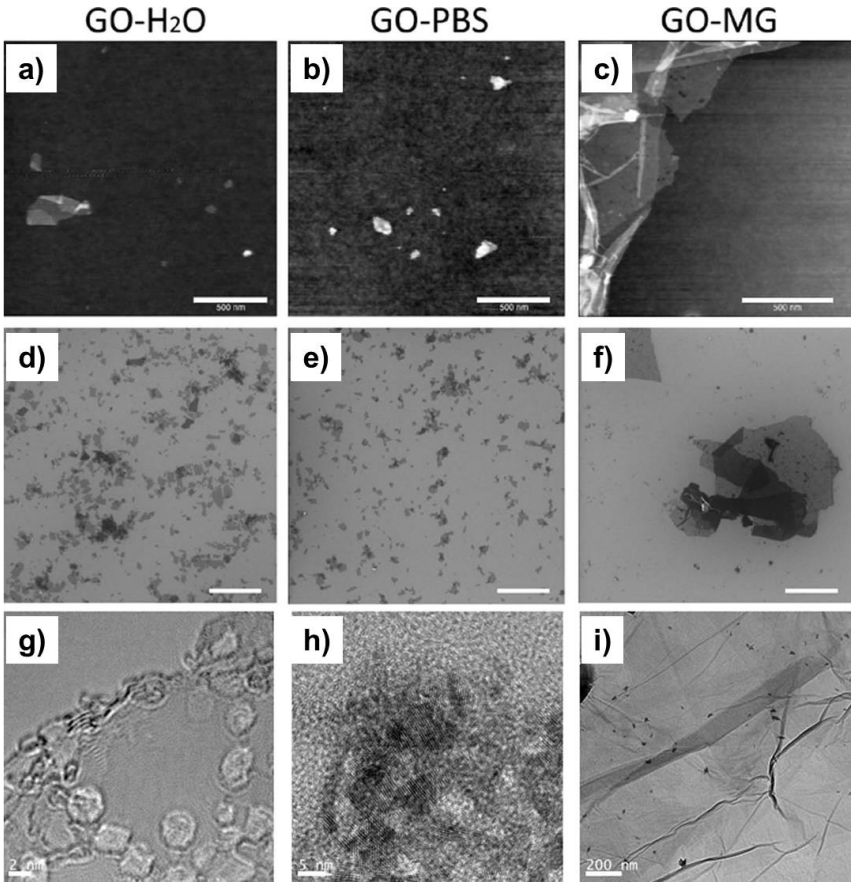

Figure 1. Representative atomic force microscopy (AFM) (a-c), scanning electron microscopy (SEM) (d-f) and transmission electron microscopy (TEM) (g-i) micrographs of graphene oxide (GO) samples: (a, d, g) GO-H_2O; (b, e, h) GO–phosphate-buffered saline (GO-PBS); (c, f, i) GO manually ground and dispersed in water (GO-MG). Scale bars represent 500 nm in (a-c); 1 μm in (d-f); and 2 nm, 5

nm and 200 nm in (g), (h) and (i), respectively.

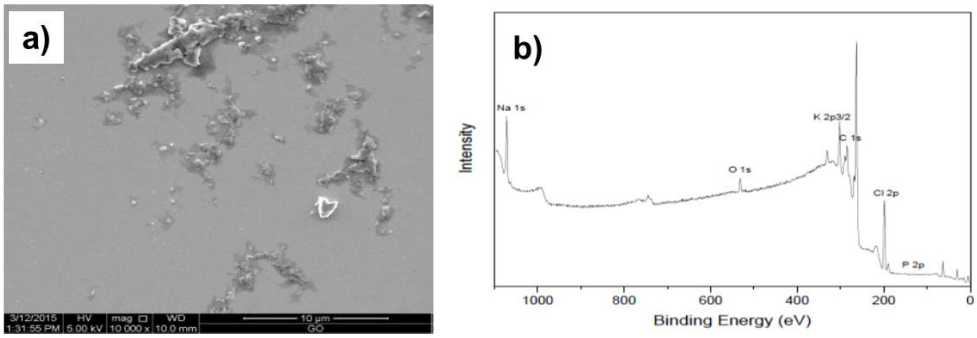

Figure 2. Scanning electron micrograph of the sample GO-PBS (a) and XPS spectrum (b).

Our XPS analysis of the C binding energies confirmed the presence of sp^2 (C=C) at 283.9 eV and carbon atoms out of regular sp^2 configurations (C-C/C-H) at 284.8 eV as expected for GO [32]. Beyond that, other oxygenated carbon functional groups were observed, such as phenol or epoxide (C-OH/C-OC) between 285.8-286.3 eV, carbonyl groups (C=O) at 287.1 eV, carboxyl groups (COOH) at 288.7 eV and the π-π* shakeup satellite at approximately 291.0 eV typical of aromatic delocalized electrons [33]. Figure 3a and b shows XPS spectra of GO-H_2O and GO-MG, respectively. It is clear that although the nature of the bonds present in both samples is the same, their distribution is different.

This was expected, as both samples were derived from GtO and dispersed in water; however, the preparation method led to more sp^2 hybridization in the GO-H_2O sample (18% against 9% in GO-MG; as confirmed by EELS results in Figure 4). On the other hand, the oxidized functional groups also showed differences in composition: the most intense component for GO-H_2O was the carbonyl groups (C=O) (25%), which were preferentially located on the edges of graphene sheets,

while for GO-MG, the most intense component was the third component, C-OH/C-O-C (25%), typically located on the basal plane of graphene [34].

As mentioned above, the XPS analysis of the GO-PBS sample revealed the presence of elements other than C and O, which were due to the diluent.

Representative Raman spectroscopy results are included in Figure 3c. Bulk measurements of the GO materials revealed the strong presence of the D and G bands, located at ~1,350 cm^{-1} and ~1,590 cm^{-1}, respectively. All spectra shared intense D bands and sharp G bands. We attribute such an intense defect-related band (D band) to the presence of sp^3 hybridization and to the high amount of oxygen bonds which were perforce present on GO.

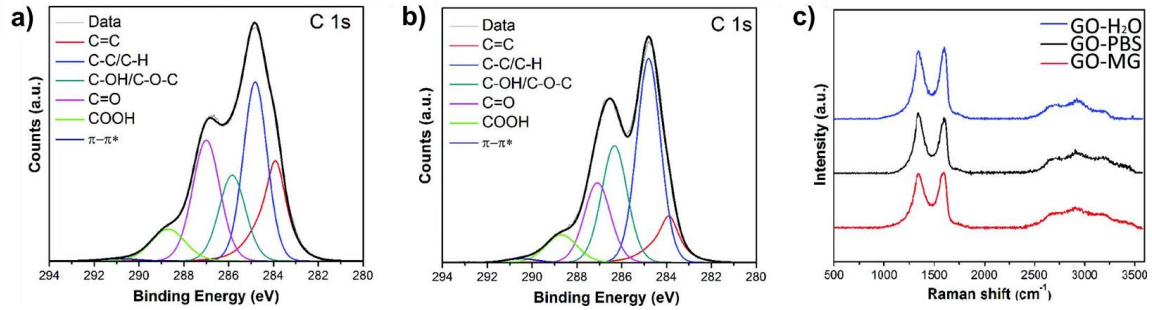

Figure 3. (a, b) X-ray photoelectron spectroscopy (XPS) spectra of graphene oxide (GO)-H_2O and GO manually ground and dispersed in water (GO-MG), respectively; (c) Raman spectra of the GO materials.

However, the I_D/I_G ratio of the GO-PBS sample was the highest (1.1 compared with 0.97 for both GO-H_2O and GO-MG) probably due to the presence PBS residues, as confirmed by TEM and SEM. From a simple inspection, it is quite obvious that the spectra of the 3 different GO samples are rather similar. For samples GO-H_2O and GO-PBS, this is expected, since the morphology of the

samples is comparable (see Figure 1); however, although sample GO-MG possesses very different characteristics, its Raman spectrum also looks similar.

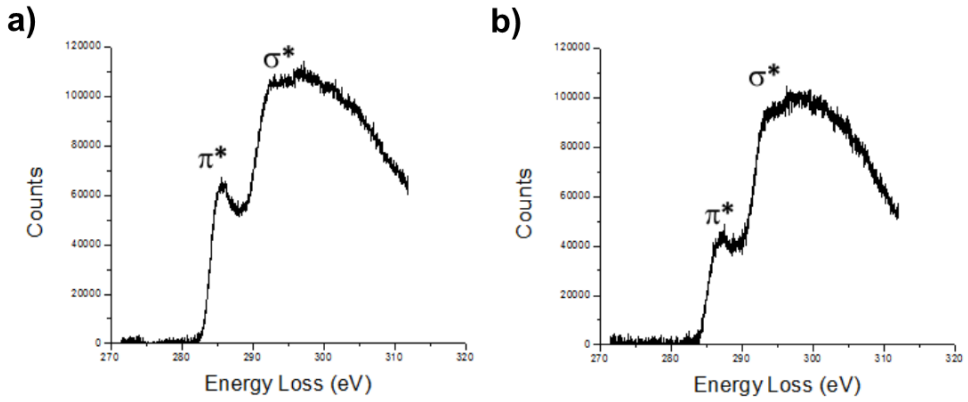

Figure 4. Carbon K edge EELS spectra after background subtraction of (a) GO-H_2O and (b) GO-MG. Peaks corresponding to the 1s → π* (284 eV) and 1s → σ* (291 eV) transitions are observed. Comparison of both spectra confirms a higher amount of sp^2 hybridization for GO-H_2O.

This suggests a high level of defects due to the less regular sp^2 carbon structure, as detected by XPS and EELS. It is possible that the high D band is due to the symmetry breakpoints that arise from in-plane defects (see Figure 1c), high proportion of sp^3 hybridization, OH-terminated edges and C-O bonds present in the sample. From our characterization, we can conclude that GO-H_2O and GO-PBS share morphology features (~100 nm, 1-2 layers, amount of defects), while GO-MG presents larger areas but the same average amount of defects. Regarding surface chemistry, it can be concluded that all samples present a significant amount of sp^3 hybridization and oxygen species.

3.2 Biocompatibility tests

Figure 5 shows the growth of *E. coli* in the presence of GO. Our results showed that the presence of GO-H_2O at such a high concentration did not have a negative impact on bacterial cell growth (Figure 5a). For the 3 exposure times, the OD values of the cultures with GO-H_2O were quite similar to those of controls, suggesting that the amount of living cells did not decrease in contact with GO-H_2O. It is worth mentioning the slight decrease in OD600 values for the 3-hour exposure set; both samples (control and GO-H_2O) showed lower values compared with those of the 0-hour and 1-hour exposure sets. We attribute this to a uniform decrease in the amount of living cells after 3 hours of agitation and the decrease of specific growth rate (μ) due to the lack of nutrients in the saline media. To avoid this effect, we chose to perform exposures of 1 hour for our growth kinetic experiments.

To assess the effect of our different GO materials (GO-H_2O, GO-PBS and GO-MG), we performed a 7-hour kinetic study of the growth of *E. coli*, with an exposure to the materials of 1 hour. We tested 3 different concentrations: 2, 20 and 200 μg/mL for each material. Conditions were similar to those in the above-described experiment (see the section “X-ray photoelectron spectroscopy”) except that during the recovery step, systematic OD_{600} readings were recorded from the cultures.

Figure 5b, c and d shows the results of our kinetic study of *E. coli* exposed to GO-H_2O, GO-PBS and GO-MG, respectively. From our above-described results, we did not expect to find an antibacterial effect of the GO-H_2O material, and such a conclusion was confirmed by Figure 5b which shows that the 3 concentrations of

GO-H_2O tested had no adverse effect on the growth of *E. coli*. Our characterization showed that the morphology of the GO-PBS sample was quite similar to that of GO-H_2O. Thus no antibacterial effect was expected from this sample either. Figure 3C confirms that the presence of GO-PBS at concentrations of 2, 20 and 200 µg/mL did not interfere with the growth of *E. coli*.

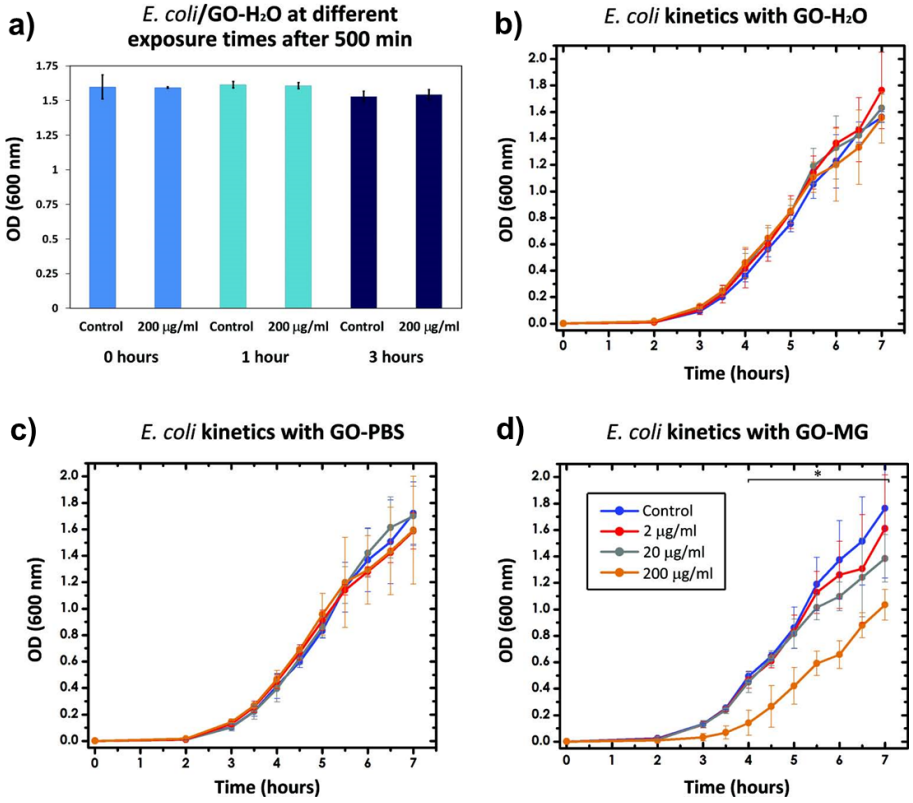

Figure 5. (a) *E. coli* exposed to graphene oxide (GO)-H_2O at different times (0, 1 and 3 hours) and incubated for 500 minutes in fresh Luria-Bertani medium for a recovery process; (b-d) growth kinetics of *E. coli* exposed for 1 hour to different concentrations of GO-H_2O, GO–phosphate-buffered saline (GO-PBS), GO manually ground and dispersed in water (GO-MG), respectively. Inset in (d) contains the color codes assigned to the different concentrations used in the study, which apply to graphs (b-d). Experiments were performed in triplicate, error bars

stand for the standard deviation of the recorded values. OD = optical density; *$p<0.05$, n = 3.

Our characterization evidenced the marked differences in morphology that the GO-MG sample presented when compared with GO-H_2O (see Figure 1). Such differences proved to have a strong impact on the growth of *E. coli* at the highest tested concentration (200 µg/mL). The results of our kinetic study (Figure 5d) revealed that low doses of GO-MG (2 and 20 µg/mL) do not show any effect on the growth of *E. coli*; however, a higher concentration (200 µg/mL) proved to have an adverse effect on the growth, where µ decreased to a value of 0.021 h^{-1} (±0.002) compared with 0.0265 h^{-1} (±0.0009) for the control (Figure 6a).

We performed 1- and 2-way ANOVA with Dunnett's post test to compare the different concentrations used against the control. Values of $p < 0.05$ were considered as significant.

We conclude that the sample GO-MG at high concentration shows an antibacterial effect which is the product of the high amount of large-area sheets that wrap around the bacteria, isolating them and disabling their proliferation, in good agreement with the reports of Liu et al [14] and Hui et al [17].

Our study revealed as well that the GO-MG antibacterial effect evidenced here was the product of the interactions with GO during the exposure step, and such an effect was not masked by the presence of LB growth medium during the recovery phase. Furthermore, the absence of this exposure step in saline solution (0-hour exposure) led to a complete suppression of the antibacterial effect of GO-MG (Figure 7), suggesting an adsorption of LB on the surface of the graphene and

an inability of the sheets to wrap and isolate *E. coli* – in good agreement with the conclusions drawn by the group of Hui et al [17].

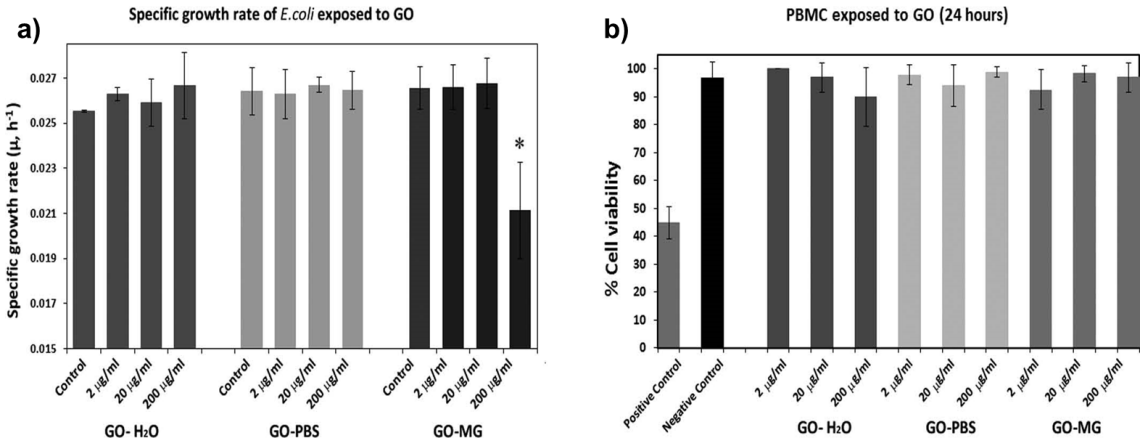

Figure 6. (a) Specific growth rate of *E. coli* in contact with graphene oxide (GO) materials, calculated from the 7-hour growth kinetic study. *p<0.05, n =3; (b) viability of peripheral blood mononuclear cells exposed to GO materials after 24 hours.

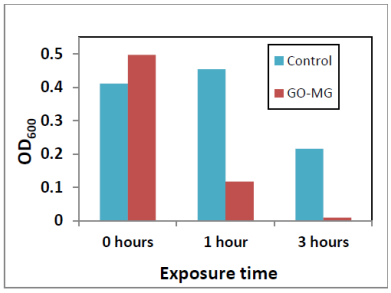

Figure 7. Effect of GO-MG on *E. coli* at different exposure times, OD_{600} readings were recorded after 220 minutes for exposures of 0, 1 and 3 hours.

3.3 Cytotoxicity to PBMCs

Results for the test of cell viability are shown on Figure 6b, indicating that the presence of GO materials did not have a negative effect on the viability of cells at 24 hours of exposure. The lowest viability identified was for the GO-H_2O sample at the highest concentration tested (200 µg/mL) with a value of 89.95% ± 10.55%.

For the rest of the samples, viability was above 90%, proving good hemocompatibility, which is in agreement with previous reports on the subject [22, 27].

Apoptosis tests were conducted on PBMCs exposed to our materials for 24 hours at concentrations of 2 and 20 µg/ mL. We evaluated whether our materials induced apoptosis of PBMCs, by flow cytometry using annexin V/propidium iodide markers. Representative dot plots of the apoptosis assay are shown in Figure 8a-e. Interestingly, for all of the materials for both concentrations tested, the percentage of apoptotic cells was very close to that of the negative control (Figure 8f). In addition, we did not find any increase in necrotic cells when our materials were present, as revealed by the propidium iodide marker, and no early apoptosis was detected, which was revealed when only the annexin marker was used.

It is important to point out that the 24-hour exposure of GO samples to PBMCs described above was done in the presence of RPMI-1640 medium with L-glutamine, 10% fetal bovine serum (FBS) and 1% penicillin-streptomycin. The availability of nutrient molecules from the growth medium opens the possibility of absorption of proteins into the GO basal plane masking thus its toxic effect. To investigate this possibility, new sets of experiments are being designed and performed, in which exposure of GO samples to PBMCs is carried out in the absence of nutrient molecules, as in the case of bacteria.

4. Discussion

We performed a complete characterization of 3 different GO samples and tested their toxicity to bacteria and PBMCs. GO-H2O and GO-PBS were obtained by the same preparation method from GtO; a 6-hour sonication treatment produced

GO dispersed in water (GO-H2O) and in PBS (GO-PBS). These samples had 2D dimensions of ~100 nm, consisted of 1-2 staked layers, had sp^3 hybridization and were bonded to oxygen species. GO-MG was derived from GtO by manual grinding and dispersed in water. This preparation led to a material of 1-2 layers with 2D dimensions of several microns possessing many in-plane defects, along with sp^3 hybridization and reactive oxygen species. Our experiments in suspension proved that GO-H2O and GO-PBS did not show an antibacterial effect to *E. coli*, while the presence of 200 μg/mL of GO-MG decreased its specific growth rate. It is thus evident that not every type of GO will present antibacterial activity; this effect is size-dependent, and small sheets do not interfere with bacteria growth, while large sheets (several microns) tend to inhibit it.

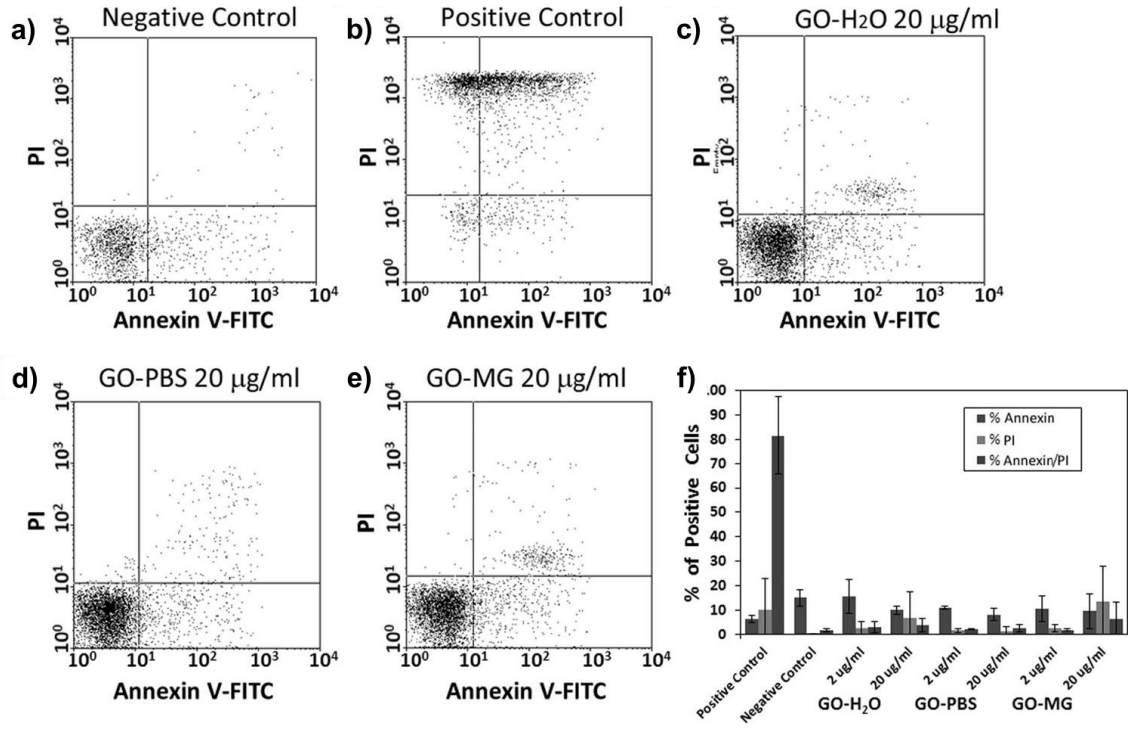

Figure 8. Results of the annexin V-FITC and propidium iodide (PI) assay. Representative scatter diagrams of peripheral blood mononuclear cells (PBMCs):

(a) negative control, (b) positive control, (c-e) exposed to 20 µg/mL of graphene oxide (GO)-H_2O, GO–phosphate-buffered saline (GO-PBS) and GO manually ground and dispersed in water (GO-MG), respectively; (f) summary of the percentage of positive cells for annexin, PI and annexin/PI.

We proved as well that the protocol followed for exposure of GO-MG to bacteria was vital for the outcome. While direct exposure of bacteria to all concentrations of GO-MG in LB media did not show an adverse effect; if the first contact was carried out in saline solution for 1-3 hours, then the presence of GO-MG at 200 µg/mL would decrease the specific growth rate of *E. coli*. This observation is in accordance with the results of Hui et al [17] and explains previous contradictory results on the toxicity of GO to bacteria due to protocol discrepancies.

Experiments with PBMCs exposed to our GO materials indicated that no adverse effect was observed after 24 hours, in good agreement with previous studies; however, further studies are underway to account for the effect in the absence of nutrient molecules that could be absorbed on the basal planes of GO [22, 27]. For the applications of GO in biology, and in particular, if its antibacterial properties are to be potentiated, it is thus very important to perform a characterization of the material, giving special attention to its dimensions and homogeneity, as well as to the protocol for exposure.

Acknowledgement

We thank B. Archanjo, M. Pojucan, M. Gutiérrez-Hernández and E. H. Ferreira for technical assistance.

References

[1] Novoselov KS, Geim AK, Morozov SV, et al. Electric field effect in atomically thin carbon films. Science. 2004;306(5696): 666-669.

[2] Ferrari AC, Bonaccorso F, Fal'ko V, et al. Science and technology roadmap for graphene, related two-dimensional crystals, and hybrid systems. Nanoscale. 2015;7(11):4598-4810.

[3] Chung C, Kim Y-K, Shin D, Ryoo S-R, Hong BH, Min D-H. Biomedical applications of graphene and graphene oxide. Acc Chem Res. 2013;46(10):2211-2224.

[4] Sun X, Liu Z, Welsher K, et al. Nano-graphene oxide for cellular imaging and drug delivery. Nano Res. 2008;1(3):203-212.

[5] Hu W, Peng C, Luo W, et al. Graphene-based antibacterial paper. ACS Nano. 2010;4(7):4317-4323.

[6] Zhang L, Xia J, Zhao Q, Liu L, Zhang Z. Functional graphene oxide as a nanocarrier for controlled loading and targeted delivery of mixed anticancer drugs. Small. 2010;6(4):537-544.

[7] Akhavan O, Ghaderi E. Toxicity of graphene and graphene oxide nanowalls against bacteria. ACS Nano. 2010;4(10):5731-5736.

[8] Liu S, Zeng TH, Hofmann M, et al. Antibacterial activity of graphite, graphite oxide, graphene oxide, and reduced graphene oxide: membrane and oxidative stress. ACS Nano. 2011;5(9): 6971-6980.

[9] Ruiz ON, Fernando KAS, Wang B, et al. Graphene oxide: a nonspecific enhancer of cellular growth. ACS Nano. 2011;5(10): 8100-8107.

[10] Das MR, Sarma RK, Saikia R, Kale VS, Shelke MV, Sengupta P. Synthesis of

silver nanoparticles in an aqueous suspension of graphene oxide sheets and its antimicrobial activity. Colloids Surf B Biointerfaces. 2011;83(1):16-22.

[11] Santos CM, Tria MC, Vergara RA, Ahmed F, Advincula RC, Rodrigues DF. Antimicrobial graphene polymer (PVK-GO) nanocomposite films. Chem Commun (Camb). 2011;47(31): 8892-8894.

[12] Liao K-H, Lin YS, Macosko CW, Haynes CL. Cytotoxicity of graphene oxide and graphene in human erythrocytes and skin fibroblasts. ACS Appl Mater Interfaces. 2011;3(7):2607-2615.

[13] Wojtoniszak M, Chen X, Kalenczuk RJ, et al. Synthesis, dispersion, and cytocompatibility of graphene oxide and reduced graphene oxide. Colloids Surf B Biointerfaces. 2012;89:79-85.

[14] Liu S, Hu M, Zeng TH, et al. Lateral dimension-dependent antibacterial activity of graphene oxide sheets. Langmuir. 2012;28(33):12364-12372.

[15] Mangadlao JD, Santos CM, Felipe MJ, de Leon AC, Rodrigues DF, Advincula RC. On the antibacterial mechanism of graphene oxide (GO) Langmuir-Blodgett films. Chem Commun (Camb). 2015;51(14):2886-2889.

[16] Akhavan O, Ghaderi E, Esfandiar A. Wrapping bacteria by graphene nanosheets for isolation from environment, reactivation by sonication, and inactivation by near-infrared irradiation. J Phys Chem B. 2011;115(19):6279-6288.

[17] Hui L, Piao J-G, Auletta J, et al. Availability of the basal planes of graphene oxide determines whether it is antibacterial. ACS Appl Mater Interfaces. 2014;6(15):13183-13190.

[18] Zhang L, Xia J, Zhao Q, Liu L, Zhang Z. Functional graphene oxide as a nanocarrier for controlled loading and targeted delivery of mixed anticancer drugs.

Small. 2010;6(4):537-544.

[19] Sasidharan A, Panchakarla LS, Chandran P, et al. Differential nano-bio interactions and toxicity effects of pristine versus functionalized graphene. Nanoscale. 2011;3(6):2461-2464.

[20] Wang K, Ruan J, Song H, et al. Biocompatibility of graphene oxide. Nanoscale Res Lett. 2011;6:8.

[21] Chang Y, Yang S-T, Liu JH, et al. In vitro toxicity evaluation of graphene oxide on A549 cells. Toxicol Lett. 2011;200(3): 201-210.

[22] Sasidharan A, Panchakarla LS, Sadanandan AR, et al. Hemocompatibility and macrophage response of pristine and functionalized graphene. Small. 2012;8(8):1251-1263.

[23] Pinto AM, Gonçalves IC, Magalhães FD. Graphene-based materials biocompatibility: a review. Colloids Surf B Biointerfaces. 2013;111:188-202.

[24] Yang K, Li Y, Tan X, Peng R, Liu Z. Behavior and toxicity of graphene and its functionalized derivatives in biological systems. Small. 2013;9(9-10):1492-1503.

[25] Seabra AB, Paula AJ, de Lima R, Alves OL, Durán N. Nanotoxicity of graphene and graphene oxide. Chem Res Toxicol. 2014;27(2):159-168.

[26] Zhang W, Yan L, Li M, et al. Deciphering the underlying mechanisms of oxidation-state dependent cytotoxicity of graphene oxide on mammalian cells. Toxicol Lett. 2015;237(2):61-71.

[27] Paul W, Sharma CP. Blood compatibility and biomedical applications of graphene. Trends Biomater. Artif. Organs. 2011;25:91.

[28]. Singh SK, Singh MK, Nayak MK, et al. Thrombus inducing property of atomically thin graphene oxide sheets. ACS Nano. 2011;5(6):4987-4996.

[29] Jastrzębska AM, Kurtycz P, Olszyna AR. Recent advances in graphene family materials toxicity investigations. J Nanopart Res. 2012;14(12):1320-1341.

[30] Guo X, Mei N. Assessment of the toxic potential of graphene family nanomaterials. J Food Drug Anal. 2014;22(1):105-115.

[31] Hummers WS, Offeman RE. Preparation of Graphitic Oxide. Journal of the American Chemical Society, v. 80 (6), p. 1339, 1958.

[32] Estrade-Szwarckopf H. XPS photoemission in carbonaceuous materials: a “defect” peak beside the asymmetric peak. Carbon. 2004;42(8-9):1713-1721.

[33] Rozada R, Paredes JI, Villar-Rodil S, Martínez-Alonso A, Tascón JM. Towards full repair of defects in reduced graphene oxide films by two-step graphitization. Nano Res. 2013;6(3): 216-233.

[34] Yang D, Velamakanni A, Bozoklu G, et al. Chemical analysis of graphene oxide films after heat and chemical treatments by X-ray photoelectron and micro-Raman spectroscopy. Carbon. 2009;47(1):145-152.

3. Chapter II

Effects of nitrogen-doped multi-wall carbon nanotubes on murine fibroblasts

Carbon nanotubes (CNTs) exhibit a number of unique properties that make them attractive for biomedical applications. However, the cytotoxicity of CNTs is a critical issue to human safety. The effect of nitrogen-doped multi-wall carbon nanotubes (CN_x) on the proliferation of NIH-3T3 murine fibroblasts is presented. CNTs were dispersed in distillated water and incubated with mammalian cells in order to evaluate their toxicity. Also, the influence of factors such as dosage (7 and 70 µg/ml), exposure time (24 to 96 h), and the exposure route (before and after cell liftoff) on the cell proliferation was evaluated. When the CN_x were simultaneously incubated with the cells, the control culture reached a maximum cell concentration of $1.3x10^5 \pm 3.4x10^4$cells per well at 96 h, whereas in cultures with 7 µg/mL reached $2.6x10^4 \pm 5.3x10^3$ cells, and a drastic no cell survive was observed at 70 µg/mL of CN_x. The CN_x that were added 24h after cell dissociation showed that live cells decreased, with a cell concentration of $9.6x10^4 \pm 9x10^3$for 7 µg/mL and $5.5x10^4 \pm 9.5x10^3$ for 70 µg/mL, in contrast to control cultures with $1.1x10^6 \pm 1.5x10^4$. The results showed that the CN_x had cytotoxic effects depending on the concentration and exposure route. Furthermore, concentrations of 7 µg/ml of these nanomaterials seemed to be well tolerated by the cells, and they could be used in biomedical applications.

Effects of nitrogen-doped multi-wall carbon nanotubes on murine fibroblasts

J G Munguía-Lopez, E Muñoz-Sandoval, J Ortiz-Medina, F J Rodriguez-Macias, A De Leon-Rodriguez.

Journal of Nanomaterials

DOI: 10.1155/2015/801606

1. Introduction

A wide range of nanomaterials has been developed for several applications over the past few years. Due to their physical, chemical, electrical and thermal properties, and since their discovery in 1991[1] carbon nanotubes (CNTs) have shown a potential for use in drug delivery, biosensor, antimicrobial nanocomposite film and cellular scaffolding. CNTs are tiny hollow cylinders, made from a single, double or several layers of graphene that are concentrically arranged and capped by fullerene hemispheres. They have diameters ranging from a few nanometers, 0.4 to 2 nm for single walled carbon nanotubes (SWCNTs), 2 to 200 nm for multi-wall carbon nanotubes (MWCNTs), and lengths ranging from hundreds of nanometers to micrometers [1-3]. Since CNTs have an asbestos-like shape, research into their toxicity and potential risks to human health has been intensified [4-7].

Studies on cellular response in non-functionalized or functionalized (addition of functional groups on a graphite surface) MWCNT have been extensive. Chemical doping (carbon atoms substitution) with nitrogen of CNTs (CN_x) was suggested to have positive effects on mice survival [8] and showed an

improvement in cell-adhesion strength, viability and proliferation of mammalian cells [3,9], in contrast with the MWCNT. However, cytotoxic effects of CN_x have also been reported, where long length CN_x were more toxic than others functionalized CNTs [10]. Researches have demonstrated that cells exhibited variable responses to CNTs depending on different factors such as the method of synthesis, impurities, length and diameter, type (pristine, functionalized, doped), degree of dispersion/agglomeration, dispersant, CNT concentration, time exposure, cellular type and protein adsorption, [2,5,6,8,11,12]. Due to the inconsistency in CN_x biocompatibility, more studies regarding to cell response to these nanomaterials are necessary.

In the body, cell motility and wound healing is carried out by cell detachment, which is generated by proteolytic processes using endogenous proteases [13]. One of the most common enzymatic methods used for cell detachment in adherent-cell-subculture is trypsinization, trypsin cuts adhesion proteins to yield disaggregated cells with a rounded appearance. Although many cells are able to tolerate trypsin digestion during a short period of time, trypsinization causes cell stress affecting cytoskeleton proteins that are involved in regulating cell adhesion, stability and elasticity [14-16].

CNTs have the capacity to adsorb a wide range of proteins, especially those rich in histidine, tryptophan and phenylalanine [12], also to adhesion proteins from extracellular matrix (fibronectins, collagen) and transmembrane-proteins (integrins) [17]. Since enzymatic cell detachment can produce residual fragments of adhesion proteins. These fragments could interact with CNTs altering the extracellular matrix metabolism which is regulated by a complex mechanism including cell-cell and

cell-matrix interactions [13,17]. For this reason, the knowledge of cell-CNTs interactions is essential for cell scaffold development that is used in tissue regeneration.

The aim of this study was to evaluate the possible toxic effect of CN_x on NIH-3T3 murine fibroblast stressed by enzymatic detachment and non-stressed cells. In which, a natural cell detachment stress was simulated by a trypsin incubation during a short period of time. Exposure route was defined in this work as the way to add nanomaterials to cell cultures (stressed and non-stressed cells). Besides several parameters are required to determine if new materials are safe for biomedical use, the effects of CN_x concentration and exposure time were also evaluated.

2. Materials and methods

2.1. Synthesis, purification and characterization of CN_x

In this way, CN_x were synthesized by using the chemical vapor deposition (CVD) method. As a chemical precursor 2.5 wt% ferrocene in benzylamine was used, the solution was placed into a reservoir and atomized. The aerosol was carried by an Argon flow at 2.5 L/min into a quartz tube 100 cm in length, placed inside of ~~a~~ two tubular furnaces heated at 850°C. After 30 min of synthesis, the quartz tube was then cooled at room temperature and the CN_x were collected by internal scraping. Then, the pristine CN_x were purified and dispersed by using a pulsed probe sonicator in water under reflux, followed by a reflux in 6M HCl and filtration.

Consequently, the purified CN_x were analyzed by scanning electron microscopy (SEM) as follows: first, the nanomaterials were pounded into a whole powder and separated into equal portions. Then, each portion was loaded into pins and visualized by SEM (Philips-XL 30 SFEG; Dual Beam (FIB/SEM) FEI-Helios Nanolab 600 equipped with an EDX detector) to determine lengths, diameters and chemical composition of CN_x. Raman characterization was performed using a laser of 633 nm in a Raman Renishaw Micro-Raman equipment.

2.2. Preparation of dispersion of purified CN_x

Stocks of purified CN_x were dispersed at 1 mg/mL in: 1) basal-IMDM [Iscove`s Modified Dulbecco`s Medium (IMDM) (SIGMA) pH 7.2 supplemented with 10% fetal bovine serum (GIBCO), 100 U/mL penicillin, 100 µg/mL streptomycin and 0.25 µg/mL amphotericin B (SIGMA)], 2) ethanol, and 3) distillated water. Then, the samples were sonicated by an ultrasonic bath at 42 kHz and100 W (Branson 2510 Ultrasonic Cleaner), at 40ºC for 8 h, having as a result stable dispersions; these conditions were strong enough to obtain no visible agglomerates of purified CN_x. Finally, all the stocks were stored at 4°C until further use.

2.3. Cytotoxicity assays

The effects of purified CN_x on the viability of NIH-3T3 murine fibroblast were evaluated by using the Trypan-blue exclusion method. Briefly, the cells were defrosted and cultured in a basal-IMDM, using 24-well plates (Corning) over a period of 72 h in a humidity chamber at 37°C and CO_2 5% (Shell-Lab). After three passes, when 80% of cellular confluence was reached, the cells were twice-

washed gently with PBS (pH 7.2) and then harvested by incubation with trypsin-EDTA (0.25%-1X, GIBCO) for 10 min. Cell suspensions with a density of $2x10^3$ cells per well were added into 96-well plates in absence or presence of purified CN_x at final concentrations of 7 and 70 µg/mL dispersed in basal-IMDM, ethanol or distillated water. For exposure route experiments, purified CN_x were added: 1) immediately after cell dissociation (stressed cells) or 2) fibroblasts were firstly incubated for 24 h and then purified CN_x were added into each well (non-stressed cells). Due to ethanol toxicity, CNTs dispersed in ethanol were incubated alone into 96-well plates for 24 h at 37°C to evaporate the ethanol; then, fibroblasts were immediately placed into each well after cell liftoff.

Samples were twice washed gently with PBS, incubated with trypsin for 6 min and cells were counted by using the Trypan blue method. During the 96 h of exposure with the nanomaterial, samples were taken each 24 h. NIH-3T3 cell cultures without nanomaterials were used as control. To avoid variation on purified CN_x concentration in cell cultures when medium was changed, kinetics were carried out using a working volume of 250 µL without medium replacement.

2.4. Statistics

The data is presented as the mean ± standard deviation, with a statistical comparison of one and two ways ANOVA. We used Dunnett´s post-tests to compare treatments with control groups, and *p*-values < 0.05 were considered significant. All experiments were done in triplicate.

3. Results and discussion

3.1. Determination of length and diameter of purified CN_x

Figure1 shows SEM micrographs and size distribution of purified CN_x. Micrographs by the XL30 and Helios are shown in Figure 1a and 1c, respectively. A few bundles were found in purified CN_x samples to determine the lengths of nanomaterials (Figure 1a). The length range were 10 to 130 µm, being the most abundant lengths of 40-50µm (Figure 1b). In micrographs of purified CN_x, the nanomaterials seemed like to have similar diameters (Figure 1c), but after an analysis with the Helios microscopy, the diameter sizes were around 10-80 nm, with a diameter predominance of 20-40 nm (Figure 1d).

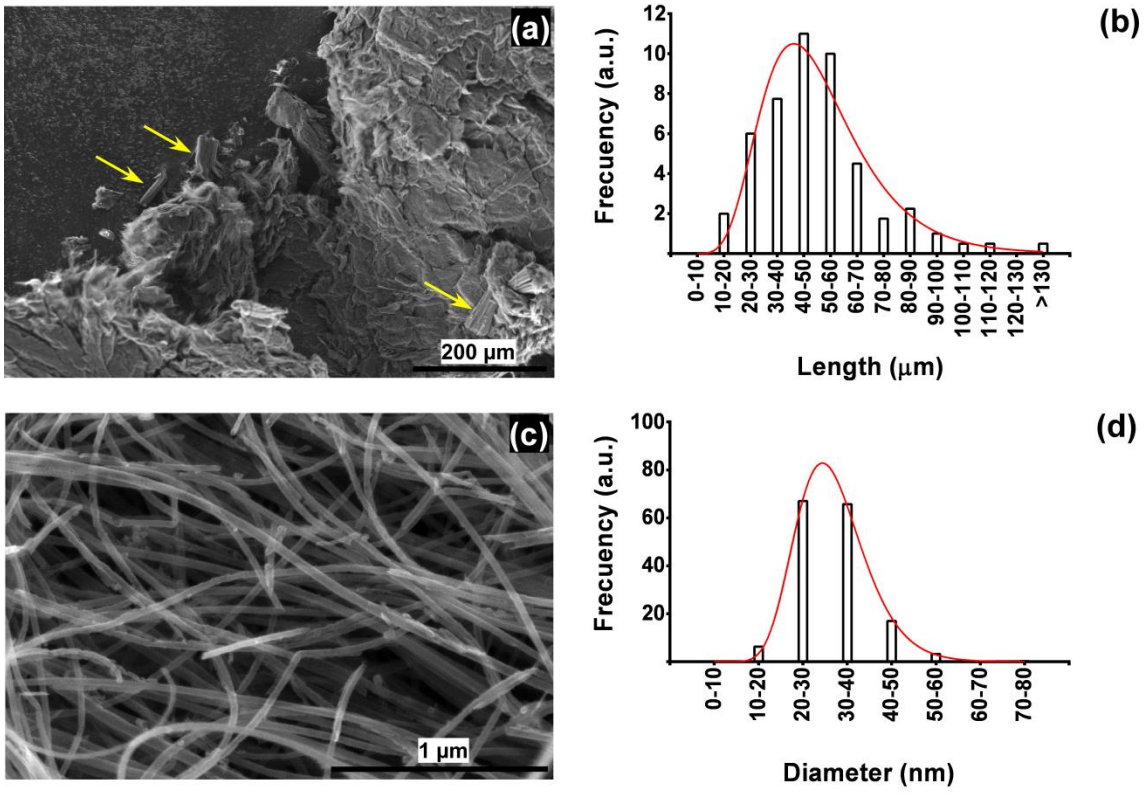

Figure 1. SEM micrographs of CN_x morphology and size distribution. Lengths were obtained from bundles of purified CN_x (a, pointed with yellow arrows) and plotted to

generate distribution patterns. Diameters were obtained from individual tubes from Helios SEM images (c) and distribution was plotted (d).

Nanomaterial sizes were obtained from their own bundles and short “fibrous” structures (Figure 2). The numbers of bundles among different samples of purified CN_x were few (around 38 bundles) (Figure 2a-c, yellow arrows) as well as in between the same sample (Figure 2d-f). Since purified CN_x samples were mostly agglomerated in big structures by dry process, the determination of their total lengths was difficult, thus only the bundles lengths were reported. The presence of amino groups in the CN_x could be the reason to find less bundles in samples, due to their weaker van der Waals, resulting in lower formation of bundles [8].

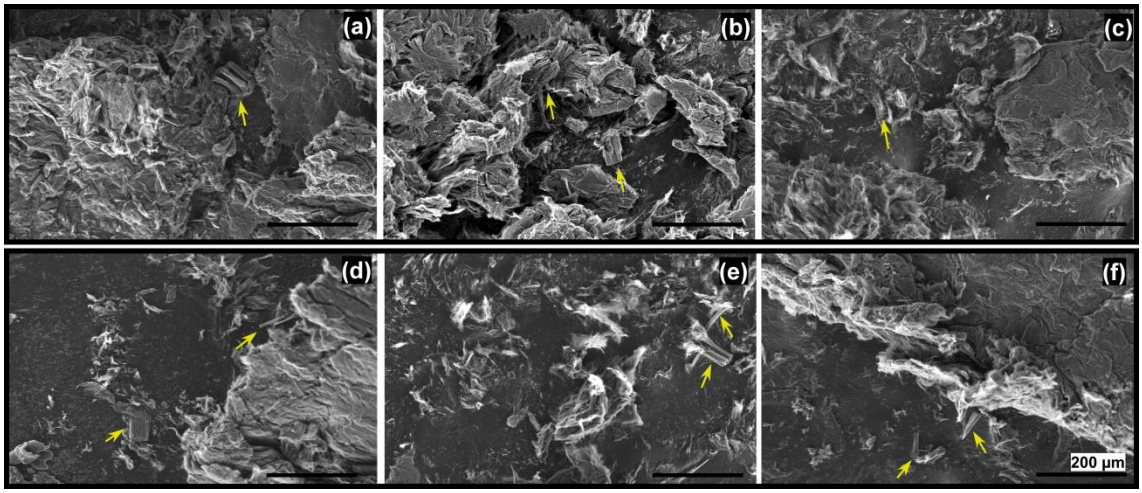

Figure 2. Representative SEM images of whole sample dry purified CN_x. (a-c) different parts of sample from whole sample, (d-f) same sample different fields. Yellow arrows pointed bundles of purified CN_x. Big structures are agglomerates of CNTs which were easy to disperse in water.

3.2. Raman and EDX characterization of pristine and purified CN_x

Figure 3 shows the Raman spectra of pristine and purified CN_x plotted between 100 and 3000 cm^{-1}. The bands D (defect mode), G (graphite mode), G'(second order mode) situated at 1340, 1592 and 2686 cm^{-1}, respectively, are the typical peaks corresponding to carbonaceous materials. In the case of purified CN_x, the shifting to higher frequencies of G band suggests that nitrogen doping decreased. The I_D/I_G values were 1.1488 and 1.2815 for pristine and purified CN_x, respectively. This increasing in I_D/I_G ratio has been suggested as an evidence for sidewall functionalization of CNTs [18,19].

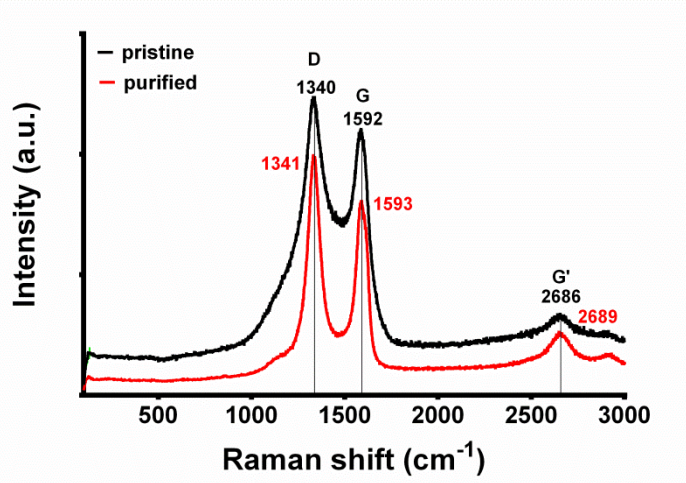

Figure 3. Raman spectra of pristine and purified CN_x at 633 nm.

Respect to chemical composition of our CN_x (pristine and purified), EDX analysis was carried out. Figure 4 and Figure 5 show the SEM images and their respective EDX graphs. The average quantity of iron in pristine samples was of 2.22 wt% (Figure 4), which decreased after purification process to 0.61 wt% (Figure 5), indicating the elimination of this contaminant.

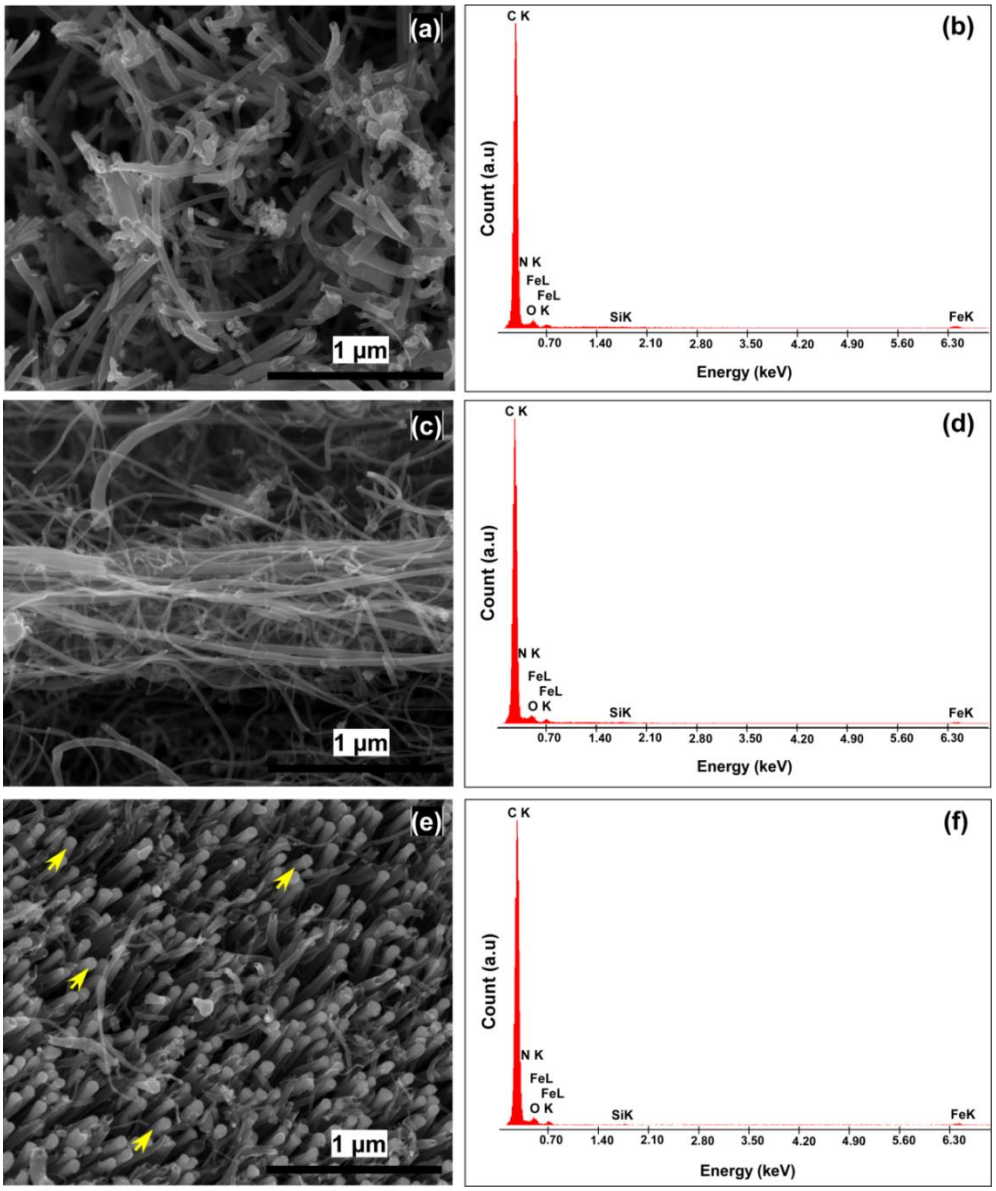

Figure 4. SEM micrograph of pristine CN_x taken form tip (a), middle (c) and root part (e) and their respective EDX analysis (b,d,f). The quantity of iron was of 2.85 wt %, 1.82 wt% and 2 wt% for tip, middle and root part, respectively. In average the other elements was: carbon: 83.04 wt%, nitrogen: 9.51 wt%, oxygen: 5.15 wt%. Yellow arrows pointed some iron particles found in the root part.

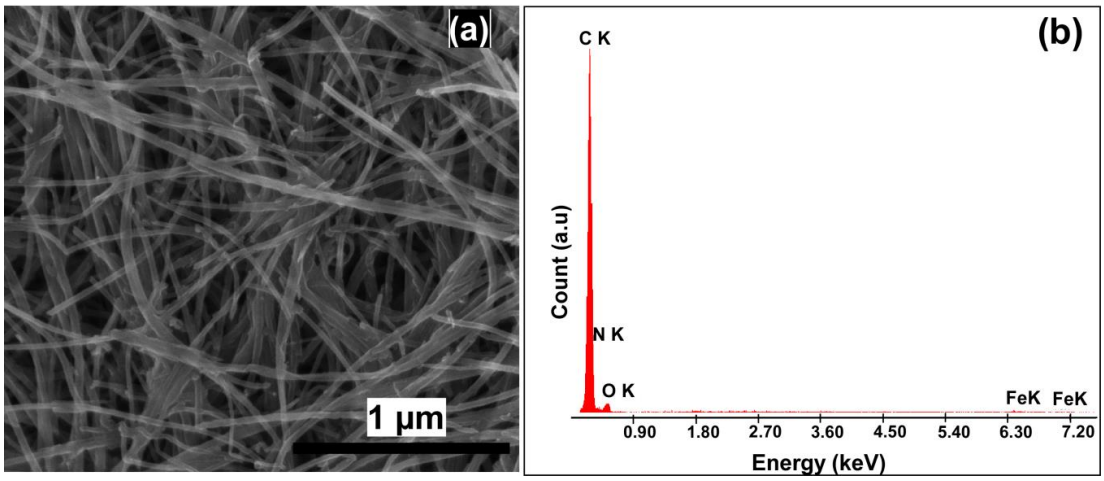

Figure 5. SEM micrograph (a) and EDX analysis (b) of purified CN_x. The chemical composition of CN_x was carbon: 84.88 wt%, nitrogen: 8.07 wt%, oxygen: 6.45 wt%, and iron: 0.61 wt%. The iron quantity decreased in purified CN_x compared to pristine CN_x.

3.3. Effect of purified CN_x on murine fibroblasts non-stressed and stressed

NIH-3T3 murine fibroblasts were used as a model for stromal cells, which can be found in matrix and connective tissue throughout the body. To evaluate the effect of the dispersant medium, CN_x were dispersed in three different solutions (basal-IMDM, distillated water, and ethanol). Figure 6 shows the comparison among growth kinetic of fibroblasts incubated with CN_x dispersed in different mediums. A drastic decrease of cell proliferation was founded when 7 µg/mL CN_x dispersed in basal-IMDM or distillated water was added immediately after cell tripsinization, this comparing to ethanol-dispersed CN_x (Figure 6a), enhancing the toxic effect when nanomaterial concentration and time were increased (Figure 6b). For CN_x incubated 24 h after cell liftoff, cells did not show significant differences among ethanol, basal-IMDM and distillated water using 7 µg/mL CN_x (Figure 6c) or

70 µg/mL (Figure 6d), except for 48 h samples. These results suggest that the toxic effect of CN_x on fibroblast is time, concentration and exposure-way dependent.

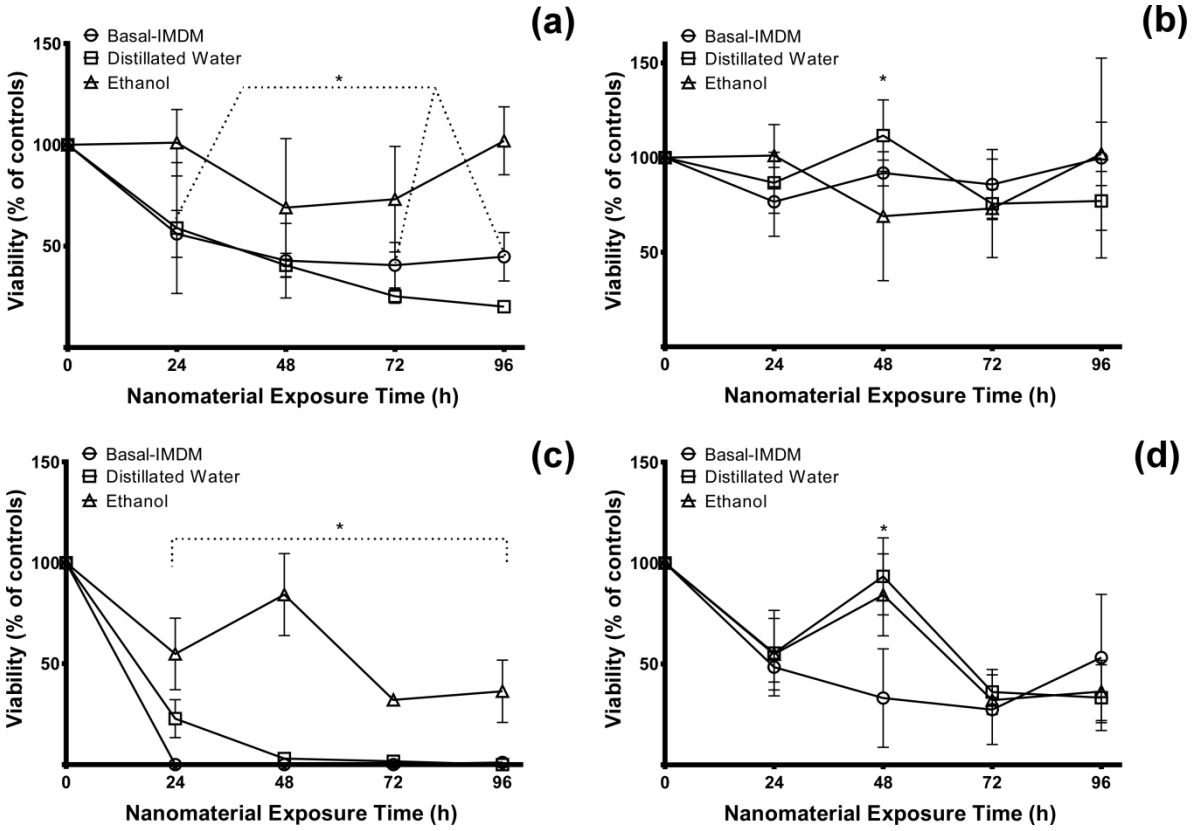

Figure 6. Viability of NIH-3T3 murine fibroblast incubated with CN_x dispersed in basal-IMDM, distillated water or ethanol. CN_x 7 µg/mL (A) or 70 µg/mL (B) incubated immediately after cell liftoff. CN_x 7 µg/mL (C) or 70 µg/mL (D) incubated 24 h post cell dissociation. Data are normalized respect to control cells and are presented as mean ± SD. * indicates significant difference compare among dispersants ($P < 0.05$). $n \geq 3$.

Dispersion/agglomeration of CNTs and dispersant solvents play an important role in cytotoxicity [5, 6, 20]. According to our results, CN_x dispersed in basal-IMDM, distillated water, and ethanol showed different degrees of toxicity, which are also related with exposure way. CN_x were less toxic when dispersed in

ethanol compared to basal-IMDM and distillated water dispersants. This might be explained by the chemical properties of the dispersant mediums as well as the intrinsic nanomaterial properties that can produce the formation of bundles of CNTs [21,22]. Nevertheless, we did not find macroscopic bundles in any of three solutions employed.

CN_x dispersed in ethanol were used as scaffold-like structure for cell growth and the interaction with cells could be lower compare with basal-IMDM and distillated water. Furthermore, since CN_x can adsorb proteins for culture medium (basal-IMDM) modifying the physicochemical properties of nanomaterials, the next experiments were carried put using CN_x dispersed in distillated water.

Figure 7 shows the kinetics of fibroblasts growth with water-dispersed purified CN_x. When the cells were incubated simultaneously with the purified CN_x, the control culture (without purified CN_x) reached a maximum live cell concentration of $1.3x10^5 \pm 3.4x10^4$cells per well at 96 h, meanwhile cultures with 7 µg/mL reached $2.6x10^4 \pm 5.3x10^3$ cells, and a drastic no cell survive was at 70 µg/mL of purified CN_x (Figure 7a). Purified CN_x added after 24 h of cell dissociation showed a decreased live cell, with a cell concentration of $9.6x10^4 \pm 9x10^3$for 7 µg/mL and $5.5x10^4 \pm 9.5x10^3$ for 70µg/mL, compared to control culture with $1.1x10^6 \pm 1.5x10^4$, at 96 h of exposure (Figure 7b). Results suggest that nanomaterials exhibited toxic effects, in concentration and exposure route-dependent. No effects concerning on time exposure were observed.

Murine fibroblasts were susceptible to purified CN_x in concentration and exposure route-dependent manner. As previously mentioned, toxicity/biocompatibility of CNTs (SWCNT, MWCNT, functionalized CNTs) on

mammalian cells depends on different factors [6,23,24]. A lot of data research has shown the toxicity of CNTs [25-28] in human mesenchymal stem cells [29], 3T3 L1 fibroblasts [30], 3T3 fibroblast, telomerase, immortalized human bronchiolar epithelial cells, RAW 264.7 macrophages [6], mouse fibroblast cell L929 and mouse adipose-derived stem cells [3], but, to our knowledge, no experiments about the effects of CNTs have been reported on mammalian cells stressed by enzymatic detachment, which is a natural process in the body.

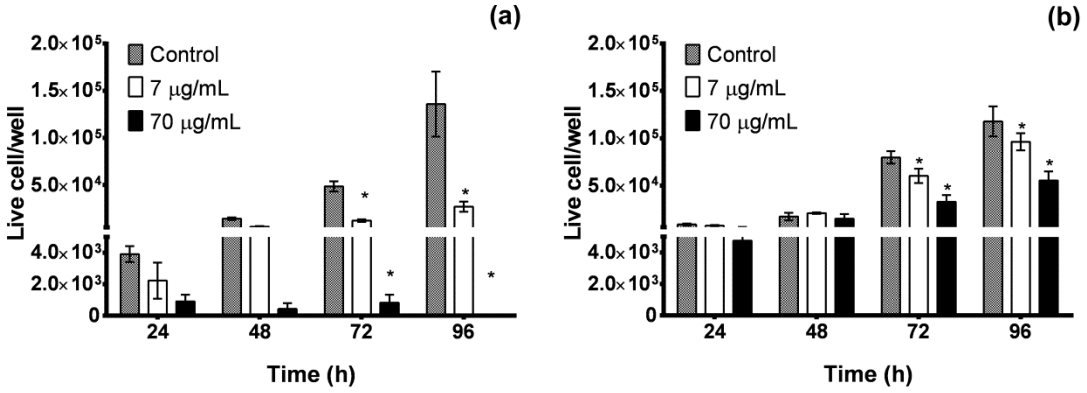

Figure 7. Effects of water-dispersed purified CN_x on NIH-3T3 murine fibroblast proliferation. Purified CN_x were incubated with fibroblast immediately after cell dissociation (a) or 24 h after cellular liftoff (b). Data are presented as mean ± SD. * indicates significant difference compare to untreated controls ($P < 0.05$), n ≥ 3.

Treatments with water-dispersed purified CN_x immediately added after cell liftoff (stressed cells by trypsin) were more toxic than purified CN_x added after 24 h of cell dissociation, suggesting that exposure route factor had negative effects on cell proliferation. This could be explained due to interaction of CNTs with residual fragments of adhesion proteins generated after cell trypsinization [12], which can still adversely affect over cytoskeleton proteins that are involved in regulating cell adhesion, stability and elasticity [14-16,31]. However, in this work only the cell

proliferation was evaluated as a first approach to determine the purified CN_x toxicity; therefore, more studies are required and are currently underway.

Specific growth rate (μ) was calculated from exponential growth phase of fibroblasts and used as a parameter to evaluate the effect of purified CN_x on cell growth. In 7 μg/mL of dispersed-water purified CN_x incubated simultaneously with cells, the μ was lower (0.031±0.004 h^{-1}) than control cultivation (0.048±0.004 h^{-1}); since no cells survived at 70 μg/mL, μ was not determined. Concerning to incubation of cells with nanomaterials for 24 h after cell liftoff, values of μ were 0.044±0.002 h^{-1} for control culture, 0.037 ± 0.002 h^{-1} and 0.035±0.001 h^{-1} for purified CN_x at 7 and 70 μg/mL, respectively; both concentrations affected negatively the μ. Results confirm a cytotoxic effect that is concentration and exposure route dependent.

3.4. Morphology diversity of pristine CN_x

In several investigations about cytotoxic effects of CNTs, these nanomaterials are purchased from companies, which are synthesized by CVD. However, researchers have reported different patterns in the bulk growth of CNTs during their synthesis, showing that the CVD method produces a wide range of CNTs morphologies with varieties of lengths and diameters [32]. In preliminary results, different fractions from the same batch were analyzed by SEM showing a wide collection of pristine CN_x sizes (Figure 8), with lengths of range between 30-250 μm (Figure 8a) and diameters of 24-60 nm (Figure 5b). Figure 9 shows a SEM micrograph gallery of the morphology of the different pristine CN_x fractions, where the variations in lengths (Figure 9a-c) and diameters (Figure 9d-f) among three

fractions are clear. The morphology variation of CNTs could be the reason to contradictory results regarding to cytotoxic/biocompatibility of CNTs reported in several researches, and this issue should be studied in order to understand the relationship between CNTs and mammalian cell response.

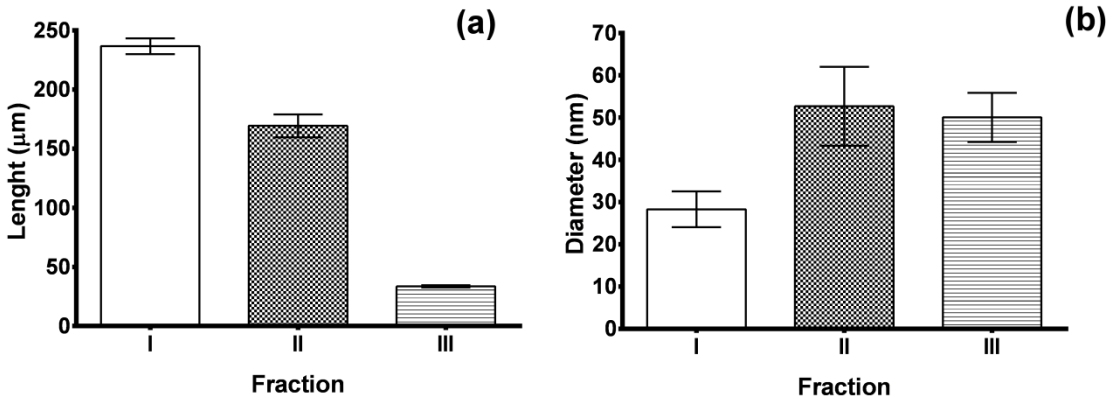

Figure 8. Variations in pristine CN_x length (a) and diameters (b) obtained from three different fractions of the same batch.

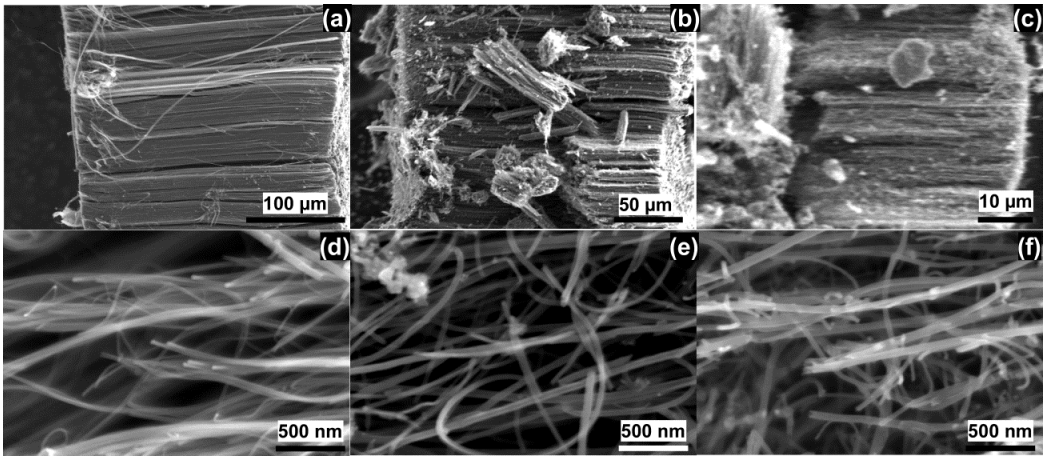

Figure 9. Electron micrograph gallery depicting the size diversity of pristine CN_x found in three different locations (fractions) from the quartz tube. Fraction: I (a, d), II (b, e), III (c, f). Lengths (a-c) and diameters (d-f) of CN_x.

4. Conclusion

Finally, purified CN_x have a cytotoxicity effect that is directly dependent–on their concentration, also purified CN_x showed a more toxic effect in enzymatic stressed cells than in the non-stressed. Since cells in the body are exposed to enzymatic processes of detachment, the present study of the effects over-stressed cells by enzymatic digestion is important for the development and potential uses of these nanomaterials in the biomedical field. On the other hand, chemical synthesis of pristine CN_x yields heterogenic product with substantial differences on length and diameter size, which have distinctive cytotoxic effects on the proliferation of NIH-3T3 cells. There is still a long path that we must take in order to understand the relationship between nanomaterials and mammalian cells. However, concentrations up to 7 µg/mL of nanotubes are well tolerated by the cells, and they could be used in biomedical applications.

Acknowledgments

We thank to The Marcos Moshinsky Foundation and CONACYT-Mexico grants 107082 (JFRM), CB-2013-220744 (EMS) for partial funding. J. Gil Munguía-López thanks to CONACYT for his scholarship 250279. We also thank L. Aldana for the English review and L. Ordoñez, B.A. Rivera-Escoto, G.J. Labrada-Delgado for their technical assistance.

References

[1] S. Iijima, "Helical microtubules of graphitic carbon", Nature. 354, 56-58 (1991).

[2] H. F. Cui, S. K. Vashist, K. Al-Rubeaan, J. H. Luong and F. S. Sheu, "Interfacing carbon nanotubes with living mammalian cells and cytotoxicity issues", Chem Res Toxicol. 23 (7), 1131-47 (2010). http://dx.doi.org/10.1021/tx100050h.

[3] M. L. Zhao, D. J. Li, L. Yuan, Y. C. Yue, H. Liu and X. Sun, "Differences in cytocompatibility and hemocompatibility between carbon nanotubes and nitrogen-doped carbon nanotubes", Carbon. 49 (9), 3125-3133 (2011). http://dx.doi.org/10.1016/j.carbon.2011.03.037.

[4] X. Wang, T. Xia, M. C. Duch, Z. Ji, H. Zhang, R. Li, B. Sun, S. Lin, H. Meng, Y.-P. Liao, M. Wang, T.-B. Song, Y. Yang, M. C. Hersam and A. E. Nel, "Pluronic F108 Coating Decreases the Lung Fibrosis Potential of Multiwall Carbon Nanotubes by Reducing Lysosomal Injury", Nano Letters. 12 (6), 3050-3061 (2012). http://dx.doi.org/10.1021/nl300895y.

[5] H. Haniu, Saito, Matsuda, Kim, Park, T. Tsukahara, Usui, Aoki, Shimizu, Ogihara, Hara, Takanashi, Okamoto, Ishigaki, Nakamura and Kato, "Effect of dispersants of multi-walled carbon nanotubes on cellular uptake and biological responses", International Journal of Nanomedicine. 6, 3295–3307 (2011). http://dx.doi.org/10.2147/ijn.s26573.

[6] S. K. Sohaebuddin, P. T. Thevenot, D. Baker, J. W. Eaton and L. Tang, "Nanomaterial cytotoxicity is composition, size, and cell type dependent", Particle and Fibre Toxicology. 7 (1), 22 (2010). http://dx.doi.org/10.1186/1743-8977-7-22.

[7] A. Kunzmann, B. Andersson, T. Thurnherr, H. Krug, A. Scheynius and B. Fadeel, "Toxicology of engineered nanomaterials: Focus on biocompatibility, biodistribution and biodegradation", Biochimica et Biophysica Acta (BBA) - General

Subjects. 1810 (3), 361-373 (2011). http://dx.doi.org/10.1016/j.bbagen.2010.04.007.

[8] J. C. Carrero-Sanchez, A. L. Elias, R. Mancilla, G. Arrellin, H. Terrones, J. P. Laclette and M. Terrones, "Biocompatibility and toxicological studies of carbon nanotubes doped with nitrogen", Nano Lett. 6 (8), 1609-16 (2006). http://dx.doi.org/10.1021/nl060548p.

[9] D. J. Li and L. F. Niu, "Influence of N atomic percentages on cell attachment for CNx coatings", Bulletin of Materials Science. 26 (4), 371-375 (2003). http://dx.doi.org/10.1007/BF02711178.

[10] S. Boncel, K. H. Muller, J. N. Skepper, K. Z. Walczak and K. K. Koziol, "Tunable chemistry and morphology of multi-wall carbon nanotubes as a route to non-toxic, theranostic systems", Biomaterials. 32 (30), 7677-86 (2011). http://dx.doi.org/10.1016/j.biomaterials.2011.06.055.

[11] D. Li, L. Yuan, Y. Yang, X. Deng, X. Lü, Y. Huang, Z. Cao, H. Liu and X. Sun, "Adsorption and adhesion of blood proteins and fibroblasts on multi-wall carbon nanotubes", Science in China Series C: Life Sciences. 52 (5), 479-482 (2009). http://dx.doi.org/10.1007/s11427-009-0049-9.

[12] X. Cai, R. Ramalingam, H. S. Wong, J. Cheng, P. Ajuh, S. H. Cheng and Y. W. Lam, "Characterization of carbon nanotube protein corona by using quantitative proteomics", Nanomedicine. 9 (5), 583-93 (2013). http://dx.doi.org/10.1016/j.nano.2012.09.004.

[13] R. J. McAnulty, "Fibroblasts and myofibroblasts: Their source, function and role in disease", The International Journal of Biochemistry & Cell Biology. 39 (4), 666-671 (2007). http://dx.doi.org/10.1016/j.biocel.2006.11.005.

[14] Q. Zheng, S. M. Iqbal and Y. Wan, "Cell detachment: post-isolation challenges", Biotechnol Adv. 31 (8), 1664-75 (2013). http://dx.doi.org/10.1016/j.biotechadv.2013.08.013.

[15] H. E. Canavan, X. Cheng, D. J. Graham, B. D. Ratner and D. G. Castner, "Cell sheet detachment affects the extracellular matrix: A surface science study comparing thermal liftoff, enzymatic, and mechanical methods", Journal of Biomedical Materials Research Part A. 75A (1), 1-13 (2005). http://dx.doi.org/10.1002/jbm.a.30297.

[16] H. L. Huang, H. W. Hsing, T. C. Lai, Y. W. Chen, T. R. Lee, H. T. Chan, P. C. Lyu, C. L. Wu, Y. C. Lu, S. T. Lin, C. W. Lin, C. H. Lai, H. T. Chang, H. C. Chou and H. L. Chan, "Trypsin-induced proteome alteration during cell subculture in mammalian cells", J Biomed Sci. 17, 36 (2010). http://dx.doi.org/10.1186/1423-0127-17-36.

[17] J. P. Kaiser, T. Buerki-Thurnherr and P. Wick, "Influence of single walled carbon nanotubes at subtoxical concentrations on cell adhesion and other cell parameters of human epithelial cells", Journal of King Saud University - Science. 25 (1), 15-27 (2013). http://dx.doi.org/10.1016/j.jksus.2012.06.003.

[18] S. Lee, J.-W. Peng and C.-H. Liu, "Raman study of carbon nanotube purification using atmospheric pressure plasma", Carbon. 46 (15), 2124-2132 (2008). http://dx.doi.org/10.1016/j.carbon.2008.09.029.

[19] S. Banerjee and S. S. Wong, "Rational Sidewall Functionalization and Purification of Single-Walled Carbon Nanotubes by Solution-Phase Ozonolysis", The Journal of Physical Chemistry B. 106 (47), 12144-12151 (2002). http://dx.doi.org/10.1021/jp026304k.

[20] Wick P, Manser P, Limbach L, Dettlaffweglikowska U, Krumeich F, Roth S, et al. The degree and kind of agglomeration affect carbon nanotube cytotoxicity. Toxicology Letters. 2007;168:121-31.

[21] Kim JS, Song KS, Lee JH, Yu IJ. Evaluation of biocompatible dispersants for carbon nanotube toxicity tests. Archives of Toxicology. 2011;85:1499-508.

[22] Buford MC, Hamilton RF, Holian A. A comparison of dispersing media for various engineered carbon nanoparticles. Particle and Fibre Toxicology. 2007;4:6.

[23] L. Meng, A. Jiang, R. Chen, C. Z. Li, L. Wang, Y. Qu, P. Wang, Y. Zhao and C. Chen, "Inhibitory effects of multiwall carbon nanotubes with high iron impurity on viability and neuronal differentiation in cultured PC12 cells", Toxicology. 313 (1), 49-58 (2013). http://dx.doi.org/10.1016/j.tox.2012.11.011.

[24] P. M. Raja, J. Connolley, G. P. Ganesan, L. Ci, P. M. Ajayan, O. Nalamasu and D. M. Thompson, "Impact of carbon nanotube exposure, dosage and aggregation on smooth muscle cells", Toxicol Lett. 169 (1), 51-63 (2007). http://dx.doi.org/10.1016/j.toxlet.2006.12.003.

[25] C. L. Ursini, D. Cavallo, A. M. Fresegna, A. Ciervo, R. Maiello, G. Buresti, S. Casciardi, F. Tombolini, S. Bellucci and S. Iavicoli, "Comparative cyto-genotoxicity assessment of functionalized and pristine multiwalled carbon nanotubes on human lung epithelial cells", Toxicology in Vitro. 26 (6), 831-840 (2012). http://dx.doi.org/10.1016/j.tiv.2012.05.001.

[26] M. Bottini, S. Bruckner, K. Nika, N. Bottini, S. Bellucci, A. Magrini, A. Bergamaschi and T. Mustelin, "Multi-walled carbon nanotubes induce T lymphocyte apoptosis", Toxicology Letters. 160 (2), 121-126 (2006). http://dx.doi.org/10.1016/j.toxlet.2005.06.020.

[27] D. Liu, C. Yi, D. Zhang, J. Zhang and M. Yang, "Inhibition of proliferation and differentiation of mesenchymal stem cells by carboxylated carbon nanotubes", ACS Nano. 4 (4), 2185-95 (2010). http://dx.doi.org/10.1021/nn901479w.

[28] F. Witzmann and N. Monteiroriviere, "Multi-walled carbon nanotube exposure alters protein expression in human keratinocytes", Nanomedicine: Nanotechnology, Biology and Medicine. 2 (3), 158-168 (2006). http://dx.doi.org/10.1016/j.nano.2006.07.005.

[29] E. Mooney, P. Dockery, U. Greiser, M. Murphy and V. Barron, "Carbon nanotubes and mesenchymal stem cells: biocompatibility, proliferation and differentiation", Nano Lett. 8 (8), 2137-43 (2008). http://dx.doi.org/10.1021/nl073300o.

[30] J. Meng, M. Yang, L. Song, H. Kong, C. Y. Wang, R. Wang, C. Wang, S. S. Xie and H. Y. Xu, "Concentration control of carbon nanotubes in aqueous solution and its influence on the growth behavior of fibroblasts", Colloids and Surfaces B: Biointerfaces. 71 (1), 148-153 (2009). http://dx.doi.org/10.1016/j.colsurfb.2009.01.020.

[31] R. Umegaki, M. Kino-oka and M. Taya, "Assessment of cell detachment and growth potential of human keratinocyte based on observed changes in individual cell area during trypsinization", Biochemical Engineering Journal. 17 (1), 49-55 (2004). http://dx.doi.org/10.1016/s1369-703x(03)00124-4.

[32] S. S. Meysami, F. Dillon, A. A. Koós, Z. Aslam and N. Grobert, "Aerosol-assisted chemical vapour deposition synthesis of multi-wall carbon nanotubes: I. Mapping the reactor", Carbon. 58, 151-158 (2013). http://dx.doi.org/10.1016/j.carbon.2013.02.044.

4. Chapter III

Heterogeneity of nitrogen-doped multiwalled carbon nanotubes produced by chemical vapor deposition and their effect on mammalian cells

Carbon nanotubes (CNTs) exhibit properties that make them attractive for biomedical applications. However, the cytotoxicity of CNTs is a critical issue for the human safety. Chemical modification of CNTs by doping with nitrogen (CN_x) has presented positive effects on cellular biocompatibility compared with other kind of CNTs. It has been reported that synthesis of CNTs by chemical vapor deposition (CVD) produces heterogeneous samples with different morphologies and dimensions, which generate different response in cells. In this work, we evaluated the effect of CN_x on human hematopoietic stem cells as well as murine fibroblasts. CN_x synthesized by CVD and recovered from different zones were incubated at concentration of 0.07-70 µg/mL with mammalian cells during 5 days. We found that CN_x belonging to high region of production (CN_x-HR) were biocompatible with both kind of cells, whereas, CN_x from middle region (CN_x-MR) were toxic for cells. Furthermore, CN_x-HR were embedded by HSC during the culture period. In this study, we demonstrate that CVD synthesis produces different nanomaterials morphologies, which generate differences in the cellular response. Beside, we have shown that CN_x belonging to high region (CN_x-HR) are biocompatible with mammalian cells and they can be uptaken them.

Heterogeneity of nitrogen-doped multiwalled carbon nanotubes produced by chemical vapor deposition and their effect on mammalian cells

1. Introduction

Carbon nanotubes (CNTs) have emerged as an ideal candidate for bioimaging, biosensing, scaffold and biomedical applications, due to their mechanical, electrical and optical properties [1-3]. CNTs are cylindrical hollow graphene sheets of one or more layers (denoted single-wall, SWCNT, or multiwall, MWCNT) with a length ranging between 2 nm to 10 mm and diameters form 0.4-2 nm and 2-200 nm for SWCNT and MWCNT, respectively [4]. The reactivity of CNTs and their shape similar to asbestos fibers represent a risk for human healthy, for this reason, researches regarding to apply CNTs in medicine are extensive [5, 6]. The chemical modification of CNTs by addition of functional groups to the sidewall of CNTs has been widely studied, this with the aim to make them biocompatibles with mammalian cells [7, 8] and whole organisms [9]. Since biocompatibility of CNTs is related to their dimension (lengths and diameters) [5, 10], synthesize method, charge (functional groups) [9, 11], degree of agglomeration (due to their intrinsic properties) [12], concentration and time of exposure [10], cell type [10], biodistribution and biodegradation [13]. All the factors above mentioned make difficult to determine if CNT are biocompatibles or toxic for mammalian cells, due to the different cellular responses that these materials generate to cells, where results sometimes looks inconsistent and even contradictory [10, 14, 15].

Chemical modification of CNTs by doping with nitrogen (CN_x) has shown a positive effect on biocompatibility of cells [7] and whole organisms [9] compared with other types, suggesting that these nanomaterials could have potential biomedical applications. However, similar to functionalized CNTs, alteration in cell behavior by CN_x has been reported, where the cytotoxic effects are due to long size of nanotubes [16], generation of reactive oxygen species (ROS), alterations in cellular cycle and a toxic effect concentration dependent [5].

Chemical vapor deposition (CVD) is one of the most common methods to synthesize CNTs at large scale [17-20]. However, the synthesis of CNTs by CVD produces a variety of morphologies with different diameters and lengths as well as different types of CNT when the carbon precursor or catalyzer changes [21, 22]. In our previous work, we demonstrated that CN_x produced by CVD had cytotoxic effects on NIH-3T3 murine fibroblasts by concentration, time and exposure route dependent. Furthermore, we showed that CVD produces a heterogenic product with different sizes of CN_x, and this nanomaterial's heterogeneity could be the reason behind the controversy regarding to cytotoxicity/biocompatibility of CNTs [23].

Here, we report the synthesis of CN_x by CVD and their effect on two types of mammalian cells, murine fibroblasts and human hematopoietic stem cells (HSC). We found different sizes of CN_x in the same batch, and this difference plays and important role on their compatibility with mammalian cells, where CN_x from the same batch are biocompatible or toxic for mammalian cells. Furthermore, we found that CN_x belonging to high region of production are biocompatible with fibroblasts and HSC.

2. Materials and methods

2.1. Synthesis, purification and characterization of CN_x.

CN_x were synthesized by using the CVD method [24]. The CVD system consists of an aerosol generator and a 100-cm-long quartz tube placed inside of two 60-cm-long horizontal tube furnaces together. Prior to CN_x synthesis, two furnaces were heated to 850°C and temperature keeps constant. The chemical precursors used were 2.5 wt. % ferrocene in benzylamine, and the mix was placed into the piezo-driven aerosol generator. This generated spray (aerosol) was carried by an Argon flow at 2.5 L/min through a heated quartz tube. After 30 min of synthesis, the quartz tube was cooled down at room temperature (RT) and washed with ethanol to remove benzylamine, and acetone to eliminate amorphous carbon and non-add CN_x.

For CN_x recovery, the quartz tube was divided into fractions of 1 cm, and then each fraction was recovered by inner scrap and was collected separately. Three batches of CN_x were synthesized. Samples were weighed to obtain the yield of CN_x synthesis. Three fractions were chosen, loaded into pins and visualized by SEM (Philips-XL 30 SFEG; Dual Beam (FIB/SEM) FEI-Helios Nanolab 600 equipped with an EDX detector) to determine lengths, diameters and EDX spectrum. CN_x fractions were purified by acid treatment of HNO_3:H_2SO_4 (1:3). Samples were sonicated by ultrasonic bath operating at 100 W (Branson 2510 Ultrasonic Cleaner, 42 kHz) with absolute ethanol during 1 h at RT and filtrated using 0.45 µm membrane filters. CN_x were recovered from membranes and put into Erlenmeyer flask where they were sonicated again by an ultrasonic bath with acid treatment for 12 h on ice. Purified CN_x were diluted with distillated water, kept

on repose during 48 h and filtered. Supernatant and sediment were treated as separately samples. Finally, for biological assay, sediment samples were chosen.

2.2 Dispersion of CN_x fractions in culture medium.

CN_x fractions were dispersed separately in basal-IMDM (Iscove`s Modified Dulbecco`s Medium (IMDM) (SIGMA) pH 7.2 supplemented with 10% fetal bovine serum (GIBCO), 100 U/mL penicillin, 100 µg/mL streptomycin and 0.25 µg/mL amphotericin B (SIGMA)) at a final concentration of 1 mg/mL. The samples were sonicated by an ultrasonic bath at 40ºC during 8 h, resulting in a stable dispersion with no visible macro-agglomerates of CNTs. Then, the stocks were storage at 4°C until used.

2.3 Cell culture and isolation of HSC form umbilical cordon blood

NIH-3T3 murine fibroblasts (ATCC) were defrosted and cultured in basal-IMDM into 24-well plates (Corning) over a period of 72 h in a humidity chamber at 37°C and CO_2 5% (Shell-Lab). After three passes, when 80% cellular confluence was reached, cells were harvested with trypsin-EDTA.

Umbilical cordon blood (UCB) samples from full-term deliveries were kindly provided by Dr. Marco Kalixto from the ISSSTE regional hospital, according to their ethical committee´s guidelines. Separation of mononuclear cells (MNC) from UCB was carried using procedure [25]. Briefly, 20-45 mL blood samples with heparin (2,000 UI) were centrifuged at 450 *g* for 15 min, and the 4-6 mL of with interphase cells and plasma were transferred into a 15-mL falcon tube containing the same volume of phosphate-buffered saline (pH 7.2). Samples were mixed gently and

transferred into 15-mL falcon tubes with 7 mL of Ficoll-Paque Plus (Pharmacia) at temperature room and centrifuged for 20 min at 550 *g*. MNC ring was recovered, put into clean tubes and centrifuged at 800 *g* for 15 min. MNC were resuspended in 1 mL of basal-IMDM supplemented with human recombinant cytokines: (Peprotech) 5 ng/mL stem cell factor (SCF), 5 ng/mL flt3 ligand (Flt-3), 5 ng/mL interleukin-3 (IL-3), 12.5 ng/mL interleukin-6 (IL-6), (Probiomed) 10 ng/mL granulocyte-macrophage colony stimulation factor (GM-CSF, Gramal®, molgramostin), 10 ng/mL granulocyte colony stimulation factor (G-CSF, Filatil®, Filgrastim), 3 U/mL erythropoietin (EPO, Bioyetin®).

2.4 Evaluation of biocompatibility of CN_x on NIH-3T3 murine fibroblasts and HSC.

In order to evaluate the effect of the different CN_x fractions, NIH-3T3 fibroblast cells were used. Cell suspensions with density of $2x10^3$ cells per well were added to 96 well plates and incubated during 96 h at 37°C and 5% CO_2. CN_x fractions at final log concentration of 0.07-70 µg/mL were added into cultures and incubated again for 96 h. Samples were taken each 24 h and cell viability was determined by cell counting with the trypan blue exclusion method using a hemocytometer. NIH-3T3 cell cultures without nanomaterial were used as control. To avoid the variation on CN_x concentration in cell cultures when medium is changed, kinetics carried out at work volume of 250 µL without medium replacement.

For HSC experiments, $0.5x10^6$ cells/mL were seeded onto 24 well plates and incubated for cellular recovery process (5 days at 37°C and 5% CO_2). After, medium was changed with fresh basal-IMDM supplemented with cytokines and

cells were counted again. Cells were exposed to each CN_x fractions at final log concentration of 0.07-70 µg/mL during 5 days. Samples were taken each 24 h and cell viability was determined by cell counting with the trypan blue exclusion method using a hemocytometer. Cell cultures without nanomaterial were used as control. To avoid variation on CN_x concentration in cell cultures when medium is changed, kinetics carried out at work volume of 1100 µL without medium replacement.

2.4 Extraction of CN_x uptake by HSC

After cell culture, cells were washed gently three times with PBS. All the adherent cells containing CN_x were incubated with trypsin for 10 min and recovered by pipetting, transferring the whole volume into Eppendorf tubes. Samples were centrifuged at 2,000 rpm for 10 min. Then, the supernatant was discarded and the cells were washed again with PBS twice. Next, the cells were resuspended in PBS and sonicated by ultrasonic bath operating at 100 W during 20 min on ice. After sonication, the samples were centrifuged at 10,000 rpm for 30 min and CN_x were washed with distillated water three times. Finally, CN_x samples were loaded into pins and visualized by SEM.

2.5. Statistics

Data are presented as mean and ± standard deviation. Statistical comparison was performed with the 2-ways ANOVA. Dunnett and Bonferroni post tests were used to compare treatment groups to control. *P*-values < 0.05 were considered significant.

3. Results

3.1. Production, determination of length and diameter of CN_x

After collecting individual fractions of CN_x, these were weighed and potted to obtain pattern of production. Figure 1 shows a plot of CN_x fractions weight. The yield of CN_x was into furnace 1 with 694.5±78.5 mg; meanwhile in the furnace 2 was 94.8±22.7 mg, showing a maximum production of nanomaterials in the first 40 fractions (Figure 1a). The synthesis of CN_x followed a Gaussian behavior. According with the graphic, we classified the fractions based on their yield: 1) low region (LR), that correspond to fractions with a <15 mg/fraction (fractions 6-10 and 34-76); 2) middle region (MR) 15-30 mg/fraction (fractions 11-17 and 25-35) and 3) high region (HR) >30 mg/fraction (fractions 18-24).

It has been reported that synthesis of CNTs by CVD produces different morphologies and diameters of CNTs [21, 23]. Optical (Figure 1b-d) and SEM (Figure 1e-j) images showed heterogeneity in the sample, where different fractions from the same synthesis presented several differences in lengths and diameters. The lengths of CN_x from LR, MR and HR were 33.52 ± 0.92, 236.53 ± 6.62 and 169.20 ± 9.68, respectively, with diameters of 50.04 ± 5.83, 28.05 ± 4.36 and 52.67 ± 9.36.

The CN_x that belong to the same region of synthesis could have the same effect on mammalian cells but different effect compared with CN_x that correspond to another region. For that reason, fractions of CN_x from HR (CN_x-HR) of two different batches, as well as fractions that belong to MR (CN_x-MR) were selected for biological testing. NIH-3T3 murine fibroblasts and HSC were chosen as biological models using different concentration of nanomaterials.

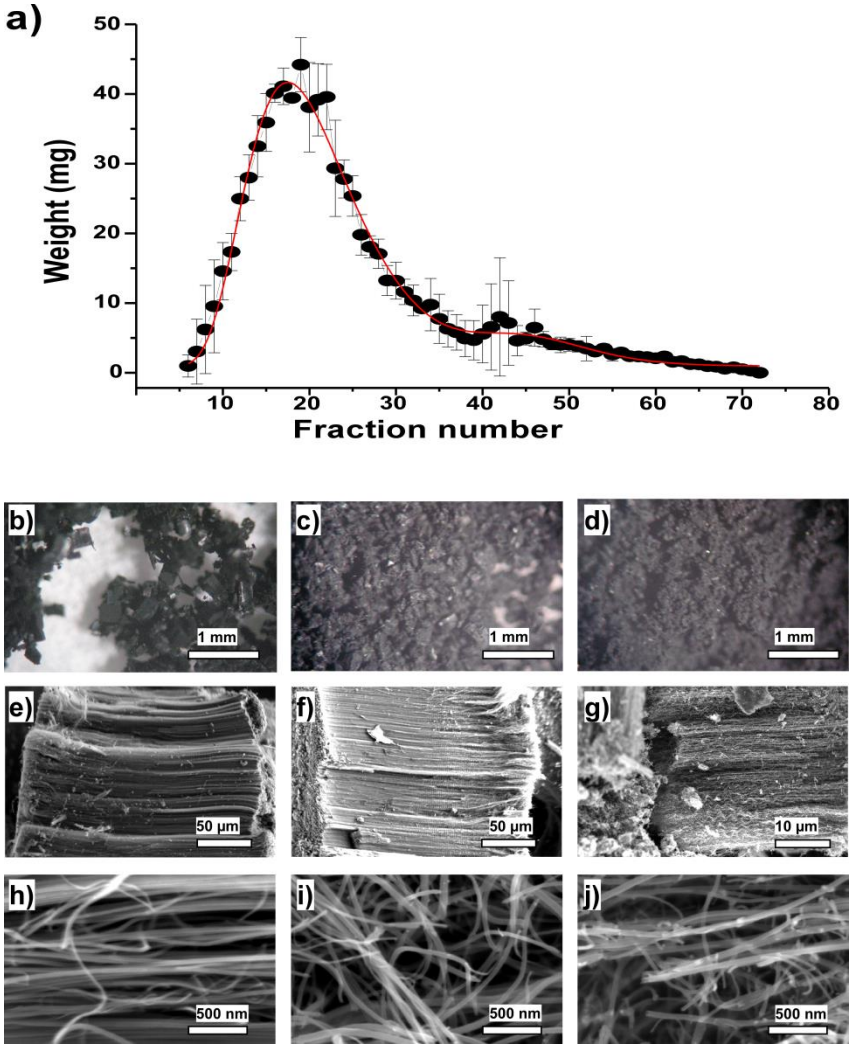

Figure 1. Production and morphology of CN_x. Mean and SD of fractions weight collected from 3 batches. The red line indicates a LogNormal distribution fit (a). Optical (b-d) and SEM (e-j) images of MR (b,e,h), HR (c, f, i) and LR (d, g, j).

Figure 2 shows the fibroblast incubated with CN_x. Regarding to fibroblast growth, no significant effect over proliferation of cells was observed when cells were exposed to CN_x-HR that were recovered from batch I or batch II, (Figure 2 a and b, respectively); meanwhile, CN_x-MR from batch I showed a cytotoxic effect after 24 h of exposure in concentration of 7 and 70 µg/mL, and after 48 h all the concentration affected negatively the proliferation of murine cells (Figure 2c). This

suggests a toxicity concentration and time dependent. Besides, these results showed clearly a different behavior of CN_x from the same batch, where they can have either a biocompatible or toxic effect, depending of the area that they were recovered.

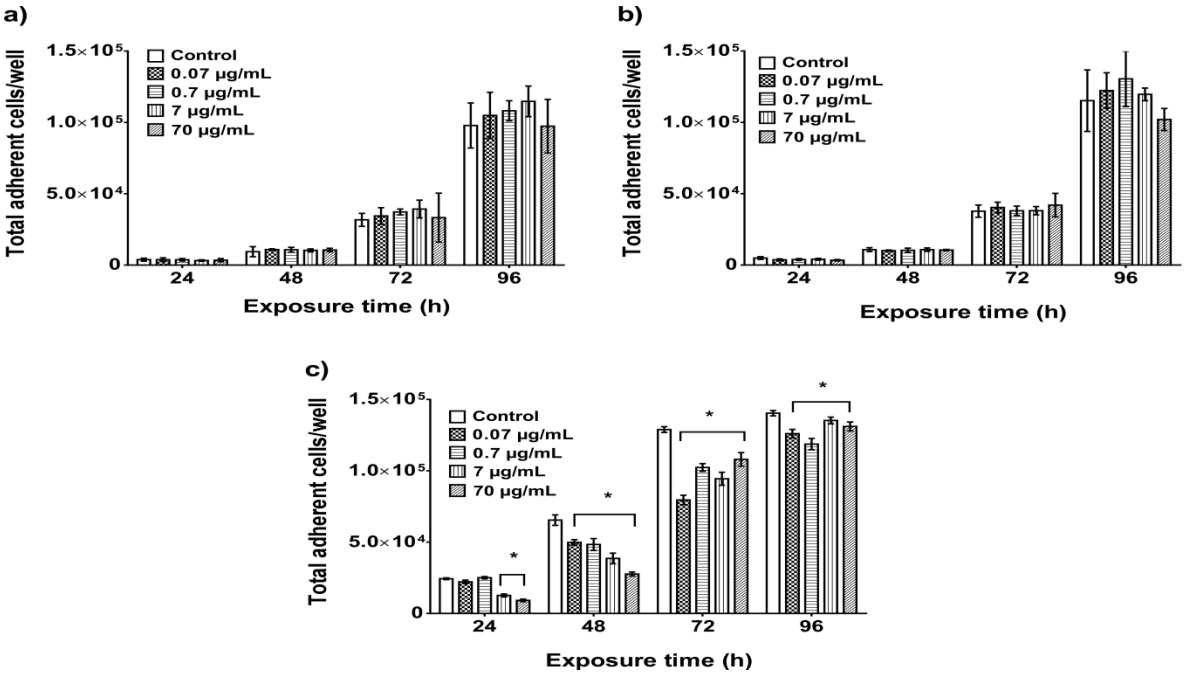

Figure 2. Murine fibroblast cells exposed to different concentration of CN_x during 96 h. a) batch I CN_x-HR; b) batch II CN_x-HR; c) batch I CN_x-MR. Data are presented as mean ± SD. ∗ indicates a significant difference compared to untreated controls ($p < 0.05$); n≥3.

Biocompatibility of nanomaterials is cell type dependent [4, 10]. For that reason and due to the CN_x-HR were biocompatible with fibroblasts, the next step was testing them on HSC. Figure 3 showed the expansion kinetic of HSC incubated with nanomaterials during 5 days. Similar to fibroblasts, either CN_x-HR from batch I (Figure 3 a) or batch II (Figure 3 b) had no negative effect on expansion of HSC. Following the effects of CN_x-HR on HSC, TNF-α level was

determined in control and 70 µg/mL of CN_x-HR samples at the end of the kinetic, where control showed more production of TNF-α than samples with nanomaterials (Figure 3 c). These results suggest that CN_x-HR were biocompatible with HSC.

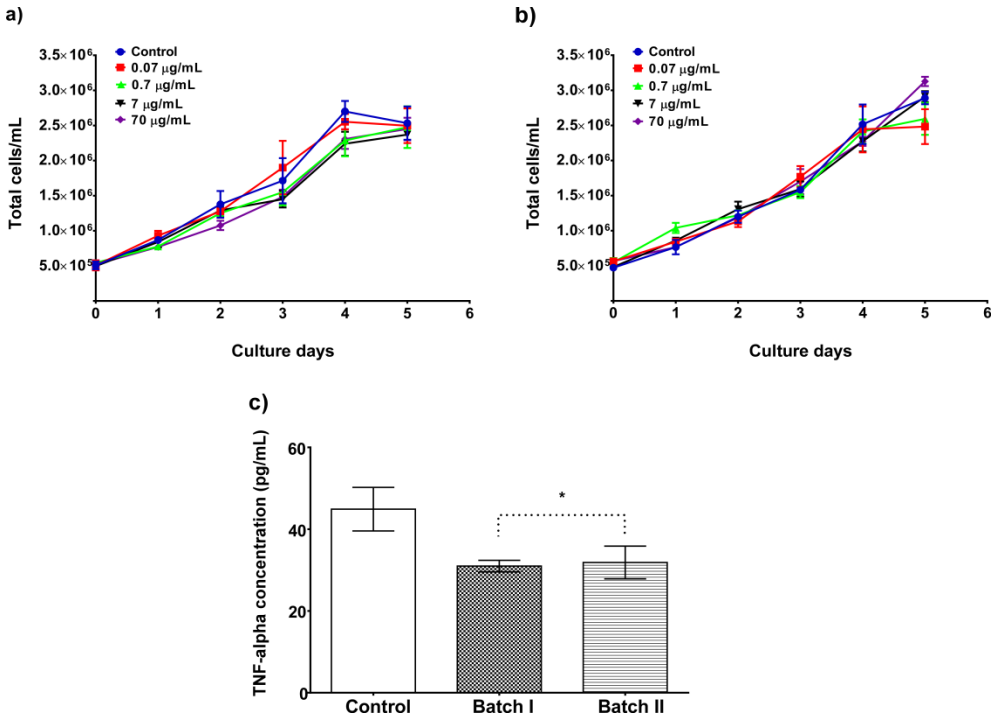

Figure 3. Expansion of HSC. Cells were incubated during 5 days with CN_x-HR from batch I (a) or II (b). Determination of TNF-α level in control samples and cultures containing 70 µg/mL of CN_x-HR (c). Data are presented as mean ± SD. ∗ indicates a significant difference compared to untreated controls ($p < 0.05$); n≥3.

Figure 4 shows the cellular uptake of CN_x-HR. After 5 days of exposure at 70 µg/mL of nanomaterials, apparently some of the cells uptake CN_x (Figure 4 a-b). To confirm if the nanomaterials were inside of the cells, several washes were carried out to eliminate all CN_x-HR in the culture medium or outside of the cells (Figure 4 c-d).

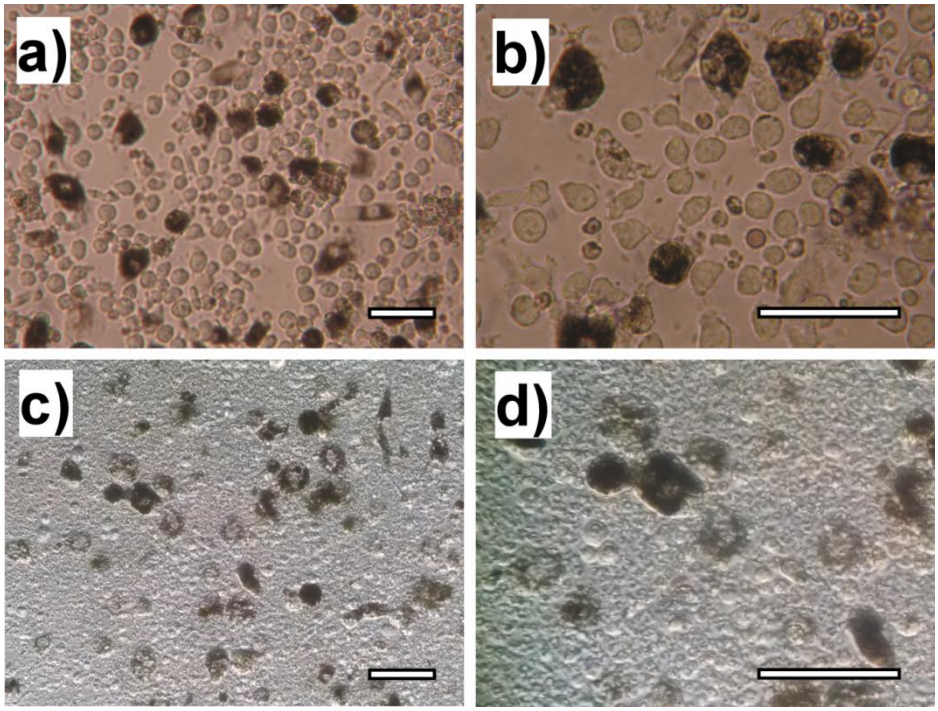

Figure 4. Optical images of HSC after incubation during 5 day with CN_x-HR at 70 µg/mL. The images were taken with (a-b) and without (c-d) culture medium to show the CN_x uptake by cells. Magnification ×20 (a,c) and ×40 (b,d). Scale bar 50 µm.

After washing cells, CN_x-HR were recovered from cells by cell lysis. Figure 5 shows the gallery of CN_x-HR as well as their EDX spectrum. Nanomaterials sonicated in ethanol were found as well-defined and dispersed CN_x-HR (Figure 5 a) with the presence of carbon, oxygen and sulfur elements, corresponding to SO_4^- groups generate by purification process (Figure 5 d). When CN_x-HR were dispersed in basal-IMDM, nanomaterials were dispersed but covered by proteins form FBS, creating a thick layer making difficult to see individual CN_x-HR (Figure 5 b), the EDX analysis exhibited the presence of some of the elements present in the culture medium (Figure 5 e). The CN_x-HR extracted from cells were observed as

individual nanotubes forming agglomerations and with some island of biological material; these agglomerations could be due to interaction with intracellular proteins (Figure 5 c, arrows). The EDX spectra showed the elements present in the sample (Figure 5 f). Due to CN_x-HR dispersed in basal-IMDM and CN_x-HR extracted from cells had different morphology as well as difference in their EDX spectra, it can be inferred that CN_x-HR were embedded by HSC.

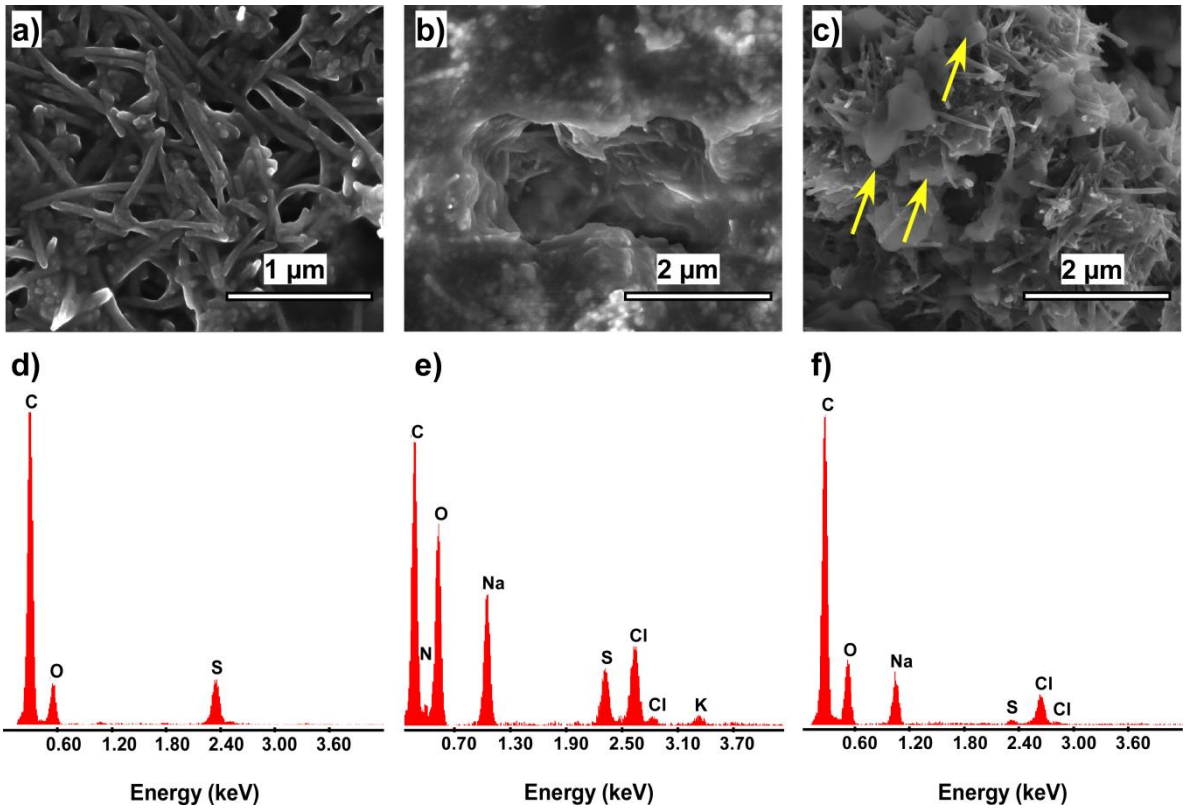

Figure 5. SEM imaging and EDX analysis of CN_x-HR. SEM micrograph of CN_x-HR dispersed in ethanol (a), basal-IMDM (b) and extracted from cells (c) and their respective EDX spectra (d, e, f).

In this study, we demonstrated that CVD synthesis produces different nanomaterials morphologies, which generate differences in the cellular response.

Beside, we have shown that the CN_x belonging to high region (CN_x-HR) are biocompatible with mammalian cells and cells can embed them.

Acknowledgments

We wish to thank The Marcos Moshinsky Foundation and CONACYT-Mexico CB-2013-220744 (EMS) for partial funding. J. Gil Munguía-López thanks to CONACYT for his scholarship 250279.

References

[1] Ferreira L, Karp JM, Nobre L, Langer R. New Opportunities: The Use of Nanotechnologies to Manipulate and Track Stem Cells. Cell Stem Cell. 2008;3:136-46.

[2] De Volder MF, Tawfick SH, Baughman RH, Hart AJ. Carbon nanotubes: present and future commercial applications. Science. 2013;339:535-9.

[3] Mundra RV, Wu X, Sauer J, Dordick JS, Kane RS. Nanotubes in biological applications. Current opinion in biotechnology. 2014;28:25-32.

[4] Cui HF, Vashist SK, Al-Rubeaan K, Luong JH, Sheu FS. Interfacing carbon nanotubes with living mammalian cells and cytotoxicity issues. Chem Res Toxicol. 2010;23:1131-47.

[5] Mihalchik AL, Ding W, Porter DW, McLoughlin C, Schwegler-Berry D, Sisler JD, et al. Effects of nitrogen-doped multi-walled carbon nanotubes compared to pristine multi-walled carbon nanotubes on human small airway epithelial cells. Toxicology. 2015;333:25-36.

[6] Fisher C, E. Rider A, Jun Han Z, Kumar S, Levchenko I, Ostrikov K. Applications and Nanotoxicity of Carbon Nanotubes and Graphene in Biomedicine. Journal of Nanomaterials. 2012;2012:1-19.

[7] Zhao ML, Li DJ, Yuan L, Yue YC, Liu H, Sun X. Differences in cytocompatibility and hemocompatibility between carbon nanotubes and nitrogen-doped carbon nanotubes. Carbon. 2011;49:3125-33.

[8] Li DJ, Niu LF. Influence of N atomic percentages on cell attachment for CNx coatings. Bull Mater Sci. 2003;26:371-5.

[9] Carrero-Sanchez JC, Elias AL, Mancilla R, Arrellin G, Terrones H, Laclette JP, et al. Biocompatibility and toxicological studies of carbon nanotubes doped with nitrogen. Nano Lett. 2006;6:1609-16.

[10] Sohaebuddin SK, Thevenot PT, Baker D, Eaton JW, Tang L. Nanomaterial cytotoxicity is composition, size, and cell type dependent. Particle and Fibre Toxicology. 2010;7:22.

[11] Zhao X, Liu R. Recent progress and perspectives on the toxicity of carbon nanotubes at organism, organ, cell, and biomacromolecule levels. Environment International. 2012;40:244-55.

[12] Sabuncu AC, Kalluri BS, Qian S, Stacey MW, Beskok A. Dispersion state and toxicity of mwCNTs in cell culture medium with different T80 concentrations. Colloids and Surfaces B: Biointerfaces. 2010;78:36-43.

[13] Kunzmann A, Andersson B, Thurnherr T, Krug H, Scheynius A, Fadeel B. Toxicology of engineered nanomaterials: Focus on biocompatibility, biodistribution and biodegradation. Biochimica et Biophysica Acta (BBA) - General Subjects. 2011;1810:361-73.

[14] Lanone S, Andujar P, Kermanizadeh A, Boczkowski J. Determinants of carbon nanotube toxicity. Adv Drug Deliv Rev. 2013;65:2063-9.

[15] LIU Y, ZHAO Y, SUN B, CHEN C. Understanding the Toxicity of Carbon Nanotubes. Acc Chem Res. 2013;46:702-13.

[16] Boncel S, Muller KH, Skepper JN, Walczak KZ, Koziol KK. Tunable chemistry and morphology of multi-wall carbon nanotubes as a route to non-toxic, theranostic systems. Biomaterials. 2011;32:7677-86.

[17] Nxumalo EN, Nyamori VO, Coville NJ. CVD synthesis of nitrogen doped carbon nanotubes using ferrocene/aniline mixtures. Journal of Organometallic Chemistry. 2008;693:2942-8.

[18] Bazargan A, McKay G. A review – Synthesis of carbon nanotubes from plastic wastes. Chemical Engineering Journal. 2012;195-196:377-91.

[19] Mubarak NM, Abdullah EC, Jayakumar NS, Sahu JN. An overview on methods for the production of carbon nanotubes. Journal of Industrial and Engineering Chemistry. 2014;20:1186-97.

[20] Shah KA, Tali BA. Synthesis of carbon nanotubes by catalytic chemical vapour deposition: A review on carbon sources, catalysts and substrates. Materials Science in Semiconductor Processing. 2016;41:67-82.

[21] Meysami SS, Dillon F, Koós AA, Aslam Z, Grobert N. Aerosol-assisted chemical vapour deposition synthesis of multi-wall carbon nanotubes: I. Mapping the reactor. Carbon. 2013;58:151-8.

[22] Meysami SS, Koós AA, Dillon F, Grobert N. Aerosol-assisted chemical vapour deposition synthesis of multi-wall carbon nanotubes: II. An analytical study. Carbon. 2013;58:159-69.

[23] Munguía-Lopez JG, Muñoz-Sandoval E, Ortiz-Medina J, Rodriguez-Macias FJ, De Leon-Rodriguez A. Effects of Nitrogen-Doped Multiwall Carbon Nanotubes on Murine Fibroblasts. Journal of Nanomaterials. 2015;2015:1-7.

[24] Kamalakaran R, Terrones M, Seeger T, Kohler-Redlich P, Ruhle M, Kim YA, et al. Synthesis of thick and crystalline nanotube arrays by spray pyrolysis. Applied Physics Letters. 2000;77:3385-7.

[25] Andrade-Zaldívar H, Kalixto-Sánchez MA, de la Rosa APB, De León-Rodríguez A. Expansion of Human Hematopoietic Cells from Umbilical Cord Blood Using Roller Bottles in CO2 and CO2-Free Atmosphere. Stem Cells and Development. 2011;20:593-8.

5. Chapter IV

Directing the self-assembly of tumor spheroids by bioprinting cellular heterogeneous models with alginate/gelatin hydrogels

Human tumor progression is a dynamic process involving diverse biological and biochemical events such as genetic mutation and selection in addition to physical, chemical, and mechanical events occurring between cells and the tumor microenvironment. Using 3D bioprinting technologies a method to embed tumor cells and tumor associated stromal cells is developed, within a cross-linked alginate/gelatin matrix in a design that initially keeps each cell type isolated and enables migration over time. These 3D hydrogel models allow cells to grow, proliferate and achieve higher viability than conventional 2D cell culture and after 7 days of co-culture, cancer cells begin to form multicellular tumor spheroids (MCTS) which increase in size over time. Also, the IMR-90 stromal fibroblast cells can migrate through a non-cellularized region of the hydrogel matrix and infiltrate the MDA-MB-231 spheroids after ~ 15days creating mixed MDA-MB-231/IMR-90 MCTS. This study provides insights into reconstructing biomimetic *in vitro* tissue co-culture models to study cell-cell and cell-matrix interactions, and tumorigenesis mechanisms.

Directing the self-assembly of tumor spheroids by bioprinting cellular heterogeneous models with alginate/gelatin hydrogels

Tao Jiang, Jose G. Munguia-Lopez, Joel Grant, Sanahan Vijayakumar, Antonio De Leon-Rodriguez, Joseph M. Kinsella

Submitted to: Advanced Materials, October 2016

1. Introduction

Breast cancer patients with endocrine receptor-positive (ER-positive) or human epidermal growth factor receptor-2-positive (HER2-positive) tumors are eligible for treatment with therapies targeted against these markers. However, patients with tumors that do not express ER, progesterone receptor (PR) or HER2 markers represent about 15% of patients and form the triple negative (TN) subclass, associated with poor survival and increased recurrence [1]. We now understand that tumors are heterogeneous and that the tumor microenvironment plays key roles in tumor evolution and resistance to therapy [2]. Solid tumor growth *in vivo* occurs in a three-dimensional (3D) environment with cells in constant, and close, contact among the extracellular matrix (ECM) and stromal cells such as fibroblasts and macrophages, soluble growth factors, gases, nutrients, and other physical and chemical stresses [3]. Cancer associated fibroblasts (CAFs) are known to have key signaling roles in tumor progression and metastasis [4].

To accurately determine CAFs influence traditional cell culture techniques are challenging to use, as it is difficult to precisely control the localization of the different stromal cells and tumor epithelial cells. 3D cell culture and co-culture of cancer cells and cancer associated cells grown in polymeric matrices have been shown to more accurately represent the physiological environment of tumors due to the cell-cell and cell-matrix interactions that can occur [5]. A variety of fabrication methods including photolithography, soft lithography, microstamping, and bioprinting have been developed to create 3D culture models [6, 7]. Bioprinting is advantageous to the alternative fabrication methods in that more complex geometric matrices can be printed with high cell density and viability [7, 8]. Cell-laden samples can be created directly with precise reproducibility from cell-hydrogel suspensions [9-11]. Recently, ejection bioprinted ovarian cancer co-culture models using fibroblasts demonstrated that the ovarian cells were able to proliferate and spontaneously form multicellular acini [12].

Here we report the ability of an extrusion bioprintable composite hydrogel consisting of ionic cross-linked alginate and gelatin drives the formation of multicellular tumor spheroids (MCTS) without the use of chemical or physical stresses. The material is mechanically tunable and can be rapidly crosslinked upon extrusion to form a stiff shell while maintaining a fluid-like core allowing cell migration in 3D. Multi-cartridge extrusion bioprinting allows us develop cellular heterogeneous samples comprised of TN breast cancer cells and fibroblasts in specific initial locations with controlled density. We characterized the tumor progression by quantifying the sizes of MCTS along a 30-day culture.

2. Materials and methods

2.1 Material preparation

We prepare a solution of 3% sodium alginate (Protanal LF 10/60 FT) and 7% gelatin (Sigma) in DPBS (Gibco) stirring for 1 h at 60 °C and 2 h at RT. We transferred the mix to clean tubes and then centrifuged at 2,000 rpm for 5 min to eliminate bubbles. After, we storage the hydrogel at 4 °C until we used it. We sterilized the alginate and gelatin powders by UV-light overnight previous to mix. We crosslinked both bioprinted and disk hydrogels by soaking them in 100 mM $CaCl_2$ for 30 s and then rinsed with PBS before culture.

2.2 Mechanical tests

Mechanical properties were characterized by rheometry. We took the data by an oscillation rheometer MCR 302 (Anton Paar, US,). We fabricated a disk by 3D printing to slice the material column into thin disks with dimension Φ25mm × 1mm prior to each test. A cylinder flat geometry with diameter 25mm (PP25) was mounted to the rheometer. All the experiments were triplicated.

Amplitude sweep was first implemented to find the linear viscoelastic range. A strain sweep from 0.01% to 100% was applied to the gel at frequency of 0.01 Hz and 10 Hz. Results declared that the gel started to loss linearity beyond 10% strain. For safety considerations, we chose 1% strain for all the tests.

To analyze the gelation kinetics of the alginate/gelatin matrix we implemented a rheological time sweep where the hydrogel was taken from a 32°C water bath and placed directly onto the rheometer platform that was heated to 25°C. A 1 Hz frequency 0.1% strain was applied based on data derived from an

amplitude sweep. A simulation of the extrusion process using an isothermal time sweep with two intersections where external shear was applied to simulate both the mixing and printing process.

After printing, the hydrogel was cross-linked using 100mM $CaCl_2$ resulting in the formation of a viscoelastic shell on the surface of printed substrate. A frequency sweep was carried out by ramping the frequency logarithm from 0.01 Hz to 100 Hz. 0.1% strain was used based on the results of a previous amplitude ramp.

2.3 Physico-chemical characterization

To confirm the presence of alginate and gelatin in our hydrogel, we carried out physico-chemical experiments. For FT-IR experiments, we freeze-dried the hydrogel and we used the powder to get their infrared spectra using a FTIR-ATR spectrophotometer (Nicolet 6700/Smart iTR, Thermo Scientific) and the results were plotted in a wavelength range from 4000 to 500 cm^{-1}. We confirmed the chemical structure of alginate and gelatin by ^{13}C-NMR. We dissolved lyophilized hydrogel into D_2O at a concentration of 50 mg/mL, then, NMR experiments were performance in a Bruker Avance 600 spectrometer (NMR 600MHz, Avance III HD, Bruker) at 40 °C, with 20,000 scans number (17 h acquisition). The delay adopted was 2s.

2.4 SEM imaging

In order to study the internal structure of the hydrogels, we performance scanning electron microscopy (SEM, Hitachi SU-3500 Variable Pressure). We

crosslinked the hydrogels, rinse with PBS and incubated for 1 h at 37 °C; then, rinsed with water and immediately frozen in liquid nitrogen. Finally, we freeze-dried the samples overnight. For hydrogels containing cells, first we fixed the cells with 4% paraformaldehyde during 30 min at 37 °C, then, rinse, frozen and freeze-dried procedures were carried out. We analyzed the samples under SEM at 25.0 kV and 70 Pa.

2.5 Cell preparation

For biological experiments, we cultured MDA-MB-231 and IMR-90 cell lines transfected with GFP (nuclear expression) and mCherry (cytoplasmatic expression), respectively, in DMEM medium (Gibco) at pH 7.2 supplemented with 10% fetal bovine serum (Wisent Bioproducts), 100U/mL penicillin, 100 μg/mL streptomycin, and 0.25 μg/mL, amphotericin B (Sigma), using 75-T-flask (Corning) in a humidity chamber at 37 °C and CO_2 5% (Panasonic Healthcare Company). After three passes, when 80% of cellular confluence was reached, we washed cells twice gently with DPBS and then harvested by incubation with trypsin-EDTA (0.25%-1X, Gibco) for 10 min.

2.6 Scaffold design and 3D fabrication

In physiological situations, the breast cancer cells were found surrounded by numerous of other types of normal cells. In this study, we focused on the interactions of breast cancer and CAF cells, hence we designed a propeller-like model where breast cancer cells (MDA-MB-231) were placed in the center of the

model, and CAF cells (IMR-90) at the edges. A non-cell zone was also designed between both types of cells to better visualization of the potential migration or invasion of different types of cells. We used SolidWorks software (Dassault Systems, U.S.) to develop the CAD model and converted to STL file and subsequently imported into Sli3r (open source software) to generate standard G-Code. A MATLAB script was written to convert the standard G-code to the specific G-code used by our 3D printer. The propeller model has an internal circle with diameter 7.7mm, and external parts were comprised of two sectors with maximum radius of 8.65mm. The other parameters were calculated to ensure the areas of both cell-laden regions were identical. Each of the propeller models comprised of 4 interlaced layers with layer thickness of 150 μm. The adjacent hydrogel lines had a gap of approximately 500 μm to allow massive exchange of nutrients and gas.

We used a 3D bioprinter BioScaffolder 3.1 (GeSiM, Germany) to print the scaffold in 3D. The printer features a three axes platform with XY resolution of 2 μm and Z resolution of 10 μm. Three extrusion cartridges were installed onto the printing head and driven by pneumatic system. The controlled pressure pushes the piston in the cartridge and thus extrudes the material through dispensing nozzle onto the platform.

Prior to printing, the 3% alginate plus 7% gelatin hydrogels were transferred to a 32 ºC water bath for 1 hour to reach thermal equilibrium. Upon printing, the hydrogels were firstly divided into three cartridges for breast cancer cells, fibroblast cells and non-cells respectively. This action was performed at the first 10 minutes after taking out of water bath to ensure mixing cells into a liquid form that allowed homogeneous distribution. The three cell laden/non-cell cartridges were kept at

room temperature (25 ºC) for 50 minutes that allowed it to reach optimal printing condition. When the printing started, the cell laden hydrogels experienced an increased shear rate during the extrusion and consequently decreased its viscosity, when formed on the platform; the viscosity grew back and held the structure. The printing head traveled along the preprogrammed trajectory and fabricate the scaffold layer by layer. After printing all replicates of the propeller models, excessive 100 mM $CaCl_2$ solution was added to the models for 1 min before rinsed by DPBS, which rapidly crosslinked the surface of the propeller models while remaining the interior uncross-linked viscoelastic gels. The cell laden propeller models were cultured in 6 well plates in an incubator at 37 ºC and 5% CO_2.

2.7 Viability and spheroid formation experiments

To determinate the best cells concentration for long-term experiments, we mixed MDA-MB-231 at initial concentration of 1, 2, 4 and $10x10^6$ cells per mL. First, we created 100 µL disk crosslinked with $CaCl_2$, and incubated for 30 days taking samples at 0, 7, 15, 21 and 30 days after culture. We replaced medium each 3 days. On the other hand, we analyzed the spheroid size and shape over time using a confocal disk inverted microscope (Olympus IX83, Olympus Life Science). We took multi-position and z-stack confocal image, then we used maximum stack arithmetic to create 2D image for counting spheroids and build the full disk or propeller image. We used MTS assay for viability test following the manufacture's procedure (Promega). As a secondary viability test, we used Live/Dead assay kit

(Molecular Probes, ThermoFisher Scientific) for 21-days culture experiments on MDA-MB-231 unlabeled.

3. Results and discussion

Using extrusion based bioprinting we have created a cellular heterogeneous tumor-mimicking *in vitro* model that enables long-term cell co-culture studies as well as the ability to create MCTS with minimal external chemical or physical stresses. These models were prepared incorporating both IMR-90 fibroblast cells (CAFs, cytoplasmic mCherry labeled) and MDA-MB-231 (nuclear GFP-labeled) breast cancer cells suspended in a cell-laden hydrogel. The cells were mixed individually into a composite hydrogel composed of 3% alginate/7% gelatin. The cell-laden hydrogel is then extruded to create a propeller-like design consisting of a central hub of MDA-MB-231 cells adjacent to a hydrogel region of predefined dimensions that does not contain cells flanked by an outer segment of IMR-90 containing hydrogel. The samples are printed onto an agarose coated well plate to inhibit cell adhesion or migration out of the hydrogel during long culture periods (Figure 1).

Extrusion bioprinting requires viscoelastic hydrogels that exhibit an optimized viscosity and stiffness to ensure the smooth extrusion as well as the model fidelity [9]. To characterize the optimized printing window, we implemented a rheological time sweep. The alginate/gelatin hydrogel was taken from a 32°C water bath based on results of temperature sweep.

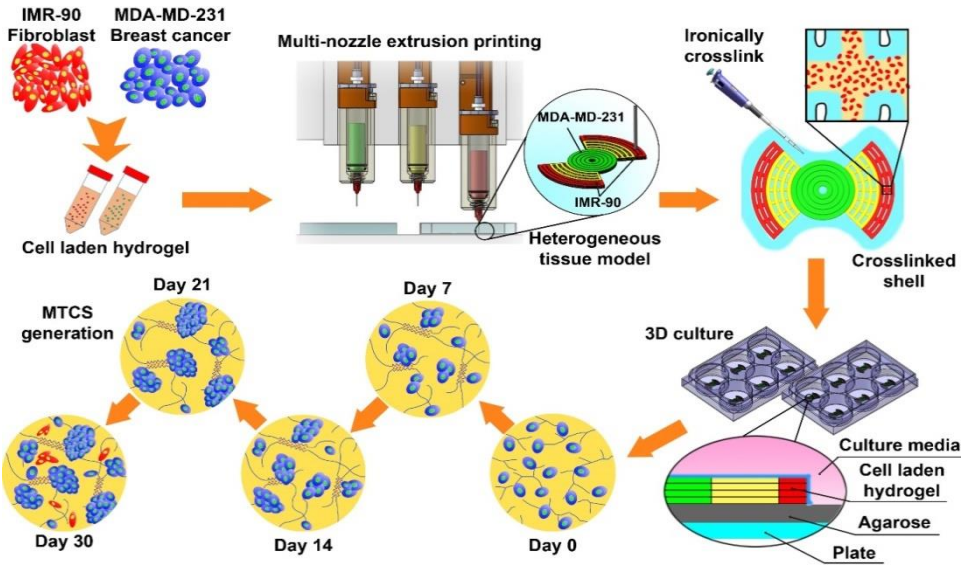

Figure 1. Schematic graph depicting the design and experimental protocol used to create a heterogeneous tumor model comprised of a triple negative breast cancer cell type and cancer associated fibroblasts.

Using a temperature ramp from 25°C to 37°C at a rate of 0.2°C/min to allow thermal stabilization under the geometry we found a decreasing storage modulus (G') from 468.5±34.2 Pa to 3.2±0.2 Pa, and loss modulus (G'') initially 140.7±9.3 Pa at 37°C decreasing to 11.8±0.6 Pa at 25°C (Figure 2a). This reduction in G' and G'' values correspond to a denaturing of the secondary structure of the gelatin fibers resulting in a more liquid-like behavior of the material. The hydrogels transition point occurs at 30.6°C, where G'=G''=51.7±9.7 Pa enabling cell-laden hydrogels to be mixed at 32°C. The sample was placed onto the rheometer platform that was kept 25°C. Periodic oscillation was applied based on data derived from an amplitude sweep. The initially high loss factor shows a rapid decrease occurring within the first 30 min while an increase in the complex viscosity occurs (Figure 3).

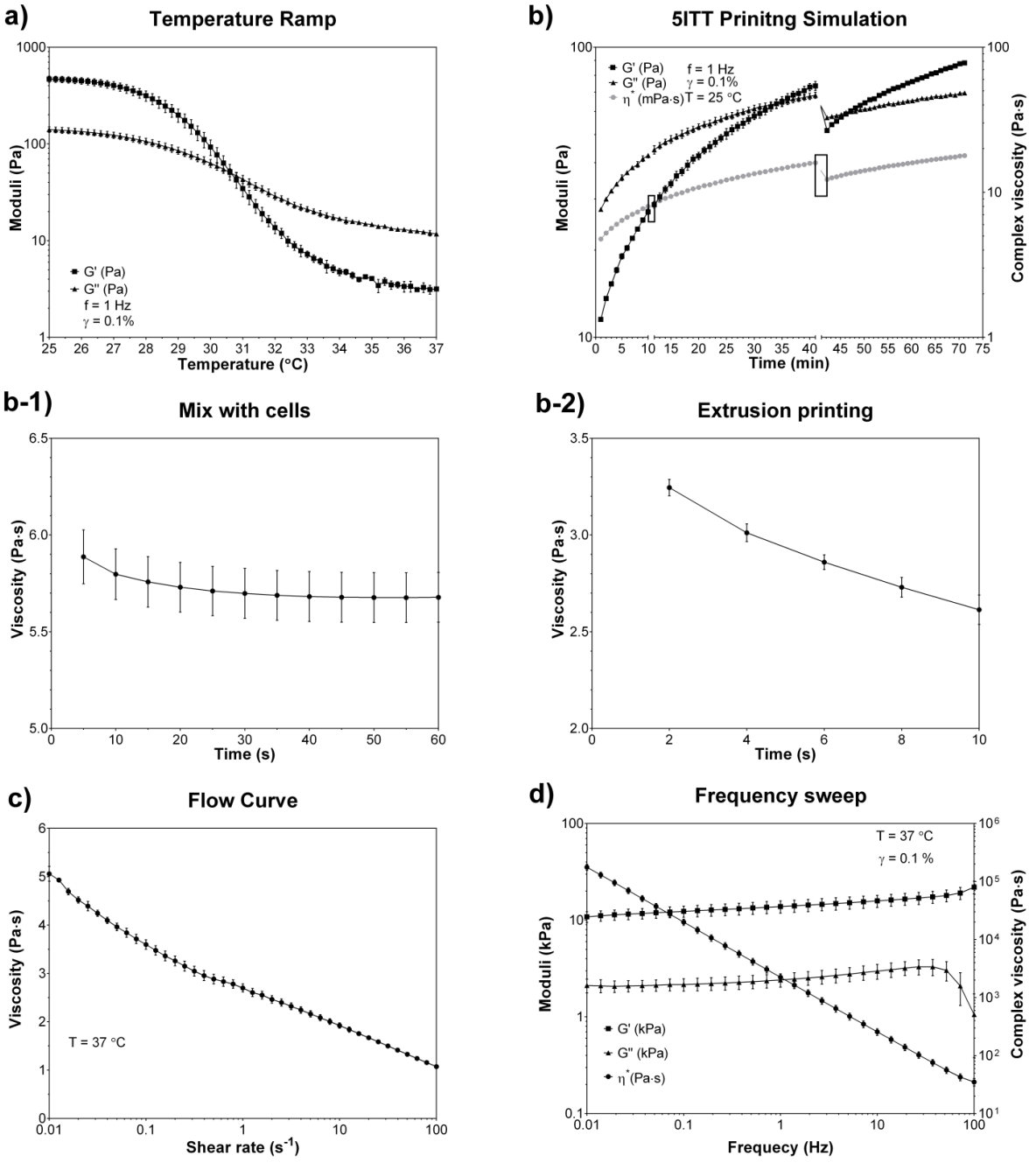

Figure 2. Mechanical properties of hydrogel (3% alginate 7% gelatin blend).a) Temperature ramp of the blend, a transition temperature of 30.6 ºC can be realized. b) 5 Interval Thixotropy Test (5ITT) was implemented to simulate the printing process, a decrease of mechanical integrity during the shearing process was observed but the material recovered rapidly. b-1) Zoom in view of the left box

in Figure 2-b), complex viscosity slightly decreased during the simulated cell mixing procedure. b-2) Zoom in view of the right box in Figure 2-b), a notable decline of viscosity was seen during the simulated extrusion process. c) Flow curve of the uncrosslinked interior hydrogel, a shear thinning properties could be realized. d) Frequency sweep of the crosslinked exterior shell, a 10 kPa of storage shear modulus was obtained that provided essential integrity of the tissue model for a long period of 3D culture (> 30 days).

The sol-gel transition happened at approximately 30 min followed by a continuous rise in viscosity until the material reaches a period of optimal printing characteristics that occurs between 50 min to 90 min. A printing simulation test was performed by shearing the hydrogel in the optimal printing window. The hydrogel showed rapid recovery of integrity after being sheared which guaranteed the stability of the printed model.

We found an increase of both storage and loss modulii from 11.5±0.2 Pa and 27.6±0.2 Pa (Figure 2b). At 10min a shear rate of 15 s^{-1} was applied for 1 min to simulate the mixing process, results show the gentle mixing does not affect gelling kinetics aside from a minor dynamic viscosity decrease from 5887.4±139.4 mPa·s to 5677.8±128.2 mPa·s (Figure 2b). The storage modulus curve intersected that of loss modulus at approximately 24 min after mixing with cells indicating the material gelation. A 100 s^{-1} shear rate was performed at 41 min causing a markable drop in both storage and loss modulus from 73.5±2.7 Pa and 68.3±1.7 Pa to 51.6±0.4 Pa and 57.2±1.0 Pa respectively while the dynamic viscosity decreased from 3245.2±42.1 mPa·s to 2613.9±75.9 mPa·s (Figure 2b). Regardless of the stiff shell which could hold the geometry, the internal hydrogel

went back to a more viscous liquid form when incubated at 37°C allowing the initial cell growth within the 3D viscous microenvironment (Figure 2c). Post-printing the moduli continuously increases reaching 88.3±0.4 Pa and 69.5±1.00 Pa for storage and loss modulus before the post-crosslinking process occurs. At low shear rate regimes the material exhibits a viscosity of 5.1±0.2 Pa·s that decreases as the shear rate is increased, reaching 1.1 Pa·s at 100 s^{-1} (Figure 2c). The inverse relationship indicates the material is shear thinning.

Immediately after printing, the hydrogel was rapidly cross-linked using 100mM $CaCl_2$ for 1 min before washed away resulting in the formation of a viscoelastic shell on the surface of printed substrate which exhibited a frequency dependent shear modulus ranging from 10.9 kPa at 0.01 Hz to 22.0 kPa at 100 Hz (Figure 2d). Both the loss and storage modulus increased with the storage modulus significantly lower than the which increased from 2.1±0.3 kPa at 0.01 Hz to 3.3±0.6 kPa at approximately 26 Hz before undergoing a sharp decrease in the high frequency regime that results in a 1.1±0.7 kPa at 100 Hz. (Figure 2d) In the frequency sweep both moduli increased, the complex viscosity decreased with frequency, indicating shear thinning properties of the shell as found for the core.

The crosslinking process creates a stiff shell which holds the geometry, while the internal hydrogel goes back to a more viscous liquid form when incubated at 37°C allowing cell growth within the 3D viscous microenvironment. The Ca^{2+} will presumably slowly diffuse into the core during the culture and finally form a uniformly viscoelastic model.

The gelation kinetics guide the time periods for each process (Figure 3). We mixed the cells in the hydrogel matrix during the first 10 min and extrude under the

optimal conditions using a 200 kPa pressure at a 5 mm/s print speed using a syringe extruding through a G25 gauge cylindrical nozzle. Notably, the hydrogel was printable during 30 min to 50 min with a lower pressure (< 50 kPa) yet it was too weak to maintain structural integrity. 90 min after preparing the cell-laden hydrogels high pressure (> 240 kPa) has to be applied to extrude the material which may cause cell membrane damage due to high shear stress [11].

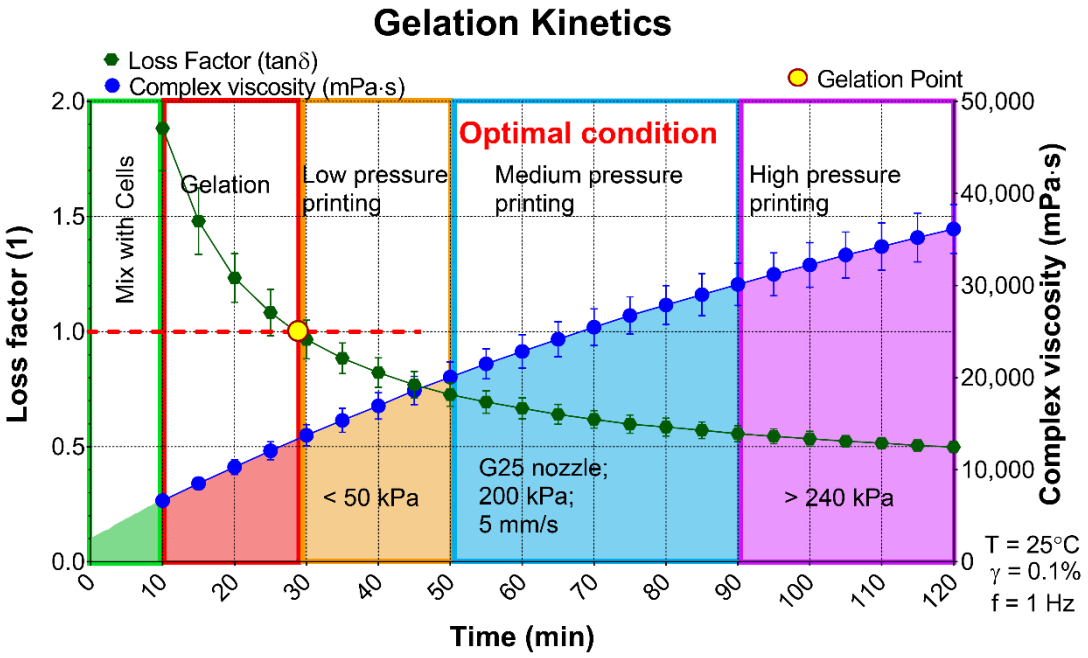

Figure 3. Gelation kinetics of the 3% alginate/7% gelatin hydrogel composite. The green spheres and fit represents the loss factor (left y-axis), the blue spheres and fit represent the complex viscosity (right y-axis). The red dashed line shows where the loss factor equals one indicating the gelation point of the hydrogel. Results showed in mean±SD, n = 3.

Following mechanical characterization of the hydrogel, physico-chemical analysis including FT-IR, ^{13}C-NMR and SEM was performed (Figure 4). FT-IR analysis of the alginate/gelatin hydrogel (Figure 4a, Table 1) reveals typical

saccharide and carboxylate bands for alginate (Figure 4a aII, Table 1) [13] as well as amide I and III bands of gelatin (Figure 4a, Table 1) [14]. ^{13}C-NMR confirms the presence of gelatin (10-60 ppm) [15] as well as alginate (65-110 ppm) (Figure 4b, Table 1) [16]. Qualitative morphological analysis via SEM shows significant porosity throughout the material typically on the micron scale which can led to enhanced cell growth due to an increased surface area and greater exchange rates of essential nutrients and gases (Figure 4c-d).

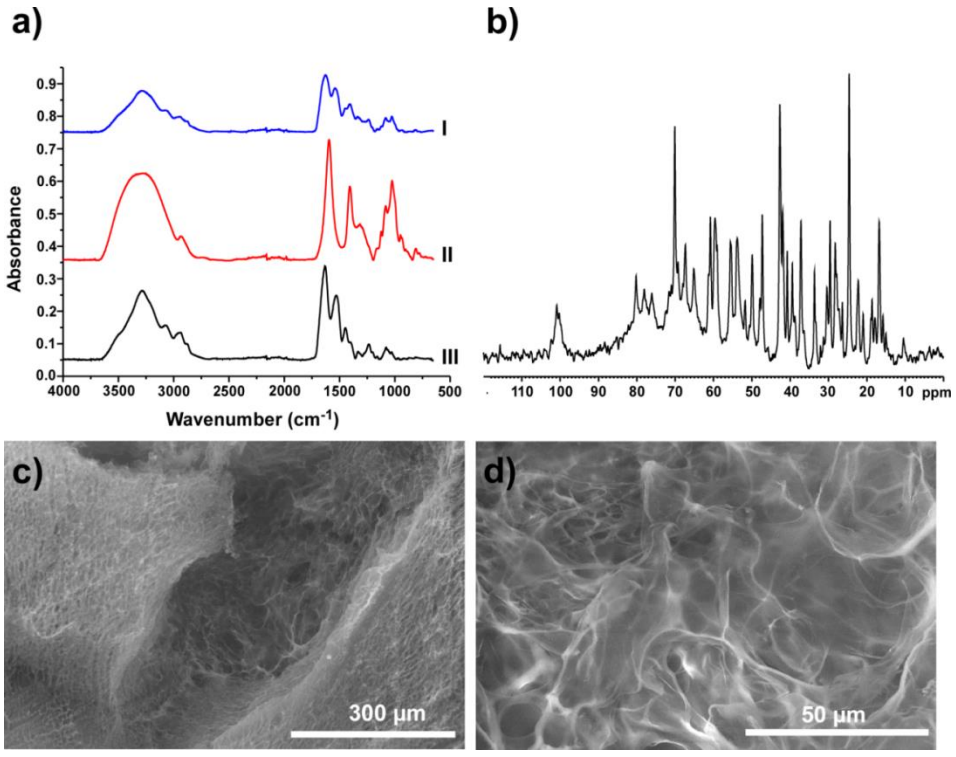

Figure 4. Physical characterization of hydrogel. FT-IR spectrum of alginate/gelatin hydrogel (a I), alginate (a II) and gelatin (a III). ^{13}C-NMR spectra of alginate/gelatin matrix (b). SEM images of hydrogel at ×150 (c) and ×1000 (d) of magnification.

For the material to be capable of creating the bioprinted *in vitro* models containing two, or more, different cell types we must meet the following two critical parameters: 1) the gel has to be capable of handling when in a liquid form in order

Table 1. Characteristics peaks of alginate and gelatin biopolymers.

FTIR (wavenumber cm^{-1})			^{13}C-NMR (ppm)
Alginate	Gelatin	Alginate/Gelatin	Alginate/Gelatin
810.38	1080.81	1027.27	14.9555
947.60	1236.95	1081.99	16.6308
1024.44	1335.04	1160.49	24.5067
1082.13	1398.68	1236.41	26.3145
1123.57	1446.85	1336.33	27.7752
1317.06	1528.48	1405.28	29.5122
1406.05	1628.95	1540.40	33.5927
1594.06	1980.30	1625.10	37.0816
1980.26	2115.17	1979.96	39.3818
2161.96	2162.20	2050.18	40.6988
2931.40	2938.55	2113.17	41.8591
3253.82	3072.86	2163.13	42.5785
	3283.01	2323.40	47.1832
		2941.73	47.1832
		3276.43	55.3134
			58.9993
			60.7464
			67.2631
			70.0376

to obtain a homogeneous dispersion of cells; 2) the gelation temperature and gelation kinetics allow rapid gelation to minimize the exposure of the cells to room temperature conditions. To create the cell-laden hydrogel suspensions we first incubate the hydrogel at 32°C before mixing with the chosen cell line and then temporarily lower the temperature to induce gelation.

3D *in vitro* culture systems have been widely used to produce MCTS models with a number of different cancer cells [3, 17]. The typical doubling time of cells within 3D cultures is approximately 6 days [18], thus to optimize our long-term experiments we cultured the MDA-MB-231-GFP cells within the hydrogels at different initial concentrations over 30 days to determine the optimal cell concentrations within the gel. Since MCTS display different morphologies and not necessarily a perfect spherical shape [17, 19], we used the surface area as a measure of MCTS size and classify the MCTS sizes into three distinct categories: small MCTS (500-10,000 μm^2), medium MCTS (10,000-20,000 μm^2) and large MCTS (>20,000 μm^2).

Using an initial concentration of 1×10^6 MDA-MB-231 cells/mL of gel we were able to induce small MCTS development after 7 days in culture. The quantities and sizes of the MCTS increase over time reaching large MCTS sizes (>20,000 μm^2) at ~21 days (Figure 5 a-d, q). Increasing the initial MDA-MB-231 cell concentration to 2×10^6 cell/mL we observe large MCTS at both 15 and 30 days (Figure 5 e-h, r), without any large or medium MCTS occurring at 21 days, suggesting a dissociation of the medium and large MCTS from the gel or migration out of the hydrogel into the surrounding media [20]. Increasing the MDA-MB-231 concentration to 4×10^6 and 10×10^6 results principally in small MCTS suggesting that the concentration of cells inhibits the formation of the larger MCTS sizes (Figure 5 i-l, s for 4×10^6 and

Figure 5 m-p, t for 10×10^6 cells/mL). The potential dissociation and inhibition of larger MCTS sizes when high initial cell concentrations are employed may be due to inhibition of the integrin β1subunit [20, 21].

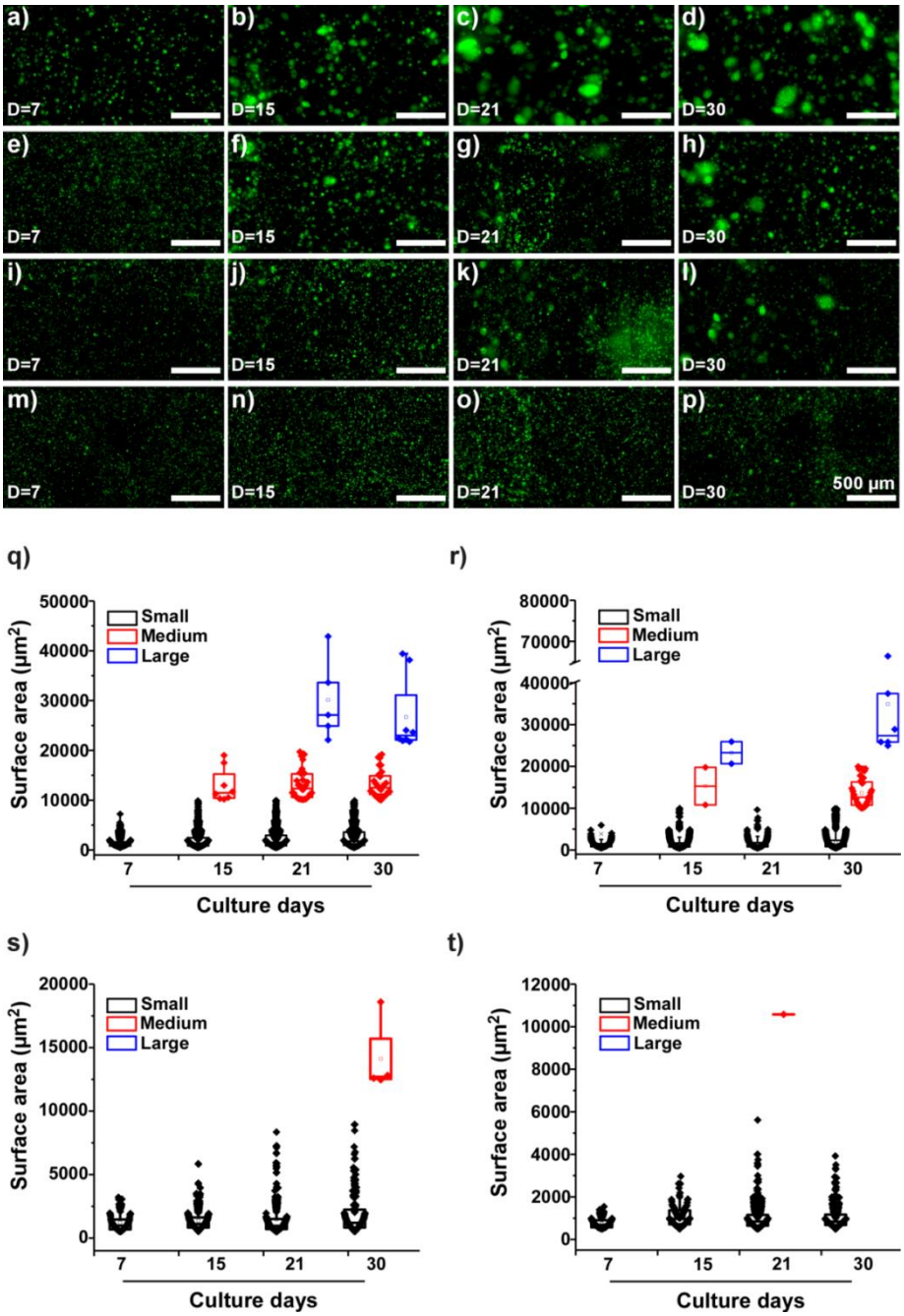

Figure 5. MDA-231 spheroid-like formation. Confocal image of breast cancer cells mixed with hydrogel at initial concentration of $1x10^6$ (a-d), $2x10^6$ (e-h), $4x10^6$ (i-l)

and $10x10^6$ (m-p) cell per mL incubated during 30 days. Scale bar 500 µm, magnification ×10. The frequency of spheroids and their sizes where plotted in box-plot graph for $1x10^6$ (q), $2x10^6$ (r), $4x10^6$ (s), $10x10^6$ (t) cell per mL, where the threshold was 500-10,000, 10,000-20,000 and >20,000 μm^2 for small, medium and large spheroids, respectively.

From the MCTS development experiments employing the MDA-MB-231-GFP laden gels we proceeded to print the heterogeneous cell-laden *in vitro* models using an initial cell concentration of 1×10^6 (Figure 6a). After 7 days of culture the MDA-MB-231 cells again formed small MCTS (Figure 6 c, h) with a similar trend of increasing MCTS size over time (Figure 6 d-f, i-k). At day 15 medium and large MCTS (Figure 6 l) were observed with increasing frequency while small MCTS numbers decreased suggesting a proliferation of individual cells proliferating within the hydrogel (Figure 6 m).

After 30 days the largest MCTS achieved a surface area of ~80,000 μm^2 under these conditions. The IMR-90 began to migrate through the non-cell hydrogel region and infiltrate the MDA-MB-231 containing region after ~ 15days and continue through the remaining culture period creating mixed MDA-MB-231/IMR-90 MCTS.

An increase of MCTS size is one index of cell proliferation within the bioprinted model we compared with metabolic activity to evaluate cell health, proliferation, and MCTS generation when printed within the gel. The metabolic activity of IMR-90 cells remains constant over time (Figure 7a) while the metabolic activity of the MDA-MB-231-GFP cells increased during the first 15 days then decreased at day 21 and increases again at day 30. This is likely due to the

metabolic activity that occurs in the medium and large MCTS compared to the small MCTS and single cells proliferating within the matrix [22].

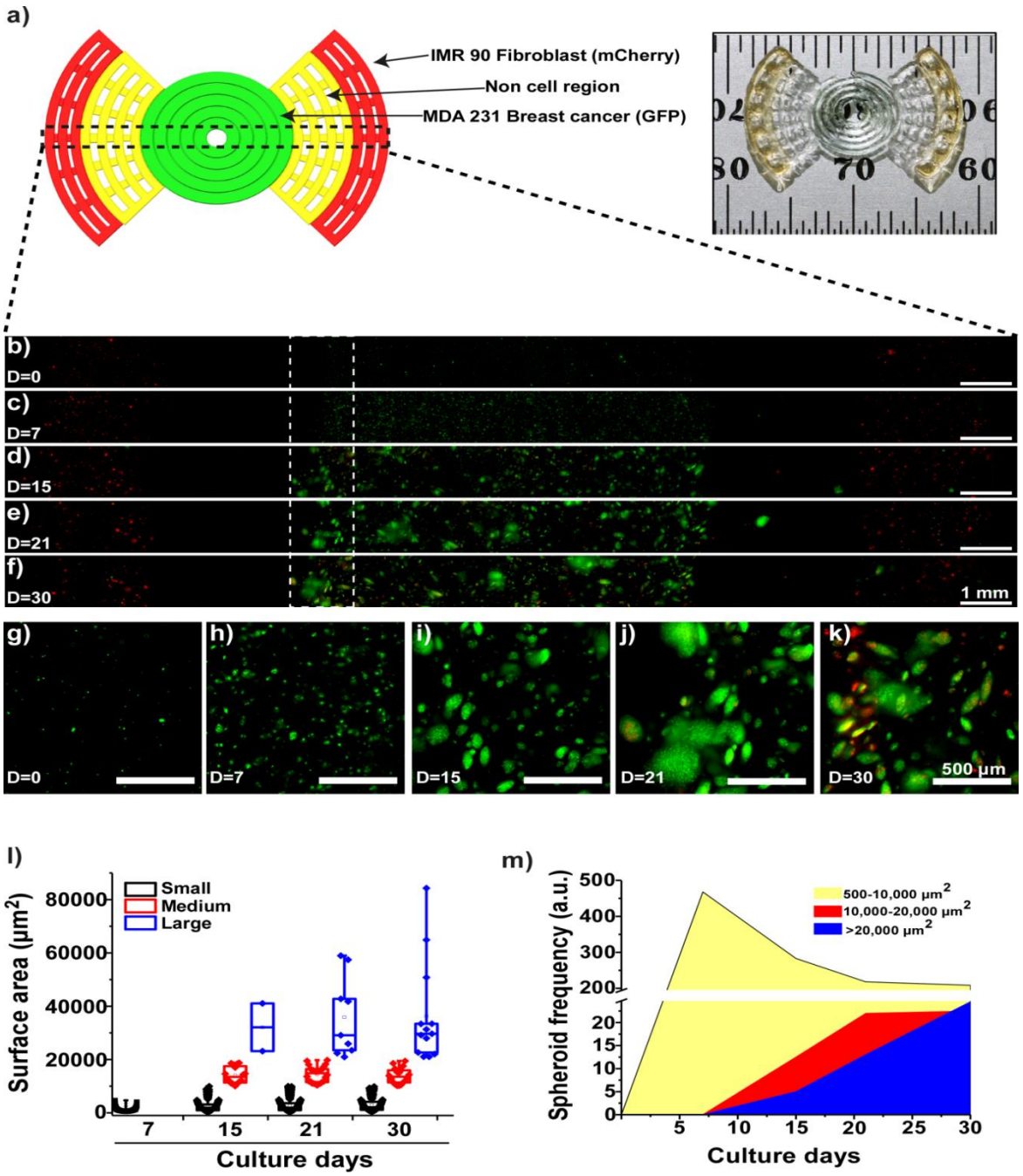

Figure 6. MCTS formation within a 3D bioprinted *in vitro* model consisting of IMR-90 CAFs and MDA-MB-231 triple-negative breast cancer cells. (a) CAD model and photograph of the bioprinted *in vitro* sample . (b) Confocal time-lapse image of

MDA-MB-231-GFP (green) and IMR-90-mCherry (red) cells bioprinted within the model (b-f) and their zoom-in (g-k). Scale bar is 1 mm (b-f) and 500 μm for selected areas (dotted line (g-h)), magnification ×10. (l) MCTS formation and size quantification during a 30 day period: 500-10,000, 10,000-20,000 and >20,000 μm^2 for small, medium and large spheroids, respectively. (m) Frequency of MCTS distribution as a function of time cultured.

To further evaluate our bioprinted *in vitro* tumor model viability was quantified using a live/dead assay. A significant number of the MCTS (Figure 7b) appear viable while a necrotic core occurs dependent upon MCTS size (Figure 7c-f). The structure of the MCTS inside the gel was visualized using environmental Scanning Electron Microscopy (eSEM). Medium (Figure 7g) and small (Figure 7h) MCTS were distributed within the samples and differ significantly from SEM images of the hydrogel without cells (Figure 4c-d) and SEM images of hydrogel containing cells and MCTS (Figure 7g-h).

Conventional models of breast cancer have challenges in the formation and study of physiological mimicking MTCS due to their lack of spatial cellular heterogeneity and dependence on external stimuli or stresses that may influence cell function or behavior. 3D bioprinting technology overcomes some of the challenges by enabling the fabrication of heterogeneous *in vitro* models in highly biocompatible hydrogels with predetermined initial locations and concentrations of both cancer cells and cancer-associated cells.

Alginate and gelatin are used as a biocompatible composite hydrogel-based bioink to embed and extrude breast cancer cells and CAFs via pneumatic pressure into preprogrammed initial locations. The alginate component of the gel imparts

viscous properties during printing and is ionically cross-linked post-extrusion to provide mechanical reinforcement, while the gelatin component provides elastic characteristics during printing in addition to bioactive moieties that promote cell adhesion during culture. These composite hydrogels have tunable mechanical properties including their shear moduli, loss factor, and complex viscosity that can be modulated for different applications.

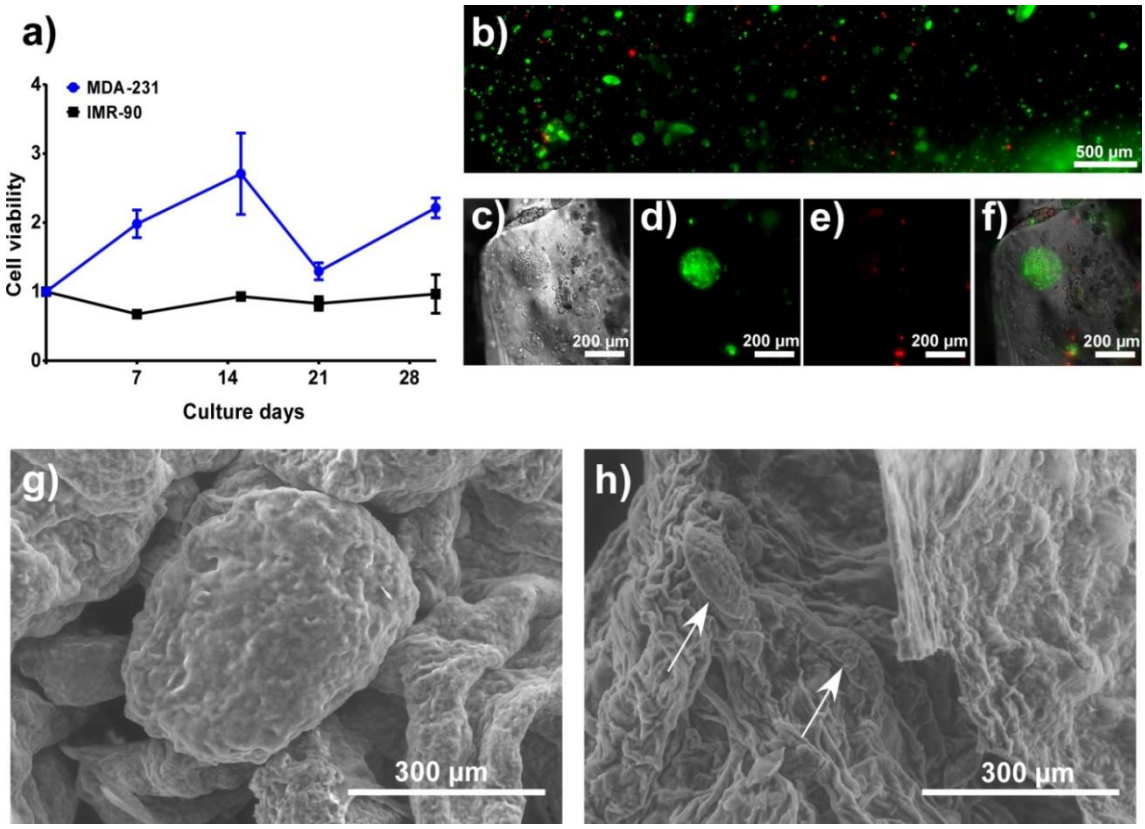

Figure 7. Metabolic activity and MCTS development. (a) fold metabolic activity of the MDA-MB-231-GFP and mCherry-IMR-90 during 30 days of culture within the hydrogel. (b) Live/Dead assay of unlabeled MDA-MB-231 cells after 21 days of culture with a representative full view (b) across the width of the entire sample. (c) magnified bright field image of a representative MTCS, (d) fluorescence image of live cells stained with the live/dead assay, (e), fluorescence image of dead cells

stained with the live/dead assay, (f) merged bright field and fluorescent live/dead assay images, (g-h) SEM images of MDA-MB-231 MCTS within the gel after 21 days of culture showing (g) medium and (h) small MTCS under a magnification of ×150.

The current methods to produce MCTS force the single cells to form aggregated by physical confinement [23] or chemical induction of MCTS [24]. This kind of technics could modified the protein expression driving cells to show different behavior that they have in natural tumor environment. Our hydrogel allowed to cells the facility to proliferate and form different sizes of MCTS similar as occur in body environment. Furthermore, the internal viscosity of our hydrogel helped to cell migrations as well as cell cross talking useful for migration of MTCS and CAFs.

The alginate/gelatin matrix is a biocompatible and bioprintable material for constructing heterogeneous breast cancer *in vitro* models with tunable mechanical and chemical characteristics in a biomimetic environment. Induction of MCTS without chemical and physical stresses for over 30 days in 3D culture can be achieved using this bioprinted system. This study provides insights in reconstructing physiological *in vitro* tissue models with mimetic spatial cellular heterogeneity that can enable insight into cell-cell interactions, diagnostic and therapeutic discovery, and tumorigenesis mechanisms.

Acknowledgements

Tao Jiang and Jose G. Munguia-Lopez contributed equally to this work. Tao Jiang thanks the China Scholarship Council (201403170354) and McGill

Engineering Doctoral Award (90025) for his scholarship. Jose G. Munguia-Lopez thanks CONACYT for his scholarship (250279) and Becas Mixtas 2015-2016 (290936). Joseph M. Kinsella thanks the National Science and Engineering Research Council, the Canadian Foundation for Innovation, the Townshend-Lamarre Family Foundation, and McGill University.

References

[1] a) S. Cleator, W. Heller, R. C. Coombes, The lancet oncology 2007, 8, 235; b) R. Dent, M. Trudeau, K. I. Pritchard, W. M. Hanna, H. K. Kahn, C. A. Sawka, L. A. Lickley, E. Rawlinson, P. Sun, S. A. Narod, Clinical Cancer Research 2007, 13, 4429; c) W. D. Foulkes, I. E. Smith, J. S. Reis-Filho, New England journal of medicine 2010, 363, 1938.

[2] a) D. Quigley, A. Balmain, Nature Reviews Genetics 2009, 10, 651; b) W. G. Stetler-Stevenson, S. Aznavoorian, L. A. Liotta, Annual review of cell biology 1993, 9, 541.

[3] a) G. Rijal, W. Li, Biomaterials 2016, 81, 135; b) L. B. Weiswald, D. Bellet, V. Dangles-Marie, Neoplasia 2015, 17, 1.

[4] a) I. Cornil, D. Theodorescu, S. Man, M. Herlyn, J. Jambrosic, R. Kerbel, Proceedings of the National Academy of Sciences 1991, 88, 6028; b) M. Gleave, J. Hsieh, A. Von Eschenbach, L. Chung, The Journal of urology 1992, 147, 1151; c) J. L. Camps, S.-M. Chang, T. Hsu, M. R. Freeman, S.-J. Hong, H. E. Zhau, A. C. von Eschenbach, L. Chung, Proceedings of the National Academy of Sciences 1990, 87, 75.

[5] a) E. Cukierman, R. Pankov, D. R. Stevens, K. M. Yamada, Science 2001, 294, 1708; b) F. Grinnell, Trends in cell biology 2003, 13, 264; c) K. M. Yamada, E. Cukierman, Cell 2007, 130, 601.

[6] a) V. L. Tsang, A. A. Chen, L. M. Cho, K. D. Jadin, R. L. Sah, S. DeLong, J. L. West, S. N. Bhatia, The FASEB Journal 2007, 21, 790; b) D. Huh, G. A. Hamilton, D. E. Ingber, Trends in cell biology 2011, 21, 745; c) S. H. Oh, S. G. Kang, E. S. Kim, S. H. Cho, J. H. Lee, Biomaterials 2003, 24, 4011.

[7] S. Knowlton, S. Onal, C. H. Yu, J. J. Zhao, S. Tasoglu, Trends in biotechnology 2015, 33, 504.

[8] a) V. Chan, P. Zorlutuna, J. H. Jeong, H. Kong, R. Bashir, Lab on a Chip 2010, 10, 2062; b) B. Derby, Science 2012, 338, 921; c) F. P. Melchels, J. Feijen, D. W. Grijpma, Biomaterials 2010, 31, 6121; d) S. Tasoglu, U. Demirci, Trends in biotechnology 2013, 31, 10.

[9] R. Chang, J. Nam, W. Sun, Tissue Engineering Part A 2008, 14, 41.

[10] M. Nakamura, A. Kobayashi, F. Takagi, A. Watanabe, Y. Hiruma, K. Ohuchi, Y. Iwasaki, M. Horie, I. Morita, S. Takatani, Tissue engineering 2005, 11, 1658.

[11] K. Nair, M. Gandhi, S. Khalil, K. C. Yan, M. Marcolongo, K. Barbee, W. Sun, Biotechnol. J 2009, 4, 1168.

[12] F. Xu, J. Celli, I. Rizvi, S. Moon, T. Hasan, U. Demirci, Biotechnology journal 2011, 6, 204.

[13] a) U. Bhutani, A. Laha, K. Mitra, S. Majumdar, Materials Letters 2016, 164, 76; b) M. A. Abd El-Ghaffar, M. S. Hashem, M. K. El-Awady, A. M. Rabie, Carbohydrate polymers 2012, 89, 667.

[14] a) E. Rosellini, C. Cristallini, N. Barbani, G. Vozzi, P. Giusti, Journal of biomedical materials research. Part A 2009, 91, 447; b) R. Yin, Y. Huang, C. Huang, Y. Tong, N. Tian, Materials Letters 2009, 63, 1335.

[15] Q. Jiang, J. Xu, T. Li, C. Qiao, Y. Li, Journal of Macromolecular Science, Part B 2013, 53, 133.

[16] C. G. Gomez, M. Rinaudo, M. A. Villar, Carbohydrate Polymers 2007, 67, 296.

[17] E. Fennema, N. Rivron, J. Rouwkema, C. van Blitterswijk, J. de Boer, Trends in biotechnology 2013, 31, 108.

[18] M. A. d. Faute, L. Laurent, D. Ploton, M.-F. Poupon, J.-C. Jardillier, H. Bobichon, Clinical & Experimental Metastasis 2002, 19, 161.

[19] S. Nath, G. R. Devi, Pharmacol Ther 2016, 163, 94.

[20] A. Ivascu, M. Kubbies, International journal of oncology 2007, 31, 1403.

[21] C. C. Park, H. Zhang, M. Pallavicini, J. W. Gray, F. Baehner, C. J. Park, M. J. Bissell, Cancer research 2006, 66, 1526.

[22] a) G. Mehta, A. Y. Hsiao, M. Ingram, G. D. Luker, S. Takayama, Journal of controlled release : official journal of the Controlled Release Society 2012, 164, 192; b) K. Bloch, H. Smith, V. van Hamel Parsons, D. Gavaghan, C. Kelly, A. Fletcher, P. Maini, R. Callaghan, Cell Biochem Biophys 2014, 68, 615.

[23] C. Han, S. Takayama, J. Park, Scientific reports 2015, 5, 11891.

[24] R. Akasov, D. Zaytseva-Zotova, S. Burov, M. Leko, M. Dontenwill, M. Chiper, T. Vandamme, E. Markvicheva, International journal of pharmaceutics 2016, 506, 148.

6. Chapter V

A nitrogen-doped carbon nanotube, alginate and alginate/gelatin composite hydrogels as a 3D bioprinting ink

Alginate and gelatin are two of the most common materials used as printable hydrogels. However, alginate has limited tunable physical properties that can be modulated via crosslinking. An alternative approach to crosslinking is to create composites between the biopolymer gels and nanomaterials such as carbon nanotubes (CNTs), which have unique physicochemical-mechanical properties with a large surface area that introduces a surface roughness that is present in the human extracellular matrix. Mixing CNTs with alginate/gelatin blend, or focal adhesion peptide modified alginate, can create bioprintable materials with tunable properties and broad applications ranging from tissue regeneration to cancer cell migration in 3D environments. Three types of composites were prepared: 1) alginate+nitrogen-doped CNTs (CN_x) hydrogel; 2) alginate/gelatin+CNx gels and 3) oxidized alginate covalently crosslinked with CN_x and mixed with an alginate/gelatin solution. As biological models, MDA-MB-231 and IMR-90 cells were used. Cells were separately blended in the hydrogels before printed by an extrusion-based printer. The samples were analyzed mechanically, physically, and biologically. Alginate hydrogels caused more stress for cells than alginate+CN_x gels. Aginate/gelatin hydrogels (with or without nanomaterials) showed biocompatibility with cells, as well as alginate-wrapped CNx hydrogels. The alginate/gelatin+CN_x composite hydrogel can enable the ability to tune properties such as the mechanical, electrical, or optical characteristics of the otherwise inert alginate gel.

A nitrogen-doped carbon nanotube, alginate and alginate/gelatin composite hydrogels as a 3D bioprinting ink

1. Introduction

Carbon nanotubes (CNTs) are graphitic sheets grown as hollow cylinders made of a single, double or several layers concentrically arranged capped by fullerene hemispheres. CNTs have diameters ranging from a few nanometers, 0.4 to 2 nm for single walled carbon nanotubes (SWCNTs), 2 to 200 nm for multi-wall carbon nanotubes (MWCNTs), and lengths ranging from hundreds of nanometers to micrometers [1-3]. Due to their physical, chemical, electrical and thermal properties [2], they have shown the potential to be used in drug delivery, biosensor, antimicrobial nanocomposite film and cellular scaffolding.

The physicochemical-mechanical properties and nano-sizes of CNTs provide them highly porosity and lightweight as wellas significantly large surface areas and similar surface roughness present naturally in collagen fibers of the extracellular matrix (ECM) [4]. It has been documented that CNT greatly influence cell adhesion, proliferation and differentiation; due to this, CNTs could provide a mimetic structure of ECM for use as cellular scaffolds [3, 5, 6].

Research on cellular response to either non-functionalized or functionalized (addition of functional groups on a graphite surface) MWCNT has been extensive. Chemical doping (carbon atoms substitution) with nitrogen of CNTs (CN_x) has presented positive effects on cellular biocompatibility [3, 7]. Non-functionalized and functionalized CNTs have been mixed with different polymers (to form composites) such as poly-DL-lactide [8], collagen [5, 9] and their derivate gelatin [10],

hydroxyapatite [11] to change their physicochemical properties, and then, increase their biocompatibility with mammalian cells to use these nanomaterials as scaffolds or biomimetic implants. CN_x has presented more positive effects on cellular response than other types of nanotubes (e.g. single walled, double walled, multi walled, non-functionalized or functionalized), this is due to the presence of nitrogen in the graphitic network [7]. For this reason, composites of CN_x could be better than others and could be used in tissue engineering.

The fabrication of patterned microstructures within a three-dimensional (3D) matrix is a challenge in tissue engineering and regenerative medicine. Bioprinting technology such as rapid prototyping and direct-writing is a leading novel technology for the fabrication of microstructures that mimic complex tissue modules [12]. In order to develop a biomimetic implant, fabrication methods and the selection of proper biomaterial are two crucial factors. The biomaterial should cover several features such as well mechanical elasticity and strength, diffusion properties, high porosity that allows the transport of nutrients, oxygen and waste [13].

Hydrogels are one of the most common matrixes employed in regenerative medicine due to their biocompatibility, interexchange of nutrients and oxygen, and highly hydrated 3D network that structurally resemble the EMC. Natural polymers such as collagen, alginate, and chitosan have better biocompatibility than synthetic polymer gels, but they have limitations in mechanical properties [13]. As mentioned above, CNT have great mechanical properties, and the use of these nanomaterials in combination with hydrogels could be an excellent material to use in tissue regeneration, by using a bioprinter for scaffold elaboration.

2. Materials and methods

2.1. Synthesis and purification CN_x

CN_x were synthesized using the chemical vapor deposition (CVD) method. As chemical precursors, 2.5 wt. % ferrocene in benzylamine was used to produce them. The solution was placed into a reservoir and atomized, then aerosol was carried by an Argon flow at 2.5 L/min into a quartz tube 100 cm in length, placed inside of a two tubular furnaces heated up to 850°C. After 30 min of synthesis, the quartz tube was cooled down to room temperature and CN_x were collected by inner scrape. CN_x purification was carried out by acid treatment of HNO_3:H_2SO_4 under sonication using an ultrasonic bath operating at 100 W (Branson 2510 Ultrasonic Cleaner, 42 kHz) during 12 h at room temperature. Samples were diluted with distillated water and recovered by filtration using 0.22 µm fluoropore PTFE membranes (Millipore).

2.2. Cell culture

Breast cancer cells (MDA-MB-231, labeled with GFP) and human cancer associated fibroblasts (IMR-90, labeled with mCherry) were cultured in Dulbecco's Modified Eagle Medium (DMEM, pH 7.2 supplemented with 10% fetal bovine serum (GIBCO), 100 U/mL penicillin, 100 µg/mL streptomycin and 0.25 µg/mL amphotericin B (SIGMA)) at 37°C and 5% of CO_2 until 80% confluence. Cells were harvested by incubation with a trypsin-EDTA solution for 10 min.

2.3 Preparation of alginate and alginate/gelatin hydrogels with CN_x

CN_x (0.01, 0.05, 0.1 %, w/v) in PBS (Phosphate-Buffered Saline) were suspended by sonication for 30 min. Then, 3% sodium alginate (Protanal LF 10/60 FT) or 3% alginate+7% gelatin (AG) mix (Sigma) was incorporated and stirred for 1 h at 60°C and 2 h more at room temperature (RT). Samples were transferred to clean tubes, centrifuged at 2,000 rpm during 5 min and storage at 4°C until use. Alginate, gelatin and CN_x powders were sterilized by UV-light overnight previous to mix. A and AG hydrogels without CN_x were used as control.

2.4 Oxidation of alginate and covalent crosslink with CN_x

To obtain alginate-wrapped CN_x (CN_x-A), 4 gr of sodium alginate was stirred in 300 mL of distillated water during 1 at 60 °C and then 3 h at RT. In parallel, 40 gr of sodium periodate was mixed in 100 mL of distillated until it was dissolved. A sodium periodate solution was poured into the alginate solution and stirred during 24 h at RT in dark bottles. The reaction was quenched by the addition of an excess of ethylene glycol (3.5 molar ratio), mixed for 30 min and 0.4 M NaCl was added. Oxidized alginate was recovered by precipitation with two volumes of ethanol, centrifuged at 2,500 rpm at RT for 5 min and washed with distillated water; then, oxidized alginate was precipitated again, dialyzed against water, freeze-dried and storage at -20 °C [14].

Oxidized alginate and CN_x were chemically crosslinked by carboxyl reaction. Briefly, 260 mg of oxidized alginate and 15 mg of CN_x were stirred separately each in 10 ml of 0.05 M MES buffer (2-morpholinoethane sulfonic acid, pH 5.40) at RT during 1 h. Subsequently, 0.192 M N-(3-dimethylaminopropyl)-N’-ethylcarbodiimide

(EDC) and 0.115 M N-hydroxysuccinimide (NHS) were dissolved in 40 mL MES buffer. Oxidized alginate and CN_x solutions were added to EDC/NHS solution and stirred for 4 h at RT. Finally, the CN_x-A sample was freeze-dried, dialyzed against water for 24 h, freeze-dried again and stored at -20 °C [15]. CN_x-A composite was added to AG hydrogel (AG+CN_x-A) at a final concentration of 0.1% for biological tests.

2.5 Mechanical, physico-chemical characterization and SEM imaging

Mechanical properties were characterized by rheometry. The data were taken by an oscillation rheometer MCR 302 (Anton Paar, US). A disk was fabricated by 3D printing to slice the material column into thin disks with dimension Φ25mm × 1mm prior to each test. A cylinder flat geometry with diameter 25mm (PP25) was mounted to the rheometer. All the experiments were triplicated.

FTIR experiments were carried out to confirm the presence of alginate and CN_x in the CN_x-A hydrogels. Hydrogels were freeze-dried and powdered to get their infrared spectra by using a FTIR-ATR spectrophotometer (Nicolet 6700/Smart iTR, Thermo Scientific), the results were plotted in a wavelength range from 4000 to 500 cm^{-1}. Raman characterization was performed by using a laser of 785 nm in alginate and alginate-CN_x hydrogels.

The internal structure of the hydrogels was analyzed by scanning electron microscopy (SEM, Hitachi SU-3500 Variable Pressure). Alginate hydrogels were crosslinked with 50 mM $CaCO_3$ and 100 mM D-gluconic acid δ-lactone (DGL) and AG hydrogels with 100 mM $CaCl_2$, rinse with PBS and incubated for 1 h at 37 °C;

then, rinsed with water, immediately frozen in liquid nitrogen and freeze-dried overnight. Samples were analyzed under SEM at 25.0 kV and 70 Pa.

2.6 Biological testing of hydrogel

For alginate and alginate+CN_x hydrogel, IMR-90 cell suspensions 1×10^6 cells/mL were mixed with the hydrogels and crosslinked with 50 mM $CaCO_3$ and 100 mM D-gluconic acid δ-lactone (DGL). For AG, AG-CN_x or AG-CN_x-A hydrogels MDA-MB-231 or IMR-90 cells at 1×10^6 cells/mL were mixed separately with the hydrogels, previously heated at 32°C, and 100 µL-disk were crosslinked by soaking in 100 mM $CaCl_2$ for 30 s and rinsed with PBS. Disks were incubated for 7 days and samples were taken at 24, 72 and 168 h at 37 °C/5% CO_2. Culture medium was changed each 2 days. The metabolic activity was determined by the MTS assay following the manufacture's procedure (Promega).

As a proof of concept, an extrusion bioprinter (BioScaffolder 3.1, GeSiM, Germany) with a G25 dispenser tip was used to print different models. Images of cell-laden hydrogels (disks and printed models) were taken by a confocal disk inverted microscope (Olympus IX83, Olympus Life Science) using a multi-position and z-stack confocal image, then a maximum stack arithmetic was used to create 2D image.

3. Results

Figure 1 shows three different schematic models to modify the viscoelastic properties of alginate and alginate/gelatin hydrogels. The first models represent the dispersion of CN_x followed by addition of alginate and gelatin polymers to create a

viscous solution that will crosslink with Ca^{++} ions (Figure 1a). The second model is the composite created by covalently binding oxidized alginate and CN_x, creating alginate-wrapped CN_x composite which will add to AG hydrogels (Figure 1b). The last schema is the representation of alginate-grafted CN_x, created by oxidation of alginate at 1.3% (Figure 1c). The three different matrices proposed are made by Ca^{++} crosslink reactions.

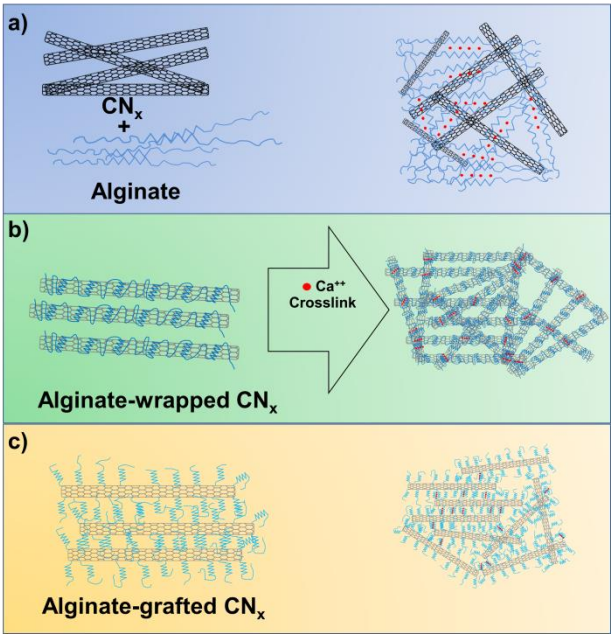

Figure 1. Schematic model of alginate+CN_x hydrogels matrix. CN_x mixed with alginate (a),10% (b) or 1.3% (c) oxidized alginate.

Following the schematic model 1, Figure 2 shows the physical characterization of alginate and alginate+CN_x hydrogels. The D (defect mode) and G (graphite mode) Raman bands at 1,311 and 1,586 cm^{-1} correspond to carbonaceous material (Figure 2a) while peaks at 811, 888, and 954 cm^{-1} correspond to skeletal C-C and C-O stretching, deformational C-C-H and C-C-O

bending modes of the alginate gel [16]. The alginate+CN_x spectra had all peaks suggesting that the polymer is not affected by CN_x.

According to the mechanical results, the addition of CN_x to alginate hydrogel did not modify the mechanical properties of this hydrogel (Figure 2b-d). This could be explained by the small quantity of CN_x used in the hydrogel. Following with the material characterization, SEM imaging was performed. Figure 3 shows the different matrix formed by alginate (Figure 3a), alginate+CN_x (Figure 3b) and alginate/gelatin (Figure 3c) hydrogels. All the matrices showed a high degree of porosity, but the hydrogel with CN_x also showed high content of fibers, which could help to support cell growth as well as encourage superior exchange rates of nutrients and gases.

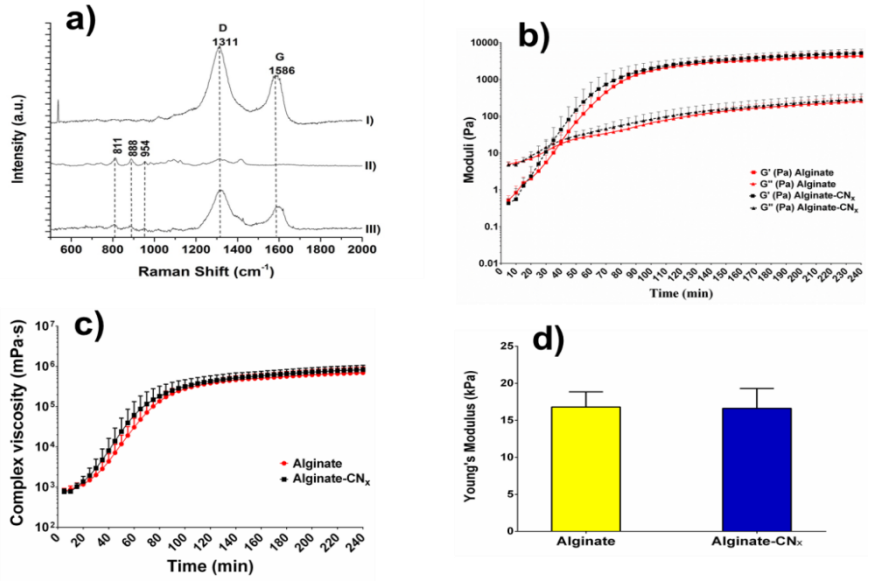

Figure 2. Physical characterization of alginate and alginate+CN_x(0.1%). a) Raman spectra of CN_x (I), alginate (II) and alginate-CN_x hydrogel (III). Dashed lines indicate the corresponding peaks for alginate and CN_x typical peaks. Gelation time

(b), viscosity (c) and elastic modulus (d) of alginate and alginate-CN_x hydrogels. Data are plotted as mean ± SD. $P < 0.05$), n ≥ 3.

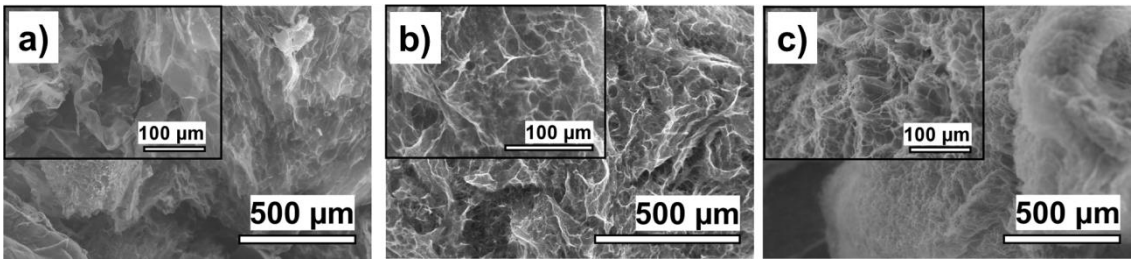

Figure 3. Morphology of alginate, alginate+CN_x and alginate-gelatin hydrogels. SEM image of alginate (a, ×80), alginate+CN_x 0.1% (b, ×100) and alginate-gelatin (c, ×100) hydrogels with a magnified image (inset ×500).

Alginate and alginate+CN_x were mixed with IMR-90 cells. Figure 4 shows the viability of cells embedded in this hydrogels. Cell membrane integrity results (trypan blue assay) showed a decrease viability of IMR-90 in alginate samples after 24 h, while cells in alginate+CN_x hydrogels kept their viability near to 90%. The viability of the cells decreased in all cases after 72 h (Figure 4a). However, metabolic activity of cells (MTS assay) showed that cells had viability over 100% in all case (Figure 4b). These results suggest that cells in alginate hydrogels had more metabolic activity, indicating cell stress due to the low quantity of cells in the hydrogel after 72 h of culture.

Since alginate hydrogel damaged the cells more that alginate+CN_x, the next step was to analyze the biological properties of AG and AG+CN_x hydrogels. In Figure 5 is presented the results of the metabolic assay of two cells types embedded in AG and AG+CN_x hydrogels using different concentration of nanomaterial. Concentration of 0.1% CN_x decreased the metabolic activity of IMR-90 cells after 24 h of incubation (Figure 5a), meanwhile 0.05 and 0.1% of CN_x

increased the metabolic activity of MDA-MB-231 cells after 72 h (Figure 5b).

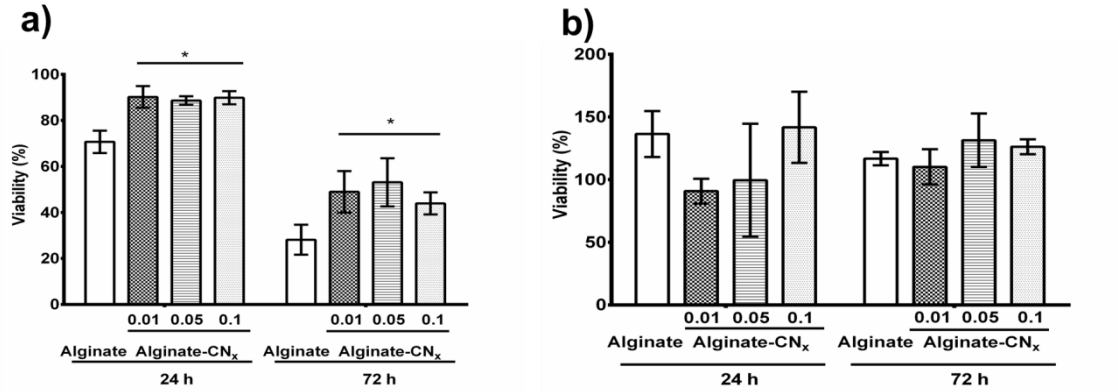

Figure 4. Membrane integrity and metabolic activity of IMR-90 cells determined by trypan blue (a) and MTS (b) assays. Data are plotted as mean ± SD. $P < 0.05$), n ≥ 3.

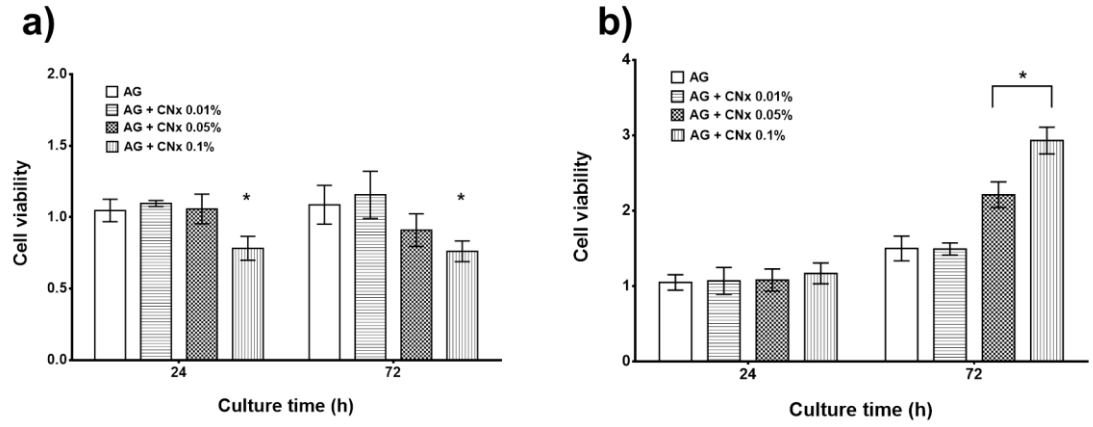

Figure 5. Metabolic activity of IMR-90 (a) and MDA-231 (b) cells embedded in alginate/gelatin (AG) and alginate/gelatin+CN_x hydrogels. Data are plotted as mean ± SD. $P < 0.05$), n ≥ 3.

Due to the simple addition of CN_x to hydrogels did not modify the mechanical properties of hydrogels; chemically crosslink of alginate with CN_x was done. Figure 6 shows the FTIR spectra of CN_x-A composite and the metabolic activity of MDA-MB-231 cells. The peak at 1,722 cm^{-1} corresponds to carboxyl

groups in oxidized alginate (Figure 6a, III); meanwhile, a peak at 3,295.68 cm^{-1} appears, which corresponds to amine groups of CN_x (Figure 6a, II). The absence of these peaks in CN_x-A composite confirmed the crosslinked material (Figure 6a, I). As a preliminary result, the metabolic activity of MDA cells was not affected by the presence of either CN_x or CN_x-A composite after 7 days of culture (Figure 6b). This result suggest that CN_x and derivate are biocompatibles with MDA-MB-231 cells.

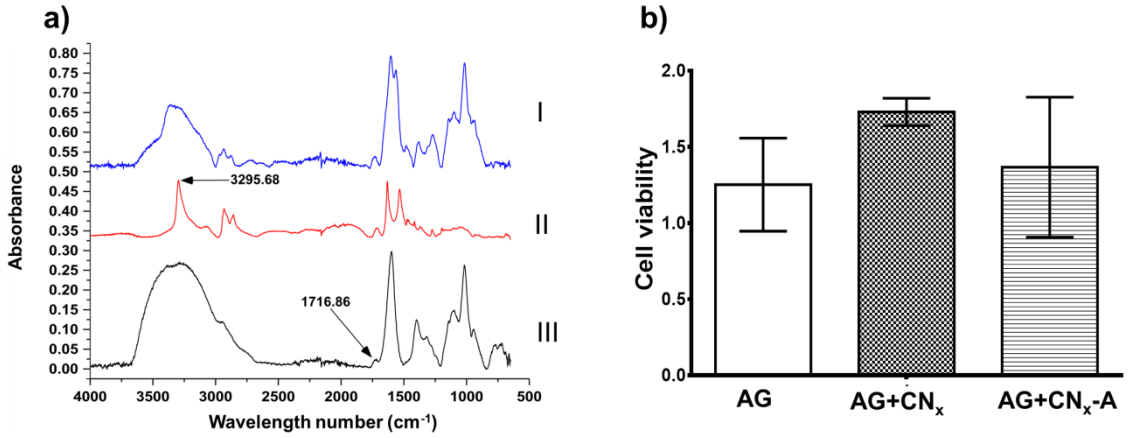

Figure 6. FT-IR spectrum of alginate-wrapped CN_x (a, I), CNx (a, II) and oxidized alginate (a, III). Metabolic activity of MDA-231 cells (b) embedded into alginate/gelatin (AG), alginate/gelatin+CN_x (AG+CN_x) or alginate/gelatin+alginate-wrapped CN_x (AG-CN_x-A) hydrogels. Cells were mixed separately with hydrogels and cultured for 7 days. Data are plotted as mean ± SD. $P < 0.05$), n ≥ 3.

As a proof of concept, AG+CN_x hydrogel was used for printing propose. Figure 7 shows some *in vitro* models of cell-laden gels. This material showed high stability in complex geometries as well as good dispersion of cells. The alginate/gelatin-CNTs composite hydrogel can enable the ability to tune properties

such as the mechanical, electrical, or optical characteristics of the otherwise inert alginate gel.

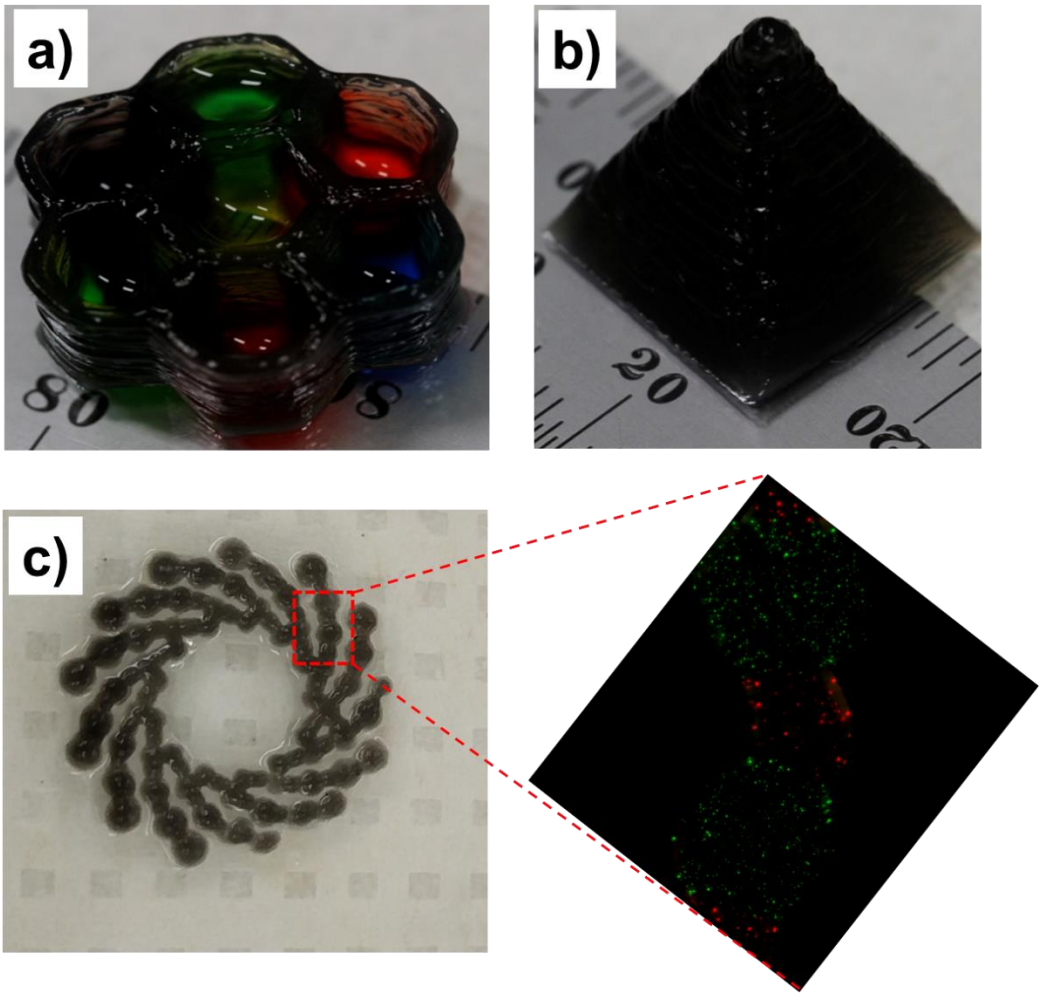

Figure 7. Bioprinted models using AG-CN_x hydrogel. Honey comb (a), pyramid (b) models and an IPICyT stamp model containing IMR-90 (red) and MDA-231 (green) cells (c).

Acknowledgements

Jose Gil Munguia-Lopez thanks CONACYT for his scholarship (250279) and Becas Mixtas 2015-2016 (290936). Tao Jiang thanks the China Scholarship Council and McGill Engineering Doctoral Award for his scholarship. Dr. Emilio

Munoz-Sandoval thanks partial support from 220744 CONACYT grant. Prof. Kinsella thanks McGill University, Canadian Foundation for Innovation, and the Natural Science and Engineering Research Council for support. We also thank Prof. Dan V. Nicolau and Prof. Allen J. Ehrlicher for providing instruments, and we thank Dr. Hossein Khadivi Heris and PhD Ghulam Jalani for their kind help.

References

[1] Cui HF, Vashist SK, Al-Rubeaan K, Luong JH, Sheu FS. Interfacing carbon nanotubes with living mammalian cells and cytotoxicity issues. Chem Res Toxicol. 2010;23:1131-47.

[2] Iijima S. Helical microtubules of graphitic carbon. Nature. 1991;354:56-8.

[3] Zhao ML, Li DJ, Yuan L, Yue YC, Liu H, Sun X. Differences in cytocompatibility and hemocompatibility between carbon nanotubes and nitrogen-doped carbon nanotubes. Carbon. 2011;49:3125-33.

[4] Hopley EL, Salmasi S, Kalaskar DM, Seifalian AM. Carbon nanotubes leading the way forward in new generation 3D tissue engineering. Biotechnol Adv. 2014;32:1000-14.

[5] Hirata E, Uo M, Nodasaka Y, Takita H, Ushijima N, Akasaka T, et al. 3D collagen scaffolds coated with multiwalled carbon nanotubes: Initial cell attachment to internal surface. Journal of Biomedical Materials Research Part B: Applied Biomaterials. 2010;93B:544-50.

[6] Ryoo SR, Kim YK, Kim MH, Min DH. Behaviors of NIH-3T3 fibroblasts on graphene/carbon nanotubes: proliferation, focal adhesion, and gene transfection studies. ACS Nano. 2010;4:6587-98.

[7] Carrero-Sanchez JC, Elias AL, Mancilla R, Arrellin G, Terrones H, Laclette JP, et al. Biocompatibility and toxicological studies of carbon nanotubes doped with nitrogen. Nano Lett. 2006;6:1609-16.

[8] Shao S, Zhou S, Li L, Li J, Luo C, Wang J, et al. Osteoblast function on electrically conductive electrospun PLA/MWCNTs nanofibers. Biomaterials. 2011;32:2821-33.

[9] MacDonald RA, Laurenzi BF, Viswanathan G, Ajayan PM, Stegemann JP. Collagen-carbon nanotube composite materials as scaffolds in tissue engineering. Journal of biomedical materials research Part A. 2005;74:489-96.

[10] Ostrovidov S, Shi X, Zhang L, Liang X, Kim SB, Fujie T, et al. Myotube formation on gelatin nanofibers - multi-walled carbon nanotubes hybrid scaffolds. Biomaterials. 2014;35:6268-77.

[11] Lu XY, Qiu T, Wang XF, Zhang M, Gao XL, Li RX, et al. Preparation of foam-like carbon nanotubes/hydroxyapatite composite scaffolds with superparamagnetic properties. Applied Surface Science. 2012;262:227-30.

[12] Hong S, Song SJ, Lee JY, Jang H, Choi J, Sun K, et al. Cellular behavior in micropatterned hydrogels by bioprinting system depended on the cell types and cellular interaction. Journal of bioscience and bioengineering. 2013;116:224-30.

[13] Dolati F, Yu Y, Zhang Y, De Jesus AM, Sander EA, Ozbolat IT. In vitro evaluation of carbon-nanotube-reinforced bioprintable vascular conduits. Nanotechnology. 2014;25:145101.

[14] Gomez CG, Rinaudo M, Villar MA. Oxidation of sodium alginate and characterization of the oxidized derivatives. Carbohydrate Polymers. 2007;67:296-304.

[15] Wissink MJB, Beernink R, Pieper JS, Poot AA, Engbers GHM, Beugeling T, et al. Immobilization of heparin to EDC/NHS-crosslinked collagen. Characterization and in vitro evaluation. Biomaterials. 2001;22:151-63.

[16] Hernández R, Sacristán J, Mijangos C. Sol/Gel Transition of Aqueous Alginate Solutions Induced by Fe2+ Cations. Macromolecular Chemistry and Physics. 2010;211:1254-60.

7. References

[1] Iijima S. Helical microtubules of graphitic carbon. Nature. 1991;354:56-8.

[2] Pérez-López B, Merkoçi A. Carbon nanotubes and graphene in analytical sciences. Microchimica Acta. 2012;179:1-16.

[3] Ströck, M. Eight allotropes of carbon. PNG image free lincense, wikimedia. 2006.

[4] Novoselov KS, Geim AK, Morozov SV, Jiang D, Zhang Y, Dubonos SV, et al. Electric Field Effect in Atomically Thin Carbon Films. Science. 2004;306:666-9.

[5] Cui HF, Vashist SK, Al-Rubeaan K, Luong JH, Sheu FS. Interfacing carbon nanotubes with living mammalian cells and cytotoxicity issues. Chem Res Toxicol. 2010;23:1131-47.

[6] Zhao ML, Li DJ, Yuan L, Yue YC, Liu H, Sun X. Differences in cytocompatibility and hemocompatibility between carbon nanotubes and nitrogen-doped carbon nanotubes. Carbon. 2011;49:3125-33.

[7] Singh V, Joung D, Zhai L, Das S, Khondaker SI, Seal S. Graphene based materials: Past, present and future. Progress in Materials Science. 2011;56:1178-271.

[8] Ruiz ON, Fernando KAS, Wang B, Brown NA, Luo PG, McNamara ND, et al. Graphene Oxide: A Nonspecific Enhancer of Cellular Growth. ACS Nano. 2011;5:8100-7.

[9] Shin KY, Lee S, Hong S, Jang J. Graphene size control via a mechanochemical method and electroresponsive properties. ACS Appl Mater Interfaces. 2014;6:5531-7.

[10] Pinto AM, Goncalves IC, Magalhaes FD. Graphene-based materials biocompatibility: A review. Colloids and surfaces B, Biointerfaces. 2013;111C:188-202.

[11] Dong H, Ding L, Yan F, Ji H, Ju H. The use of polyethylenimine-grafted graphene nanoribbon for cellular delivery of locked nucleic acid modified molecular beacon for recognition of microRNA. Biomaterials. 2011;32:3875-82.

[12] Lu F, Gu L, Meziani MJ, Wang X, Luo PG, Veca LM, et al. Advances in Bioapplications of Carbon Nanotubes. Advanced Materials. 2009;21:139-52.

[13] Harrison BS, Atala A. Carbon nanotube applications for tissue engineering. Biomaterials. 2007;28:344-53.

[14] Zhang Y, Yu Y, Dolati F, Ozbolat IT. Effect of multiwall carbon nanotube reinforcement on coaxially extruded cellular vascular conduits. Materials science & engineering C, Materials for biological applications. 2014;39:126-33.

[15] Hopley EL, Salmasi S, Kalaskar DM, Seifalian AM. Carbon nanotubes leading the way forward in new generation 3D tissue engineering. Biotechnol Adv. 2014;32:1000-14.

Anexos

A) Production of CN_x by chemical vapor deposition (CVD) and purification of nanomaterials

1. The CVD system consisting of an aerosol generator and a 100-cm-long quartz tube placed inside of two 60-cm-long horizontal tube furnaces together and a middle tramp of acetone (Figure 1).
2. Prior to CN_x synthesis, the furnaces are heated to 850 °C and temperature is kept constant.
3. A solution of 2.5 wt. % ferrocene in benzylamine is sonicated for 1 h.
4. Three hundred milliliters of 2.5 wt. % ferrocene in benzylamine solution are placed into the piezo-driven aerosol generator.
5. The generated spray (aerosol) is carried by argon flow at 2.5 L/min through heated quartz tube.
6. After 30 min of synthesis, the quartz tube is cooled down at room temperature (RT) and washing with ethanol to remove benzylamine, and acetone to remove amorphous carbon and non-add CN_x.
7. For CN_x recovery, the quartz tube is divided into fractions of 1 cm (Figure 2), and then each fraction is recovered by inner scrap and collected separately.
8. CN_x fractions are sonicated by ultrasonic bath operating at 100 W (Branson 2510 Ultrasonic Cleaner, 42 kHz) with absolute ethanol during 1 h at RT and filtrated using 0.45 µm membrane filters.
9. CN_x are recovered from membranes and put into Erlenmeyer flask where they are sonicated again in presence of acid treatment (HNO_3:H_2SO_4, 1:3)

during 12 h on ice. The ratio of acid:CN_x is 1:1 (1 mL of acid mix per 1 mg of nanomaterials).

10. Purified CN_x are diluted with distillated water, keep on repose during 48 h and filtered with 0.45 µm membrane filters.
11. Finally, CN_x are recovered from filters and died at 60°C during 24 h.

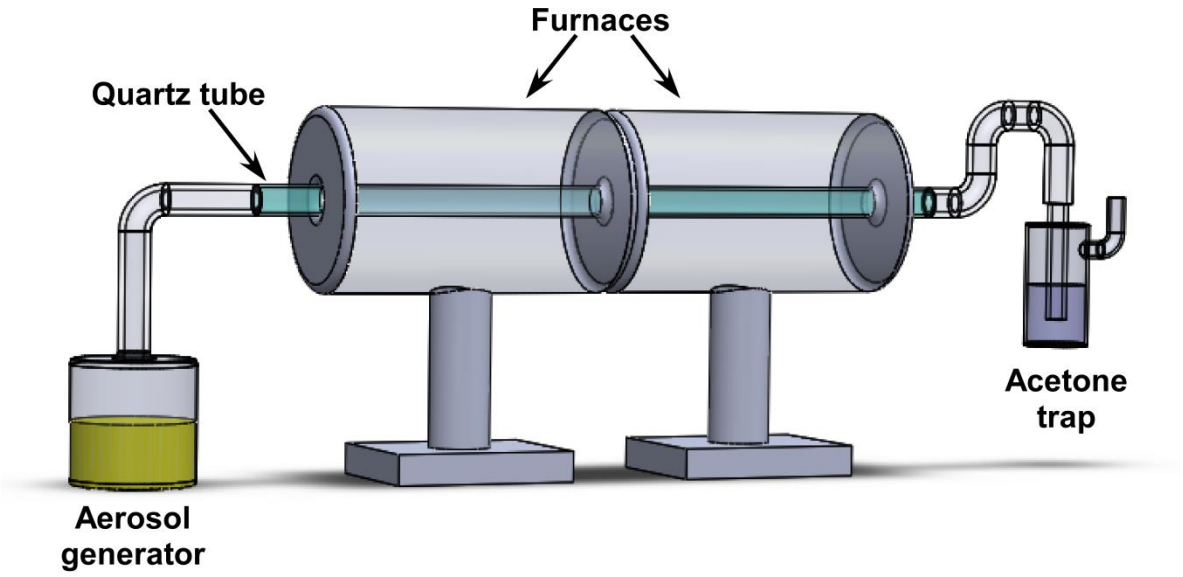

Figure 1. Schematic model of synthesis of CN_x using two furnaces and a middle trap of acetone.

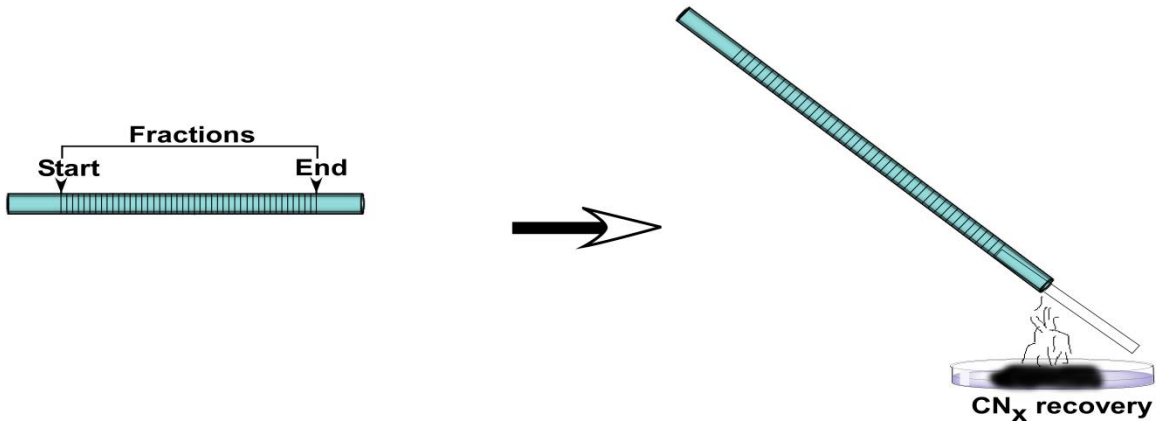

Figure 2. Recovery of CN_x fractions by inner scrape.

B) Publication

Effects of Nitrogen-Doped Multiwall Carbon Nanotubes on Murine Fibroblasts

J. G. Munguía-Lopez, E. Muñoz-Sandoval, J. Ortiz-Medina, F. J. Rodriguez-Macias, and A. De Leon-Rodriguez

Journal of Nanomaterials (Open Access)

Volume 2015 (2015), Article ID 801606, 7 pages

For access to full document, please type the following link:

DOI:10.1155/2015/801606

Hindawi Publishing Corporation
Journal of Nanomaterials
Volume 2015, Article ID 801606, 7 pages
http://dx.doi.org/10.1155/2015/801606

Research Article

Effects of Nitrogen-Doped Multiwall Carbon Nanotubes on Murine Fibroblasts

J. G. Munguía-Lopez,[1] E. Muñoz-Sandoval,[2] J. Ortiz-Medina,[2,3] F. J. Rodriguez-Macias,[4] and A. De Leon-Rodriguez[1]

[1]*Molecular Biology Division, Instituto Potosino de Investigación Científica y Tecnológica (IPICYT), Camino a la Presa San José 2055, Colonia Lomas 4a Sección, 78216 San Luis Potosí, SLP, Mexico*
[2]*Advanced Materials Department, Instituto Potosino de Investigación Científica y Tecnológica (IPICYT), Camino a la Presa San José 2055, Colonia Lomas 4a Sección, 78216 San Luis Potosí, SLP, Mexico*
[3]*Research Center for Exotic Nanocarbons (JST), Shinshu University, Wakasato 4-17-1, Nagano 380-8553, Japan*
[4]*Department of Fundamental Chemistry, Universidade Federal de Pernambuco, Avenida Proessor Luiz Freire, 50740-540 Recife, PE, Brazil*

Correspondence should be addressed to A. De Leon-Rodriguez; aleonr@ipicyt.edu.mx

Received 13 July 2015; Accepted 11 August 2015

Academic Editor: Faik Oktar

The effect of nitrogen-doped multiwall carbon nanotubes (CN_x) on the proliferation of NIH-3T3 murine fibroblasts is presented. CNTs were dispersed in distillated water and incubated with mammalian cells in order to evaluate their toxicity. Also, the influence of factors such as dosage (7 and 70 μg/mL), exposure time (24 to 96 h), and the exposure route (before and after cell liftoff) on the cell proliferation was evaluated. When the CN_x were simultaneously incubated with the cells, the control culture reached a maximum cell concentration of $1.3 \times 10^5 \pm 3.4 \times 10^4$ cells per well at 96 h, whereas cultures with 7 μg/mL reached a concentration of $2.6 \times 10^4 \pm 5.3 \times 10^3$ cells. In the case of 70 μg/mL of CN_x most of the cells were dead. The CN_x that were added 24 h after cell dissociation showed that live cells decreased, with a cell concentration of $9.6 \times 10^4 \pm 9 \times 10^3$ for 7 μg/mL and $5.5 \times 10^4 \pm 9.5 \times 10^3$ for 70 μg/mL, in contrast to control cultures with $1.1 \times 10^6 \pm 1.5 \times 10^4$. The results showed that the CN_x had cytotoxic effects depending on the concentration and exposure route.

1. Introduction

A wide range of nanomaterials has been developed for several applications over the past few years. Due to their physical, chemical, electrical, and thermal properties, and since their discovery in 1991 [1], carbon nanotubes (CNTs) have shown a potential for use in drug delivery, biosensor, antimicrobial nanocomposite film, and cellular scaffolding. CNTs are tiny hollow cylinders, made from a single, double, or several layers of graphene that are concentrically arranged and capped by fullerene hemispheres. They have diameters ranging from 0.4 to 2 nm for single walled carbon nanotubes (SWCNTs) and from 2 to 200 nm for multiwall carbon nanotubes (MWCNTs), and lengths ranging from hundreds of nanometers to micrometers [1–3]. Since CNTs have an asbestos-like shape, research into their toxicity and potential risks to human health has been intensified [4–7].

Studies on cellular response in nonfunctionalized or functionalized (addition of functional groups on a graphite surface) MWCNT have been extensive. Chemical doping (carbon atoms substitution) with nitrogen of CNTs (CN_x) was suggested to have positive effects on mice survival [8] and showed an improvement in cell-adhesion strength, viability, and proliferation of mammalian cells [3, 9], in contrast with the MWCNT. However, cytotoxic effects of CN_x have also been reported, where long length CN_x were more toxic than other functionalized CNTs [10]. Researches have demonstrated that cells exhibited variable responses to CNTs depending on different factors such as the method of synthesis, impurities, length and diameter, type (pristine,

functionalized, and doped), degree of dispersion/agglomeration, dispersant, CNT concentration, time exposure, cellular type, and protein adsorption [2, 5, 6, 8, 11, 12]. Due to the inconsistency in CN_x biocompatibility, more studies regarding cell response to these nanomaterials are necessary.

In the body, cell motility and wound healing are carried out by cell detachment, which is generated by proteolytic processes using endogenous proteases [13]. One of the most common enzymatic methods used for cell detachment in adherent-cell-subculture is trypsinization; trypsin cuts adhesion proteins to yield disaggregated cells with a rounded appearance. Although many cells are able to tolerate trypsin digestion during a short period of time, trypsinization causes cell stress affecting cytoskeleton proteins that are involved in regulating cell adhesion, stability, and elasticity [14–16].

CNTs have the capacity to adsorb a wide range of proteins, especially those rich in histidine, tryptophan, and phenylalanine [12], and also adhesion proteins from extracellular matrix (fibronectins, collagen) and transmembrane-proteins (integrins) [17]. Since enzymatic cell detachment can produce residual fragments of adhesion proteins, these fragments could interact with CNTs altering the extracellular matrix metabolism which is regulated by a complex mechanism including cell-cell and cell-matrix interactions [13, 17]. For this reason, the knowledge of cell-CNTs interactions is essential for cell scaffold development that is used in tissue regeneration.

The aim of this study was to evaluate the possible toxic effect of CN_x on NIH-3T3 murine fibroblast stressed by enzymatic detachment and nonstressed cells, in which a natural cell detachment stress was simulated by a trypsin incubation during a short period of time. Exposure route was defined in this work as the way to add nanomaterials to cell cultures (stressed and nonstressed cells). Besides several parameters are required to determine if new materials are safe for biomedical use; the effects of CN_x concentration and exposure time were also evaluated.

2. Materials and Methods

2.1. Synthesis, Purification, and Characterization of CN_x. In this way, CN_x were synthesized by using the chemical vapor deposition (CVD) method. As a chemical precursor 2.5 wt% ferrocene in benzylamine was used; the solution was placed into a reservoir and atomized. The aerosol was carried by an Argon flow at 2.5 L/min into a quartz tube 100 cm in length, placed inside of two tubular furnaces heated at 850°C. After 30 min of synthesis, the quartz tube was then cooled at room temperature and the CN_x were collected by internal scraping. Then, the pristine CN_x were purified and dispersed by using a pulsed probe sonicator in water under reflux, followed by a reflux in 6 M HCl and filtration.

Consequently, the purified CN_x were analyzed by scanning electron microscopy (SEM) as follows: first, the nanomaterials were pounded into a whole powder and separated into equal portions. Then, each portion was loaded into pins and visualized by SEM (Philips-XL 30 SFEG; Dual Beam (FIB/SEM) FEI-Helios Nanolab 600 equipped with an EDX detector) to determine lengths, diameters, and chemical composition of CN_x. Raman characterization was performed using a laser of 633 nm in Raman Renishaw Micro-Raman equipment.

2.2. Preparation of Dispersion of Purified CN_x. Stocks of purified CN_x were dispersed in distillated water at 1 mg/mL. Then, the samples were sonicated by an ultrasonic bath at 42 kHz and 100 W (Branson 2510 Ultrasonic Cleaner), at 40°C for 8 h, having as a result stable dispersions; these conditions were strong enough to obtain no visible agglomerates of purified CN_x. Finally, all the stocks were stored at 4°C until further use.

2.3. Cytotoxicity Assays. The effects of purified CN_x on the viability of NIH-3T3 murine fibroblast were evaluated by using the Trypan-blue exclusion method. Briefly, the cells were defrosted and cultured in a basal-IMDM (Iscove's Modified Dulbecco's Medium, SIGMA) at pH 7.2 and supplemented with 10% fetal bovine serum (GIBCO), 100 U/mL penicillin, 100 μg/mL streptomycin, and 0.25 μg/mL amphotericin B (SIGMA), using 24-well plates (Corning) over a period of 72 h in a humidity chamber at 37°C and CO_2 5% (Shell-Lab). After three passes, when 80% of cellular confluence was reached, the cells were washed twice gently with PBS (pH 7.2) and then harvested by incubation with trypsin-EDTA (0.25%-1X, GIBCO) for 10 min. Cell suspensions with a density of 2×10^3 cells per well were added into 96-well plates in absence or presence of purified CN_x at final concentrations of 7 and 70 μg/mL. For exposure route experiments, purified CN_x were added (1) immediately after cell dissociation (stressed cells) or (2) fibroblasts were firstly incubated for 24 h and then purified CN_x were added into each well (nonstressed cells). Samples were washed twice gently with PBS, incubated with trypsin for 6 min, and cells were counted by using the Trypan-blue method. During the 96 h of exposure with the nanomaterial, samples were taken each 24 h. NIH-3T3 cell cultures without nanomaterials were used as control. To avoid variation on purified CN_x concentration in cell cultures when medium was changed, kinetics were carried out using a working volume of 250 μL without medium replacement.

2.4. Statistics. The data is presented as the mean ± standard deviation, with a statistical comparison of one- and two-way ANOVA. We used Dunnett's posttests to compare treatments with control groups, and p values <0.05 were considered significant. All experiments were done in triplicate.

3. Results and Discussion

3.1. Determination of Length and Diameter of Purified CN_x. Figure 1 shows SEM micrographs and size distribution of purified CN_x. Micrographs by the XL30 and Helios are shown in Figures 1(a) and 1(c), respectively. A few bundles were found in purified CN_x samples to determine the lengths of nanomaterials (Figure 1(a)). The length range was 10 to 130 μm, being the most abundant lengths of 40–50 μm (Figure 1(b)). In micrographs of purified CN_x, the nanomaterials seemed to have similar diameters (Figure 1(c)), but, after

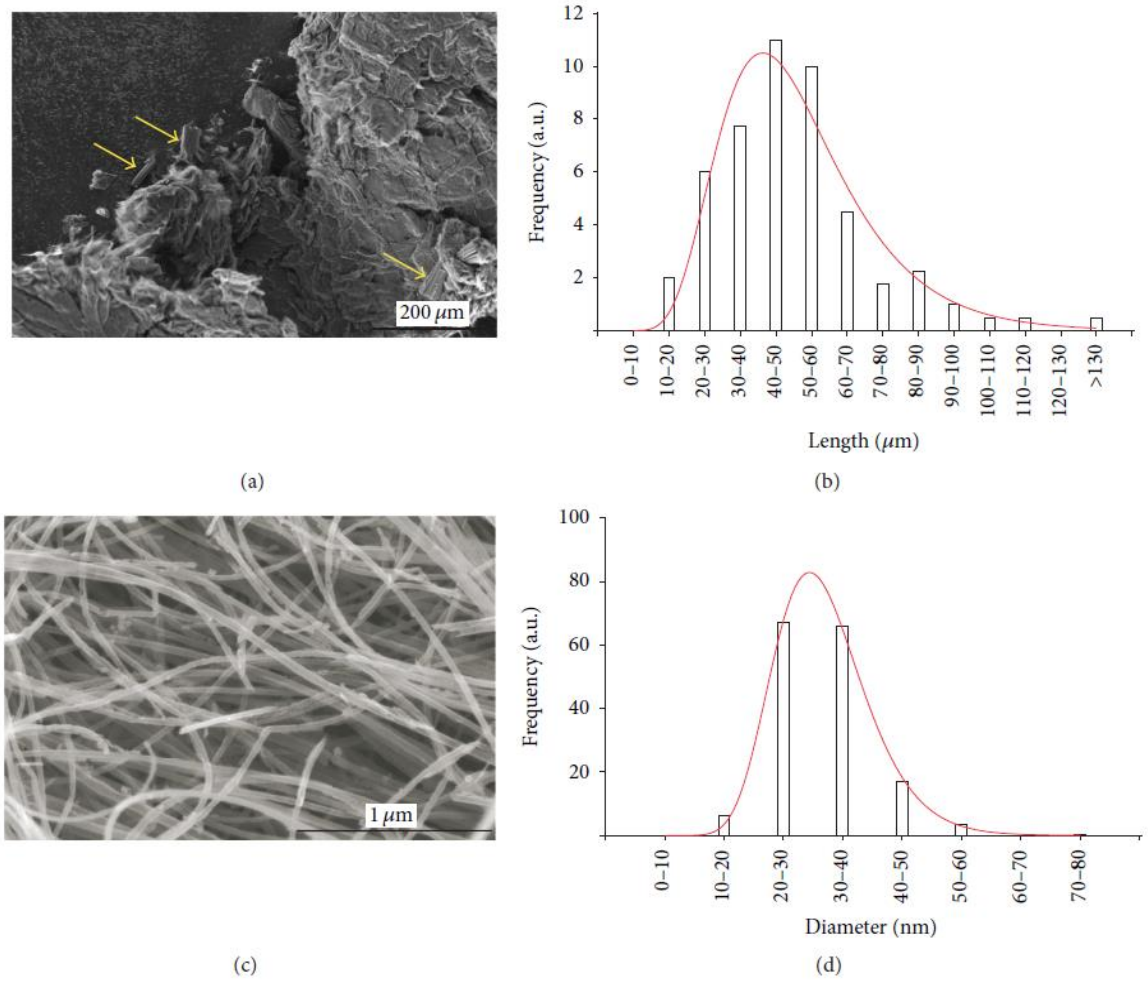

FIGURE 1: SEM micrographs of CN_x morphology and size distribution. Lengths were obtained from bundles of purified CN_x ((a), pointed with yellow arrows) and plotted to generate distribution patterns. Diameters were obtained from individual tubes from Helios SEM images (c) and distribution was plotted (d).

an analysis with the Helios microscopy, the diameter sizes were around 10–80 nm, with a diameter predominance of 20–40 nm (Figure 1(d)).

Nanomaterial sizes were obtained from their own bundles and short "fibrous" structures (Figure 2). The number of bundles among different samples of purified CN_x was small (around 38 bundles) (Figures 2(a)–2(c), yellow arrows), as well as in between the same sample (Figures 2(d)–2(f)). Since purified CN_x samples were mostly agglomerated in big structures by dry process, the determination of their total lengths was difficult; thus only the bundles lengths were reported. The presence of amino groups in the CN_x could be the reason to find less bundles in samples, due to their weaker van der Waals interactions, resulting in lower formation of bundles [8].

3.2. Raman and EDX Characterization of Pristine and Purified CN_x. Figure 3 shows the Raman spectra of pristine and purified CN_x plotted between 100 and 3000 cm^{-1}. The bands D (defect mode), G (graphite mode), and G′ (second order mode) situated at 1340, 1592, and 2686 cm^{-1}, respectively, are the typical peaks corresponding to carbonaceous materials. In the case of purified CN_x, the shifting to higher frequencies of G band suggests that nitrogen doping decreased. The I_D/I_G values were 1.1488 and 1.2815 for pristine and purified CN_x, respectively. This increasing in I_D/I_G ratio has been suggested as an evidence for sidewall functionalization of CNTs [18, 19].

With respect to chemical composition of our CN_x (pristine and purified), EDX analysis was carried out. Figures S1 and S2 (see Supplementary Material available online at http://dx.doi.org/10.1155/2015/801606) show the SEM images and their respective EDX graphs. The average quantity of iron in pristine samples was of 2.22 wt% (Figure S1), which decreased after purification process to 0.61 wt% (Figure S2), indicating the elimination of this contaminant (see Supplementary Material for the quantities of carbon, nitrogen, and oxygen elements).

3.3. Effect of Purified CN_x on Murine Fibroblasts Nonstressed and Stressed. 3T3 murine fibroblasts were used as a model for stromal cells, which can be found in matrix and connective tissue throughout the body. Figure 4 shows the kinetics of

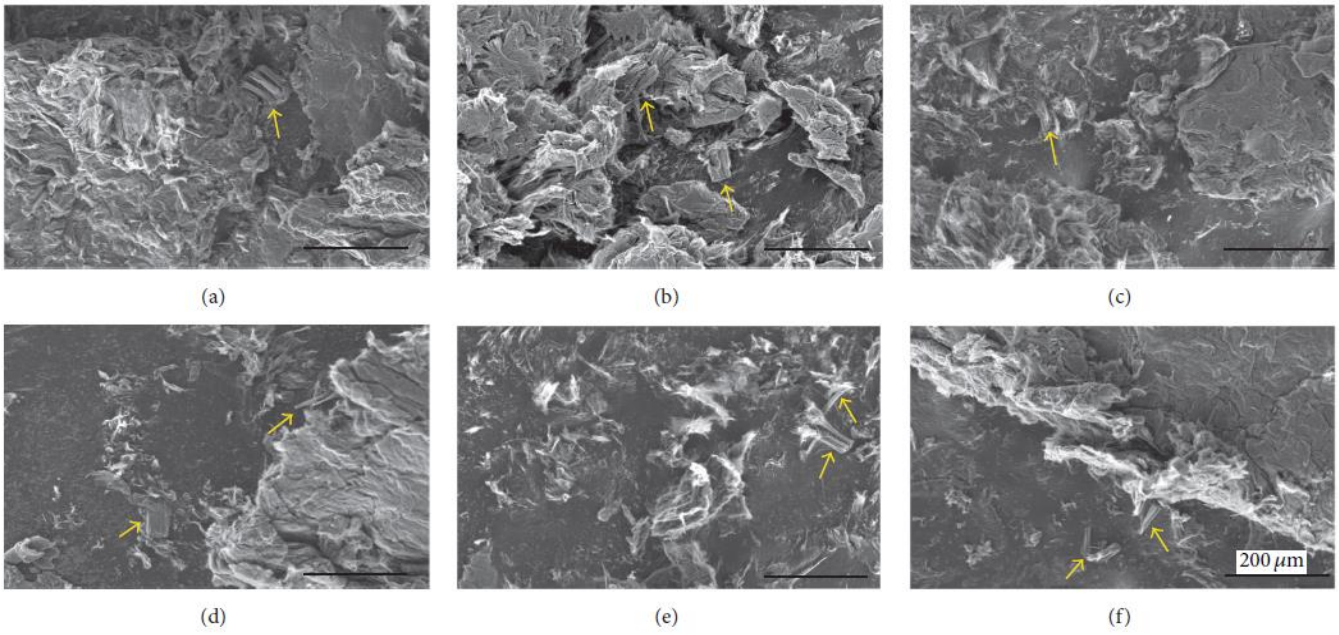

FIGURE 2: Representative SEM images of whole sample dry purified CN_x. (a–c) Different parts of sample from whole sample; (d–f) the same sample different fields. Yellow arrows pointed to bundles of purified CN_x. Big structures are agglomerates of CNTs which were easy to disperse in water.

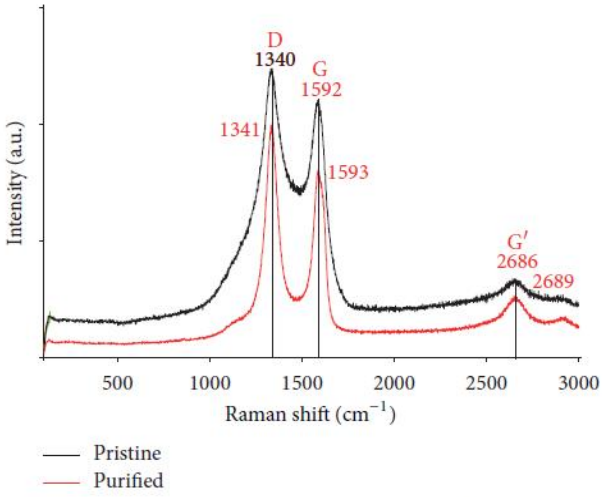

FIGURE 3: Raman spectra of pristine and purified CN_x at 633 nm.

fibroblasts growth with water-dispersed purified CN_x. When the cells were incubated simultaneously with the purified CN_x, the control culture (without purified CN_x) reached a maximum live cell concentration of $1.3 \times 10^5 \pm 3.4 \times 10^4$ cells per well at 96 h; meanwhile cultures with 7 μg/mL reached $2.6 \times 10^4 \pm 5.3 \times 10^3$ cells, and a drastic no cell survival was at 70 μg/mL of purified CN_x (Figure 4(a)). Purified CN_x added after 24 h of cell dissociation showed a decreased live cell, with a cell concentration of $9.6 \times 10^4 \pm 9 \times 10^3$ for 7 μg/mL and $5.5 \times 10^4 \pm 9.5 \times 10^3$ for 70 μg/mL, compared to control culture with $1.1 \times 10^6 \pm 1.5 \times 10^4$, at 96 h of exposure (Figure 4(b)). Results suggest that nanomaterials exhibited toxic effects, in concentration and exposure route-dependent manner. No effects concerning time exposure were observed.

Murine fibroblasts were susceptible to purified CN_x in concentration and exposure route-dependent manner. As previously mentioned, toxicity/biocompatibility of CNTs (SWCNT, MWCNT, and functionalized CNTs) on mammalian cells depends on different factors [6, 20, 21]. A lot of data research has shown the toxicity of CNTs [22–25] in human mesenchymal stem cells [26], 3T3 L1 fibroblasts [27], 3T3 fibroblast, telomerase, immortalized human bronchiolar epithelial cells, RAW 264.7 macrophages [6], mouse fibroblast cell L929, and mouse adipose-derived stem cells [3], but, to our knowledge, no experiments about the effects of CNTs have been reported on mammalian cells stressed by enzymatic detachment, which is a natural process in the body. Treatments with water-dispersed purified CN_x immediately added after cell liftoff (stressed cells by trypsin) were more toxic than purified CN_x added after 24 h of cell dissociation, suggesting that exposure route factor had negative effects on cell proliferation. This could have been caused by interaction of CNTs with residual fragments of adhesion proteins generated after cell trypsinization [12], which can still adversely affect cytoskeleton proteins that are involved in regulating cell adhesion, stability, and elasticity [14–16, 28]. However, in this work, only the cell proliferation was evaluated as a first approach to determine the purified CN_x toxicity; therefore, more studies are required and are currently underway.

Specific growth rate (μ) was calculated from exponential growth phase of fibroblasts and used as a parameter to evaluate the effect of purified CN_x on cell growth. In 7 μg/mL of dispersed-water purified CN_x incubated simultaneously with cells, μ was lower ($0.031 \pm 0.004\ h^{-1}$) than control cultivation

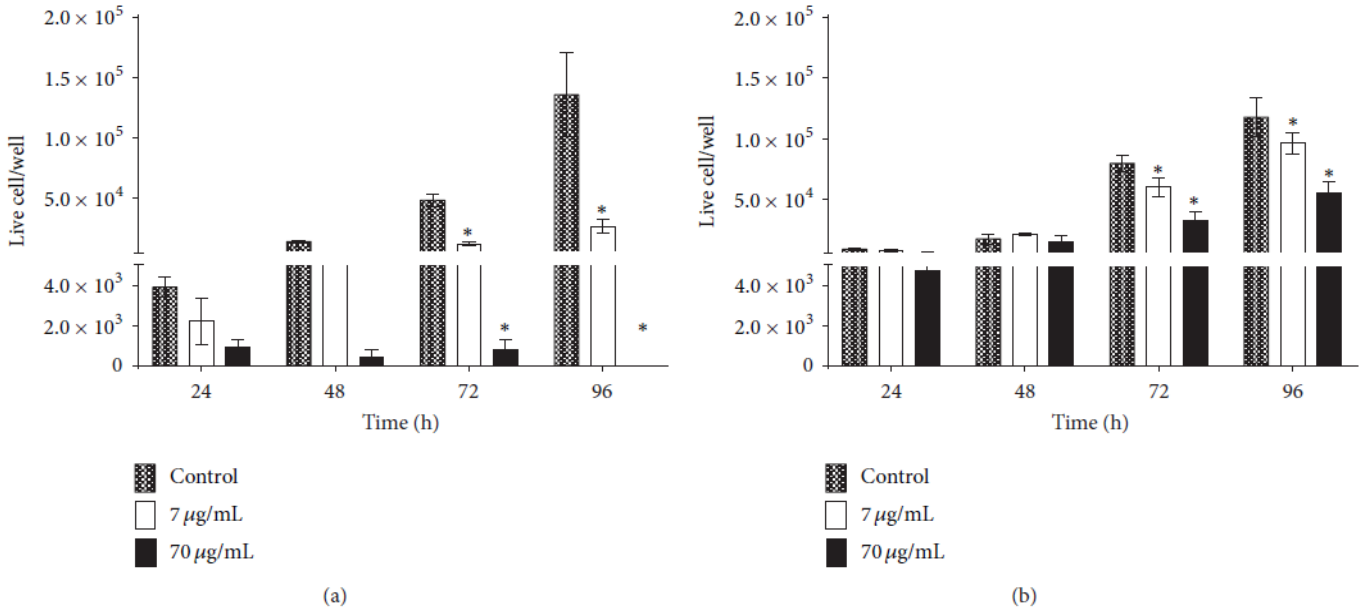

FIGURE 4: Effects of water-dispersed purified CN_x on NIH-3T3 murine fibroblast proliferation. Purified CN_x were incubated with fibroblast immediately after cell dissociation (a) or 24 h after cellular liftoff (b). Data are presented as mean ± SD. * indicates significant difference compared to untreated controls ($p < 0.05$); $n \geq 3$.

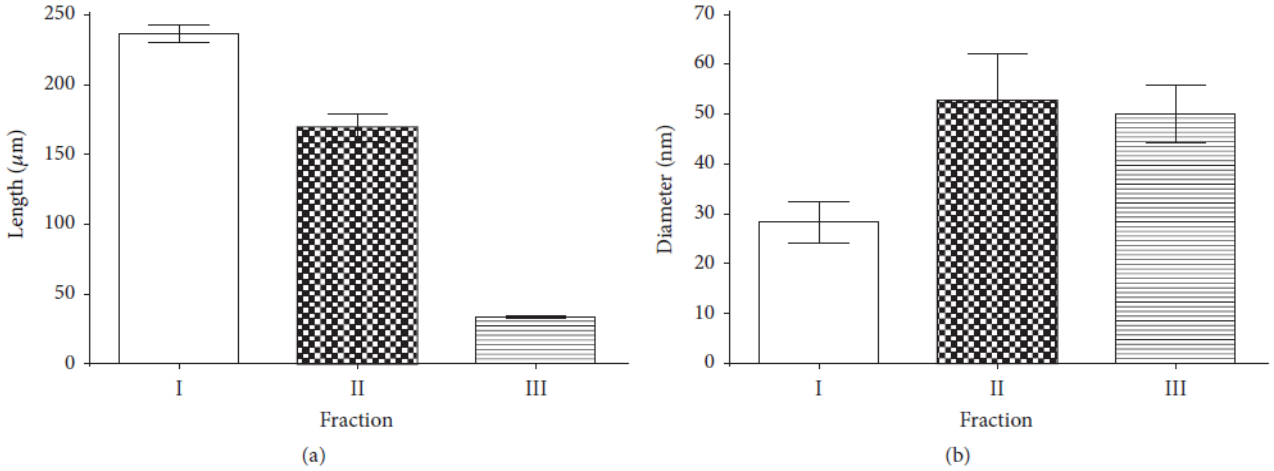

FIGURE 5: Variations in pristine CN_x length (a) and diameters (b) obtained from three different fractions of the same batch.

($0.048 \pm 0.004\ h^{-1}$); since no cells survived at 70 μg/mL, μ was not determined. Concerning incubation of cells with nanomaterials for 24 h after cell liftoff, values of μ were $0.044 \pm 0.002\ h^{-1}$ for control culture and $0.037 \pm 0.002\ h^{-1}$ and $0.035 \pm 0.001\ h^{-1}$ for purified CN_x at 7 and 70 μg/mL, respectively; both concentrations affected negatively μ. Results confirm a cytotoxic effect that is concentration and exposure route dependent.

3.4. Morphology Diversity of Pristine CN_x. In several investigations about cytotoxic effects of CNTs, these nanomaterials are purchased from companies, which are synthesized by CVD. However, researchers have reported different patterns in the bulk growth of CNTs during their synthesis, showing that the CVD method produces a wide range of CNTs morphologies with varieties of lengths and diameters [29]. In preliminary results, different fractions from the same batch were analyzed by SEM showing a wide collection of pristine CN_x sizes (Figure 5), with lengths of range between 30 and 250 μm (Figure 5(a)) and diameters of 24–60 nm (Figure 5(b)). Figure 6 shows a SEM micrograph gallery of the morphology of the different pristine CN_x fractions, where the variations in lengths (Figures 6(a)–6(c)) and diameters (Figures 6(d)–6(f)) among three fractions are clear. The morphology variation of CNTs could be the reason behind having contradictory results regarding cytotoxicity/biocompatibility of CNTs reported in several researches, and this issue should be studied in order to understand the relationship between CNTs and mammalian cell response.

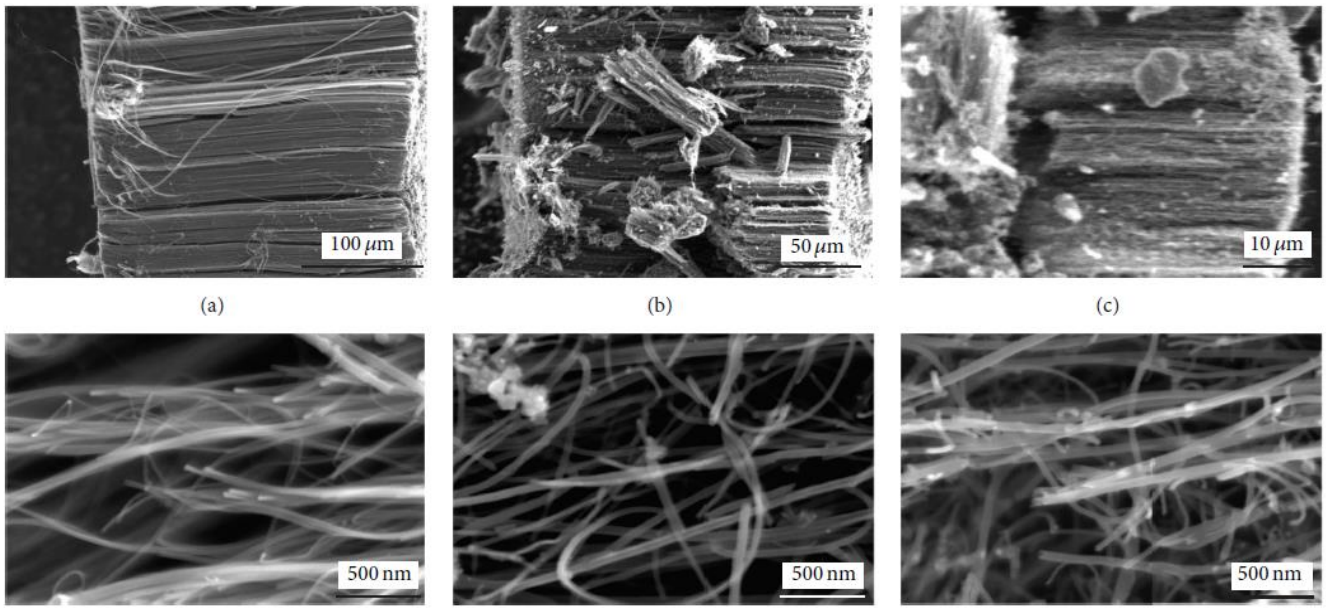

FIGURE 6: Electron micrograph gallery depicting the size diversity of pristine CN_x found in three different locations (fractions) from the quartz tube. Fractions: I (a, d), II (b, e), and III (c, f). Lengths (a–c) and diameters (d–f) of CN_x.

4. Conclusion

Finally, purified CN_x have a cytotoxicity effect that is directly dependent on their concentration; also purified CN_x showed a more toxic effect in enzymatic stressed cells than in the non-stressed ones. Since cells in the body are exposed to enzymatic processes of detachment, the present study of the effects on overstressed cells by enzymatic digestion is important for the development and potential uses of these nanomaterials in the biomedical field. On the other hand, chemical synthesis of pristine CN_x yields heterogenic product with substantial differences on length and diameter size, which have distinctive cytotoxic effects on the proliferation of NIH-3T3 cells. There is still a long path that we must take in order to understand the relationship between nanomaterials and mammalian cells. However, concentrations up to 7 μg/mL of nanotubes are well tolerated by the cells, and they could be used in biomedical applications.

Conflict of Interests

The authors declare that there is no conflict of interests regarding the publication of this paper.

Acknowledgments

The authors thank the Marcos Moshinsky Foundation and CONACYT-Mexico Grants 107082 (JFRM), CB-2013-220744 (EMS) for partial funding. J. Gil Munguía-López thanks CONACYT for its Scholarship 250279. They also thank L. Aldana for the English review and L. Ordoñez, B. A. Rivera-Escoto, and G. J. Labrada-Delgado for their technical assistance.

References

[1] S. Iijima, "Helical microtubules of graphitic carbon," *Nature*, vol. 354, no. 6348, pp. 56–58, 1991.

[2] H.-F. Cui, S. K. Vashist, K. Al-Rubeaan, J. H. T. Luong, and F.-S. Sheu, "Interfacing carbon nanotubes with living mammalian cells and cytotoxicity issues," *Chemical Research in Toxicology*, vol. 23, no. 7, pp. 1131–1147, 2010.

[3] M. L. Zhao, D. J. Li, L. Yuan, Y. C. Yue, H. Liu, and X. Sun, "Differences in cytocompatibility and hemocompatibility between carbon nanotubes and nitrogen-doped carbon nanotubes," *Carbon*, vol. 49, no. 9, pp. 3125–3133, 2011.

[4] X. Wang, T. Xia, M. C. Duch et al., "Pluronic F108 coating decreases the lung fibrosis potential of multiwall carbon nanotubes by reducing lysosomal injury," *Nano Letters*, vol. 12, no. 6, pp. 3050–3061, 2012.

[5] H. Haniu, N. Saito, Y. Matsuda et al., "Effect of dispersants of multi-walled carbon nanotubes on cellular uptake and biological responses," *International Journal of Nanomedicine*, vol. 6, pp. 3295–3307, 2011.

[6] S. K. Sohaebuddin, P. T. Thevenot, D. Baker, J. W. Eaton, and L. Tang, "Nanomaterial cytotoxicity is composition, size, and cell type dependent," *Particle and Fibre Toxicology*, vol. 7, article 22, 2010.

[7] A. Kunzmann, B. Andersson, T. Thurnherr, H. Krug, A. Scheynius, and B. Fadeel, "Toxicology of engineered nanomaterials: focus on biocompatibility, biodistribution and biodegradation," *Biochimica et Biophysica Acta (BBA)—General Subjects*, vol. 1810, no. 3, pp. 361–373, 2011.

[8] J. C. Carrero-Sánchez, A. L. Elías, R. Mancilla et al., "Biocompatibility and toxicological studies of carbon nanotubes doped with nitrogen," *Nano Letters*, vol. 6, no. 8, pp. 1609–1616, 2006.

[9] D. J. Li and L. F. Niu, "Influence of N atomic percentages on cell attachment for CNx coatings," *Bulletin of Materials Science*, vol. 26, no. 4, pp. 371–375, 2003.

[10] S. Boncel, K. H. Müller, J. N. Skepper, K. Z. Walczak, and K. K. K. Koziol, "Tunable chemistry and morphology of multi-wall carbon nanotubes as a route to non-toxic, theranostic systems," *Biomaterials*, vol. 32, no. 30, pp. 7677–7686, 2011.

[11] D. Li, L. Yuan, Y. Yang et al., "Adsorption and adhesion of blood proteins and fibroblasts on multi-wall carbon nanotubes," *Science in China, Series C: Life Sciences*, vol. 52, no. 5, pp. 479–482, 2009.

[12] X. Cai, R. Ramalingam, H. S. Wong et al., "Characterization of carbon nanotube protein corona by using quantitative proteomics," *Nanomedicine: Nanotechnology, Biology, and Medicine*, vol. 9, no. 5, pp. 583–593, 2013.

[13] R. J. McAnulty, "Fibroblasts and myofibroblasts: their source, function and role in disease," *International Journal of Biochemistry & Cell Biology*, vol. 39, no. 4, pp. 666–671, 2007.

[14] Q. Zheng, S. M. Iqbal, and Y. Wan, "Cell detachment: post-isolation challenges," *Biotechnology Advances*, vol. 31, no. 8, pp. 1664–1675, 2013.

[15] H. E. Canavan, X. Cheng, D. J. Graham, B. D. Ratner, and D. G. Castner, "Cell sheet detachment affects the extracellular matrix: a surface science study comparing thermal liftoff, enzymatic, and mechanical methods," *Journal of Biomedical Materials Research—Part A*, vol. 75, no. 1, pp. 1–13, 2005.

[16] H.-L. Huang, H.-W. Hsing, T.-C. Lai et al., "Trypsin-induced proteome alteration during cell subculture in mammalian cells," *Journal of Biomedical Science*, vol. 17, no. 1, article 36, 2010.

[17] J.-P. Kaiser, T. Buerki-Thurnherr, and P. Wick, "Influence of single walled carbon nanotubes at subtoxical concentrations on cell adhesion and other cell parameters of human epithelial cells," *Journal of King Saud University—Science*, vol. 25, no. 1, pp. 15–27, 2013.

[18] S. Lee, J.-W. Peng, and C.-H. Liu, "Raman study of carbon nanotube purification using atmospheric pressure plasma," *Carbon*, vol. 46, no. 15, pp. 2124–2132, 2008.

[19] S. Banerjee and S. S. Wong, "Rational sidewall functionalization and purification of single-walled carbon nanotubes by solution-phase ozonolysis," *The Journal of Physical Chemistry B*, vol. 106, no. 47, pp. 12144–12151, 2002.

[20] L. Meng, A. Jiang, R. Chen et al., "Inhibitory effects of multiwall carbon nanotubes with high iron impurity on viability and neuronal differentiation in cultured PC12 cells," *Toxicology*, vol. 313, no. 1, pp. 49–58, 2013.

[21] P. M. V. Raja, J. Connolley, G. P. Ganesan et al., "Impact of carbon nanotube exposure, dosage and aggregation on smooth muscle cells," *Toxicology Letters*, vol. 169, no. 1, pp. 51–63, 2007.

[22] C. L. Ursini, D. Cavallo, A. M. Fresegna et al., "Comparative cyto-genotoxicity assessment of functionalized and pristine multiwalled carbon nanotubes on human lung epithelial cells," *Toxicology in Vitro*, vol. 26, no. 6, pp. 831–840, 2012.

[23] M. Bottini, S. Bruckner, K. Nika et al., "Multi-walled carbon nanotubes induce T lymphocyte apoptosis," *Toxicology Letters*, vol. 160, no. 2, pp. 121–126, 2006.

[24] D. Liu, C. Yi, D. Zhang, J. Zhang, and M. Yang, "Inhibition of proliferation and differentiation of mesenchymal stem cells by carboxylated carbon nanotubes," *ACS Nano*, vol. 4, no. 4, pp. 2185–2195, 2010.

[25] F. A. Witzmann and N. A. Monteiro-Riviere, "Multi-walled carbon nanotube exposure alters protein expression in human keratinocytes," *Nanomedicine: Nanotechnology, Biology, and Medicine*, vol. 2, no. 3, pp. 158–168, 2006.

[26] E. Mooney, P. Dockery, U. Greiser, M. Murphy, and V. Barron, "Carbon nanotubes and mesenchymal stem cells: biocompatibility, proliferation and differentiation," *Nano Letters*, vol. 8, no. 8, pp. 2137–2143, 2008.

[27] J. Meng, M. Yang, L. Song et al., "Concentration control of carbon nanotubes in aqueous solution and its influence on the growth behavior of fibroblasts," *Colloids and Surfaces B: Biointerfaces*, vol. 71, no. 1, pp. 148–153, 2009.

[28] R. Umegaki, M. Kino-Oka, and M. Taya, "Assessment of cell detachment and growth potential of human keratinocyte based on observed changes in individual cell area during trypsinization," *Biochemical Engineering Journal*, vol. 17, no. 1, pp. 49–55, 2004.

[29] S. S. Meysami, F. Dillon, A. A. Koós, Z. Aslam, and N. Grobert, "Aerosol-assisted chemical vapour deposition synthesis of multi-wall carbon nanotubes: I. Mapping the reactor," *Carbon*, vol. 58, pp. 151–158, 2013.

Effect of graphene oxide on bacteria and peripheral blood mononuclear cells

Jessica Campos-Delgado, Kelly L.S. Castro, Jose G. Munguia-Lopez, Ana K. González, Martin E. Mendoza, Benjamin Fragneaud, Raphael Verdan, Joyce R. Araujo, Francisco J. González, Hugo Navarro-Contreras, Ivan N. Pérez-Maldonado, Antonio de León-Rodríguez, Carlos A. Achete

Journal of Applied Biomaterials & Functional Materials (Open Access)

2016; 14(4): e423 - e430

For access to full document, please type the following link:

DOI:10.5301/jabfm.5000325

JABFM
eISSN 2280-8000

J Appl Biomater Funct Mater 2016; 14(4): e423-e430
DOI: 10.5301/jabfm.5000325

ORIGINAL RESEARCH ARTICLE

Open Access

Effect of graphene oxide on bacteria and peripheral blood mononuclear cells

Jessica Campos-Delgado[1], Kelly L.S. Castro[2], Jose G. Munguia-Lopez[3], Ana K. González[1], Martin E. Mendoza[2], Benjamin Fragneaud[4], Raphael Verdan[2], Joyce R. Araujo[2], Francisco J. González[1], Hugo Navarro-Contreras[1], Ivan N. Pérez-Maldonado[1], Antonio de León-Rodríguez[3], Carlos A. Achete[2]

[1] CIACYT, Universidad Autónoma de San Luis Potosí, San Luis Potosí - México
[2] DIMAT, INMETRO, Xerem, Rio de Janeiro - Brazil
[3] Department of Molecular Biology, IPICYT, San Luis Potosí - México
[4] Departamento de Física, UFJF, Juiz de Fora - Brazil

ABSTRACT

Background: Driven by the potential biological applications of graphene, many groups have studied the response of cells exposed to graphene oxide (GO). In particular, investigations of bacteria indicate that there are 2 crucial parameters, which so far have only been investigated separately: GO size and exposure methodology. Our study took into account both parameters. We carefully characterized the samples to catalog sizes and structural properties, and tested different exposure methodologies: exposure in saline solution and in the presence of growth media. Furthermore, we performed experiments with peripheral blood mononuclear cells exposed to our GO materials.

Methods: Atomic force microscopy, scanning electron microscopy, Raman spectroscopy, X-ray photoelectron spectroscopy and transmission electron microscopy were used to characterize the morphology and composition of different samples of GO: GO-H_2O, GO-PBS and GO-MG. Our samples had 2D sizes of ~100 nm (GO-H_2O and GO-PBS) and >2 µm (GO-MG). We tested antibacterial activity and cytotoxicity toward peripheral blood mononuclear cells of 3 different GO samples.

Results: A size-dependent growth inhibition of *Escherichia coli* (DH5 α) in suspension was found, which proved that this effect depends strongly on the protocol followed for exposure. Hemocompatibility was confirmed by exposing peripheral blood mononuclear cells to materials for 24 hours; viability and apoptosis tests were also carried out.

Conclusions: Our experiments provide vital information for future applications of GO in suspension. If its antibacterial properties are to be potentiated, care should be taken to select 2D sizes in the micrometer range, and exposure should not be carried out in the presence of grow media.

Keywords: Antibacterial effect, *Escherichia coli*, Graphene oxide, Peripheral blood mononuclear cells

Introduction

The attention that graphene has attracted since its isolation in 2004 is undeniable (1). Over the years, an increasing number of scientific groups have been seduced by its amazing electronic, mechanical, optical and thermal properties, and evidently, by its innumerable potential applications (2). However, due to the hydrophobic nature of pristine graphene, in biomedicine, graphene oxide (GO) is considered a better alternative thanks to its hydrophilicity, amphiphilicity and availability of functional groups attached to its surface or edges (3). Along with the debut of graphene and GO in biological applications has come the necessity of studying their biocompatibility (4-13). Of particular interest have been the reported antibacterial properties of GO (5, 7-11, 14). Akhavan and Ghaderi (7) argued that the adverse effect of graphene on bacteria is to be attributed to membrane damage by the numerous sharp edges of GO, while others have focused on oxidative stress as the toxic mechanism (8). A recent paper by Mangadlao and coauthors (15) reported on the fabrication of GO films through the Langmuir-Blodgett technique, where graphene sheets lie flat on a polyethylene terephthalate (PET) substrate. Thus the sharp edges of GO were not available to pierce the membranes, and yet antibacterial activity was still observed, suggesting that the antibacterial activity of GO does not rely on membrane damage by its sharp edges. Liu and coauthors (14) conducted experiments that showed that

Accepted: July 4, 2016
Published online: September 7, 2016

Corresponding author:
Dr. Jessica Campos-Delgado
Arquitectos 135
Col. Himno Nacional
CP 78280
San Luis Potosí, SLP, México
jessica.mex@gmail.com

the antibacterial effect of GO depends on the sheet size, suggesting that large graphene sheets wrap bacteria and block interactions, isolating them from the environment, while small sheets interact with bacterial surfaces in a nonharmful way. These results confirmed the encapsulation by graphene reported previously by another group in 2011 (16). Many groups have studied the response of bacteria exposed to GO, and although many researchers have agreed on its antibacterial effect (5, 7, 8, 11, 13), a couple of research groups have reported a contrary effect (9, 10). Ruiz et al (9) confirmed a GO enhancement effect on *Escherichia coli* proliferation, and Das et al (10) confirmed the kinetic growth of *Pseudomonas aeruginosa* and *E. coli* in the presence of GO. These early controversial reports have led to more investigations into the subject. Recently, Hui and coworkers (17) conducted experiments where they demonstrated that the discrepancies regarding the antibacterial effects of GO lie in the way that GO is exposed to the bacteria. When bacteria is exposed to GO in pure saline solution, the antibacterial effect is observed; however, this antibacterial activity decreases progressively when increasing amounts of Luria-Bertani (LB) broth are added to the saline solution. They attribute this decrease of bactericidal activity to the absorption of LB molecules on the surface of the graphene; hence, the more the graphene surface is free from adsorbates, the greater the antibacterial effect it will have. Although this piece of research is very valuable and clarifies the controversial results above discussed, it lacks important information about the characterization of the GO used and does not take into account the size-dependent antibacterial effect reported by Liu and coauthors (14). Moreover, an inspection of the GO materials shown on their figures demonstrates a size-heterogeneous sample.

As described above, different groups have attempted to study the antibacterial effect of graphene and have found 2 major influential parameters: size and exposure methodology. Our study brought together both approaches. We carefully characterized the samples to catalog the sizes and structural properties and tested different exposure methodologies: exposure in saline solution and exposure in the presence of growth media. Our results indicated that the antibacterial effect was not only size dependent but also depended on the exposure technique.

When it comes to cytotoxicity toward mammalian cells, the picture is not any more uniform (4, 12, 13, 18-25). Some groups have reported on the biocompatibility of graphene (4, 13, 18, 21-23, 25), while others have discussed its toxicity in terms of concentration and degree of oxidation (12, 19, 20, 26). The same dilemma applies to its hemocompatibility (12, 22, 27, 28). In any case, many authors who have written reviews on this topic (23-25, 29, 30) have agreed on the need to standardize protocols for the evaluation of cytotoxicity, because many studies are not comparable due to differences in synthesis and processing methods of GO which yield a wide spectrum of physicochemical properties. Sheet size, surface functionalization, degree of oxidation, purity and defects are some of the parameters of GO that vary from one report to the other, rendering it very difficult to draw conclusions from the available literature.

We carried out atomic force microscopy (AFM), scanning and transmission electron microscopy (SEM and TEM), Raman spectroscopy and X-ray photoelectron spectroscopy (XPS) to study the morphology and structure of different GO materials. We also performed an exhaustive series of experiments to test the effects of our GO samples on bacteria and mammalian cells. We produced graphite oxide (GtO) from expanded graphite using the modified Hummers' method, followed by a purification process (see "Materials and methods" and "Supplementary material", available online at www.jab-fm.com). Using this GtO, we obtained 3 different materials: GO dispersed in water for 6 hours in an ultrasonic bath (GO-H_2O), GO dispersed in phosphate-buffered saline (PBS) for 6 hours in an ultrasonic bath (GO-PBS) and GO manually ground and dispersed in water (GO-MG). We confirmed that the antibacterial effect of GO is size dependent and proved that the protocol for exposure plays a crucial role. Our experiments with peripheral blood mononuclear cells (PBMCs) confirmed the hemocompatibility of our different GO materials for the exposure protocol used.

Materials and Methods

GO preparation

We obtained graphite oxide from expanded graphite (from Nacional de Grafite, Brasil) using the modified Hummers' method, followed by a purification process. We dispersed graphite oxide in H_2O or PBS by sonication (ultrasonic bath) for 6 hours, thus obtaining GO-H_2O and GO-PBS, respectively. The sample GO-MG was obtained by manually grinding graphite oxide using a mortar (for further details, see "Supplementary material").

Raman spectroscopy

Raman spectroscopy analyses were carried out on a Witec Alfa 300 spectrometer, with a 532 - nm laser line in backscattering configuration using a microscope with a ×50 objective. The laser power was kept under 0.1 mW to avoid local heat damage to samples. All spectra were acquired with 10 accumulations of 10 seconds of integration time in the region between 100 cm^{-1} and 3,600 cm^{-1}.

Atomic force microscopy

To carry out AFM imaging of the different GO samples, we deposited a diluted solution of each GO on a Si/SiO_2 wafer by drop casting. The drop was carefully rolled over the wafer to uniformly disperse single layers and a few layers of GO. Finally, the excess of solution was blown off with nitrogen (N_2). The samples were dried in ambient conditions for 24 hours. The AFM images were obtained in intermittent contact mode with a JPK Nanowizard 3 using a silicon nitride tip (spring constant of 40 N/m).

Transmission electron microscopy

Dispersed solutions of the different GO materials were used to deposit them on Cu^- holey carbon grids (300 mesh). A probe-corrected FEI Titan 80-300 microscope was used at 80 kV to minimize beam damage effects. Conventional bright

field images and high resolution transmission electron microscopy (HRTEM) images were taken. Electron energy loss spectroscopy (EELS) measurements were done in spectroscopy mode (STEM-EELS) using a GIF 866 camera under the following experimental conditions: α = 58.5 mrad, GIF aperture = 2.5 mrad, dispersion = 0.02 eV/ch with ZLP_{FWHM} resolution of 0.8 eV.

Scanning electron microscopy

The GO solutions were diluted to a concentration of 5 µg/mL using deionized water. One drop of each solution was deposited on a 300-nm SiO_2/Si substrate kept at 50°C on a hot plate and allowed to dry. SEM images were obtained at 15 kV and 50 pA, with secondary electron detection using the Through Lens Detector (TLD-detector) in FEI Helios Nanolab 650.

X-ray photoelectron spectroscopy

XPS analyses were performed in an ultrahigh vacuum medium (pressure of 10^{-9} mbar) using an Mg, Kα (hν = 1,253.6 eV) X-ray source, with power given by emission of 20 mA, at a voltage of 15 kV. For the carbon element, the high-resolution spectra were obtained with analyzer pass energy of 20 eV in steps of 0.05 eV. The binding energies were referred to the carbon 1s level of a neat graphite sample, set as 284.8 eV.

Cell contact to GO

In the literature, many groups have tested the antibacterial activity of GO. Although the early reports were contradictory, a recent study attempted to elucidate the nature of these controversial effects (17). The authors state that the observed antibacterial effect is directly related to the availability of graphene's basal planes, and they further affirm that when GO is exposed to bacteria, its effect is determined by the media in which the 3-hour exposure takes place. If the exposure is carried out in a saline solution, then GO will have an antibacterial effect; when this exposure is carried out in LB broth growth medium, no antibacterial effect was evidenced.

Having these results in mind and to avoid masking antibacterial effects by the medium components, we decided to test the effect our GO-H_2O material for the growth of the gram-negative bacteria *E. coli* (DH5 α), probing 3 different exposure times: 0, 1 and 3 hours in saline solution. Briefly, the experiment consisted of growing *E. coli* at 37°C overnight. Then the culture was changed with fresh medium and allowed to grow again to the exponential phase. *E. coli* at 10^7 colony forming units/mL was resuspended in saline solution (0.9% NaCl) and incubated to a final concentration of 200 µg/mL of GO-H_2O for 1 and 3 hours at 37°C and under agitation. As control, we used samples exposed to Milli-Q grade water. After this step (referred to as exposure), cells along with the materials were harvested by centrifugation, resuspended in 60 mL of fresh medium and incubated at 37°C under agitation (the recovery step) for 500 minutes. For the 0-hour-exposure experiments, the cells were put in contact with the material and immediately allowed to undergo the recovery step (for more details, see "Supplementary material"). After 500 minutes, the optical density at 600 nm (OD_{600}) of the cell cultures was measured, readings were recorded 3 times and all experiments were performed in triplicate.

We tested our materials on mammalian cells by exposing PBMCs to different concentrations of GO-H_2O, GO-PBS and GO-MG, and performed cell viability and apoptosis tests after 24 hours. PBMCs were isolated from the blood of healthy individuals, and a protocol was followed for the separation of PBMCs based on density gradient centrifugation (for further details, see "Supplementary material"). Then the cells were exposed to our materials at concentrations of 2, 20 and 200 µg/mL on multiwell culture plates for 24 hours, including a positive and a negative control. The negative control consisted of only medium and cells, and positive control was 0.3% H_2O_2. We performed trypan blue cell viability tests counting live/dead cells using a hemocytometer.

Results

Sample characterization

We thoroughly studied the physical and chemical properties of our GO materials. AFM, SEM and TEM were used to figure out the morphological characteristics of the different samples, and EELS and XPS to understand their chemistry. Our studies revealed that the GO-H_2O sample contained small fragments of GO with average 2D sizes of 100 nm and thicknesses of 1 or 2 layers (Fig. 1A, D and G; see also "Supplementary material" for more details). The sample GO-PBS was very similar in morphology to GO-H_2O, as can be confirmed in Figure 1B and E. This was not a surprise since both samples were subjected to the same preparation treatment (6 hours in ultrasonic bath); however, the difference between the samples lay in the medium of dispersion (i.e., for GO-PBS, PBS was used). This difference resulted in many PBS residues that accompanied the GO sheets. Figure 1H shows a TEM image of GO-PBS where an impurity can be seen. Furthermore, Figure S2 (available online as supplementary material at www.jab-fm.com) shows an SEM image where the impurities are clearly localized on top of the GO, and our XPS analysis revealed signals from Na, Cl, K and P that evidently came from PBS residues.

Sample GO-MG showed very different characteristics. Figure 1C, f and i reveal that GO-MG contained larger-area GO sheets, averaging several microns, showing similar morphological characteristics to those of exfoliated graphene. Nevertheless, structural damage in the honeycomb structure was detected.

Our XPS analysis of the C binding energies confirmed the presence of sp^2 (C = C) at 283.9 eV and carbon atoms out of regular sp^2 configurations (C-C/C-H) at 284.8 eV as expected for GO (31). Beyond that, other oxygenated carbon functional groups were observed, such as phenol or epoxide (C-OH/C-O-C) between 285.8-286.3 eV, carbonyl groups (C = O) at 287.1 eV, carboxyl groups (COOH) at 288.7 eV and the π-π* shake-up satellite at approximately 291.0 eV typical of aromatic delocalized electrons (32). Figure 2A, B shows XPS spectra of GO-H_2O and GO-MG, respectively. It is clear that although the nature of the bonds present in both samples is the same, their distribution is different. This was expected, as both samples

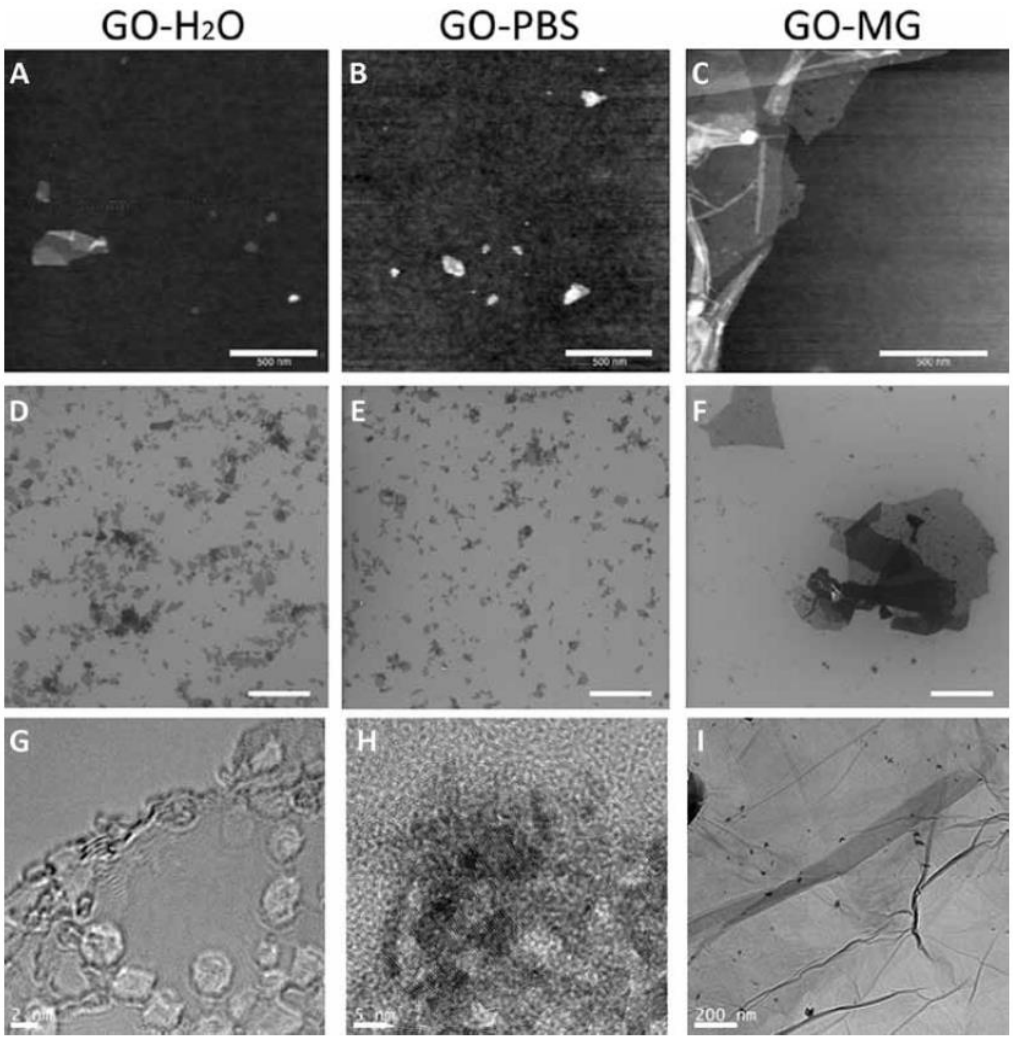

Fig. 1 - Representative atomic force microscopy (AFM) (**A-C**), scanning electron microscopy (SEM) (**D-F**) and transmission electron microscopy (TEM) (**G-I**) micrographs of graphene oxide (GO) samples: (**A, D, G**) GO-H_2O; (**B, E, H**) GO–phosphate-buffered saline (GO-PBS); (**C, F, I**) GO manually ground and dispersed in water (GO-MG). Scale bars represent 500 nm in (**A-C**); 1 µm in (**D-F**); and 2 nm, 5 nm and 200 nm in (**G**), (**H**) and (**I**), respectively.

were derived from GtO and dispersed in water; however, the preparation method led to more sp^2 hybridization in the GO-H_2O sample (18% against 9% in GO-MG; as confirmed by EELS results in Fig. S3, available online as supplementary material at www.jab-fm.com). On the other hand, the oxidized functional groups also showed differences in composition: the most intense component for GO-H_2O were the carbonyl groups (C = O) (25%) (see Suppl Tab. I for information on the EELS analysis, available online as supplementary material at www.jab-fm.com), which were preferentially located on the edges of graphene sheets, while for GO-MG, the most intense component was the third component, C-OH/C-O-C (25%), as shown in Supplemental Table I, typically located on the basal plane of graphene (33).

As mentioned above, the XPS analysis of the GO-PBS sample revealed the presence of elements other than C and O, which were due to the diluent.

Representative Raman spectroscopy results are included in Figure 2C. Bulk measurements of the GO materials revealed the strong presence of the D and G bands, located at ~1,350 cm^{-1} and ~1,590 cm^{-1}, respectively. All spectra shared intense D bands and sharp G bands. We attribute such an intense defect-related band (D band) to the presence of sp^3 hybridization and to the high amount of oxygen bonds which were perforce present on GO. However, the I_D/I_G ratio of the GO-PBS sample was the highest (1.1 compared with 0.97 for both GO-H_2O and GO-MG) probably due to the presence PBS residues, as confirmed by TEM and SEM. From a simple inspection, it is quite obvious that the spectra of the 3 different GO samples are rather similar. For samples GO-H_2O and GO-PBS, this is expected, since the morphology of the samples is comparable (see Fig. 1); however, although sample GO-MG possesses very different characteristics, its Raman spectrum also looks similar. This suggests a high level of defects due to the less regular sp^2 carbon structure, as detected by XPS and EELS. It is possible that the high D band is due to the symmetry breakpoints that arise from in-plane defects (see Fig. 1C), high proportion of sp^3 hybridization, OH-terminated edges and C-O bonds present in the sample.

From our characterization, we can conclude that GO-H_2O and GO-PBS share morphology features (~100 nm, 1-2 layers, amount of defects), while GO-MG presents larger areas but the same average amount of defects. Regarding surface

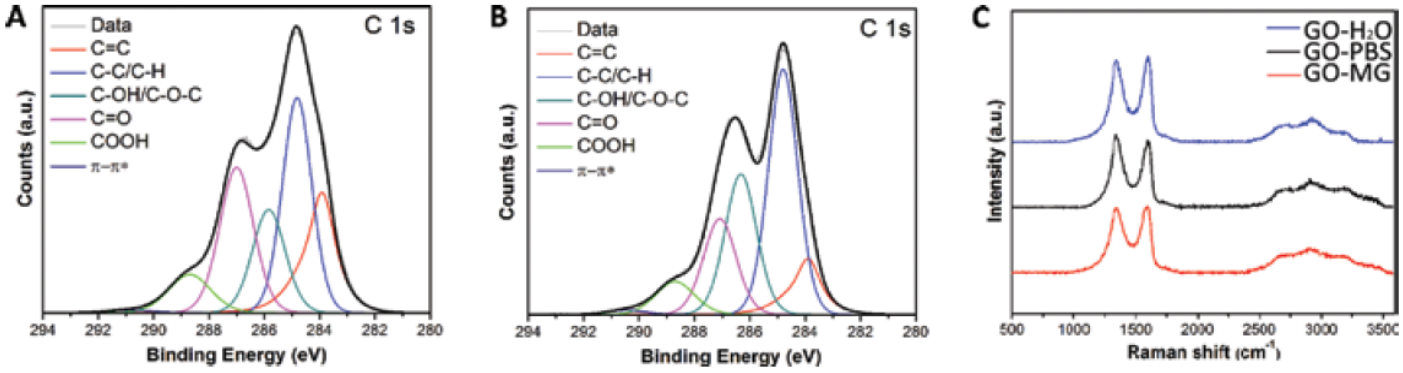

Fig. 2 - (**A, B**) X-ray photoelectron spectroscopy (XPS) spectra of graphene oxide (GO)-H_2O and GO manually ground and dispersed in water (GO-MG), respectively; (**C**) Raman spectra of the GO materials.

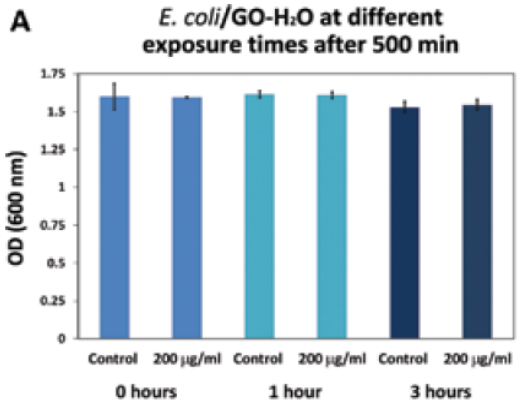

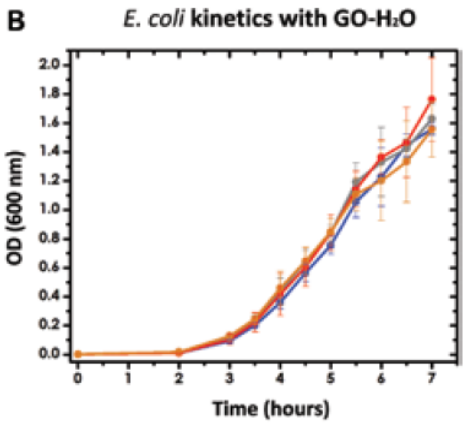

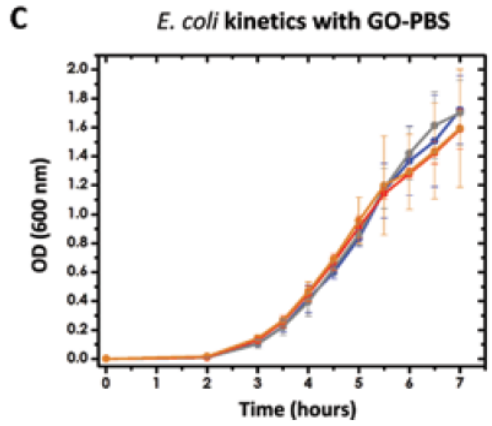

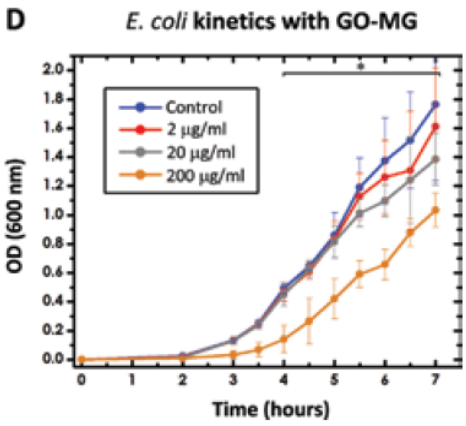

Fig. 3 - (**A**) *E. coli* exposed to graphene oxide (GO)-H_2O at different times (0, 1 and 3 hours) and incubated for 500 minutes in fresh Luria-Bertani medium for a recovery process; (**B-D**) growth kinetics of *E. coli* exposed for 1 hour to different concentrations of GO-H_2O, GO–phosphate-buffered saline (GO-PBS), GO manually ground and dispersed in water (GO-MG), respectively. Inset in (**D**) contains the color codes assigned to the different concentrations used in the study, which apply to graphs (**B-D**). Experiments were performed in triplicate, error bars stand for the standard deviation of the recorded values. OD = optical density; *p<0.05, n = 3.

chemistry, it can be concluded that all samples present a significant amount of sp^3 hybridization and oxygen species.

Biocompatibility tests

Figure 3 shows the growth of *E. coli* in the presence of GO. Our results showed that the presence of GO-H_2O at such a high concentration did not have a negative impact on bacterial cell growth (Fig. 3A). For the 3 exposure times, the OD values of the cultures with GO-H_2O were quite similar to those of controls, suggesting that the amount of living cells did not decrease in contact with GO-H_2O. It is worth mentioning the slight decrease in OD_{600} values for the 3-hour exposure set; both samples (control and GO-H_2O) showed lower values compared with those of the 0-hour and 1-hour exposure sets. We attribute this to a uniform decrease in the amount of living cells after 3 hours of agitation and the decrease of specific growth rate (μ) due to the lack of nutrients in the saline media. To avoid this effect, we chose to perform exposures of 1 hour for our growth kinetic experiments.

To assess the effect of our different GO materials (GO-H_2O, GO-PBS and GO-MG), we performed a 7-hour kinetic

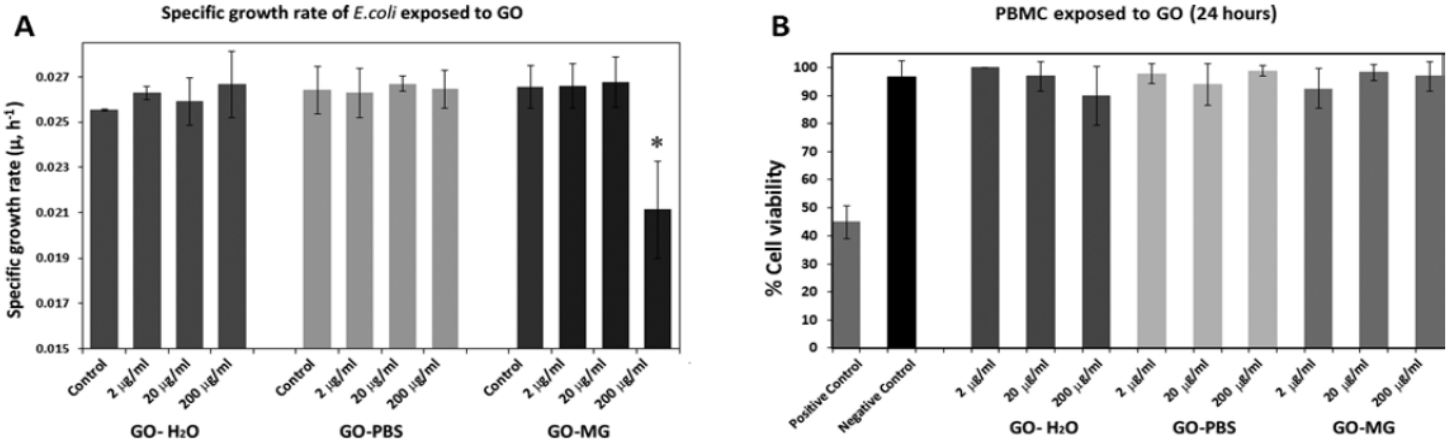

Fig. 4 - (**A**) Specific growth rate of *E. coli* in contact with graphene oxide (GO) materials, calculated from the 7-hour growth kinetic study. *p<0.05, n = 3; (**B**) viability of peripheral blood mononuclear cells exposed to GO materials after 24 hours.

study of the growth of *E. coli*, with an exposure to the materials of 1 hour. We tested 3 different concentrations: 2, 20 and 200 µg/mL for each material. Conditions were similar to those in the above-described experiment (see the section "Cell contact to GO") except that during the recovery step, systematic OD_{600} readings were recorded from the cultures (see more details in "Supplementary material").

Figure 3B, C and D shows the results of our kinetic study of *E. coli* exposed to GO-H_2O, GO-PBS and GO-MG, respectively. From our above-described results. We did not expect to find an antibacterial effect of the GO-H_2O material, and such a conclusion was confirmed by Figure 3B which shows that the 3 concentrations of GO-H_2O tested had no adverse effect on the growth of *E. coli*. Our characterization showed that the morphology of the GO-PBS sample was quite similar to that of GO-H_2O. Thus no antibacterial effect was expected from this sample either. Figure 3C confirms that the presence of GO-PBS at concentrations of 2, 20 and 200 µg/mL did not interfere with the growth of *E. coli*.

Our characterization evidenced the marked differences in morphology that the GO-MG sample presented when compared with GO-H_2O (see Fig. 1). Such differences proved to have a strong impact on the growth of *E. coli* at the highest tested concentration (200 µg/mL). The results of our kinetic study (Fig. 3D) revealed that low doses of GO-MG (2 and 20 µg/mL) do not show any effect on the growth of *E. coli*; however, a higher concentration (200 µg/mL) proved to have an adverse effect on the growth, where µ decreased to a value of 0.021 h^{-1} (±0.002) compared with 0.0265 h^{-1} (±0.0009) for the control (Fig. 4A).

We performed 1- and 2-way ANOVA with Dunnett's post test to compare the different concentrations used against the control. Values of $p < 0.05$ were considered as significant.

We conclude that the sample GO-MG at high concentration shows an antibacterial effect which is the product of the high amount of large-area sheets that wrap around the bacteria, isolating them and disabling their proliferation, in good agreement with the reports of Liu et al (14) and Hui et al (17).

Our study revealed as well that the GO-MG antibacterial effect evidenced here was the product of the interactions with GO during the exposure step, and such an effect was not masked by the presence of LB growth medium during the recovery phase. Furthermore, the absence of this exposure step in saline solution (0-hour exposure) led to a complete suppression of the antibacterial effect of GO-MG (see Suppl Fig. 5, available online as supplementary material at www.jab-fm.com, for results for GO-MG exposed to bacteria), suggesting an adsorption of LB on the surface of the graphene and an inability of the sheets to wrap and isolate *E. coli* – in good agreement with the conclusions drawn by the group of Hui et al (17).

Cytotoxicity to PBMCs

Results for the test of cell viability are shown on Figure 4B, indicating that the presence of GO materials did not have a negative effect on the viability of cells at 24 hours of exposure. The lowest viability identified was for the GO-H_2O sample at the highest concentration tested (200 µg/mL) with a value of 89.95% ± 10.55%. For the rest of the samples, viability was above 90%, proving good hemocompatibility, which is in agreement with previous reports on the subject (22, 27).

Apoptosis tests were conducted on PBMCs exposed to our materials for 24 hours at concentrations of 2 and 20 µg/mL (see details on "Supplementary material").

We evaluated whether our materials induced apoptosis of PBMCs, by flow cytometry using annexin V/propidium iodide markers. Representative dot plots of the apoptosis assay are shown in Figure 5A-E. Interestingly, for all of the materials for both concentrations tested, the percentage of apoptotic cells was very close to that of the negative control (Fig. 5F). In addition, we did not find any increase in necrotic cells when our materials were present, as revealed by the propidium iodide marker, and no early apoptosis was detected, which was revealed when only the annexin marker was used.

It is important to point out that the 24-hour exposure of GO samples to PBMCs described above was done in the presence of RPMI-1640 medium with L-glutamine, 10% fetal bovine serum (FBS) and 1% penicillin-streptomycin (see

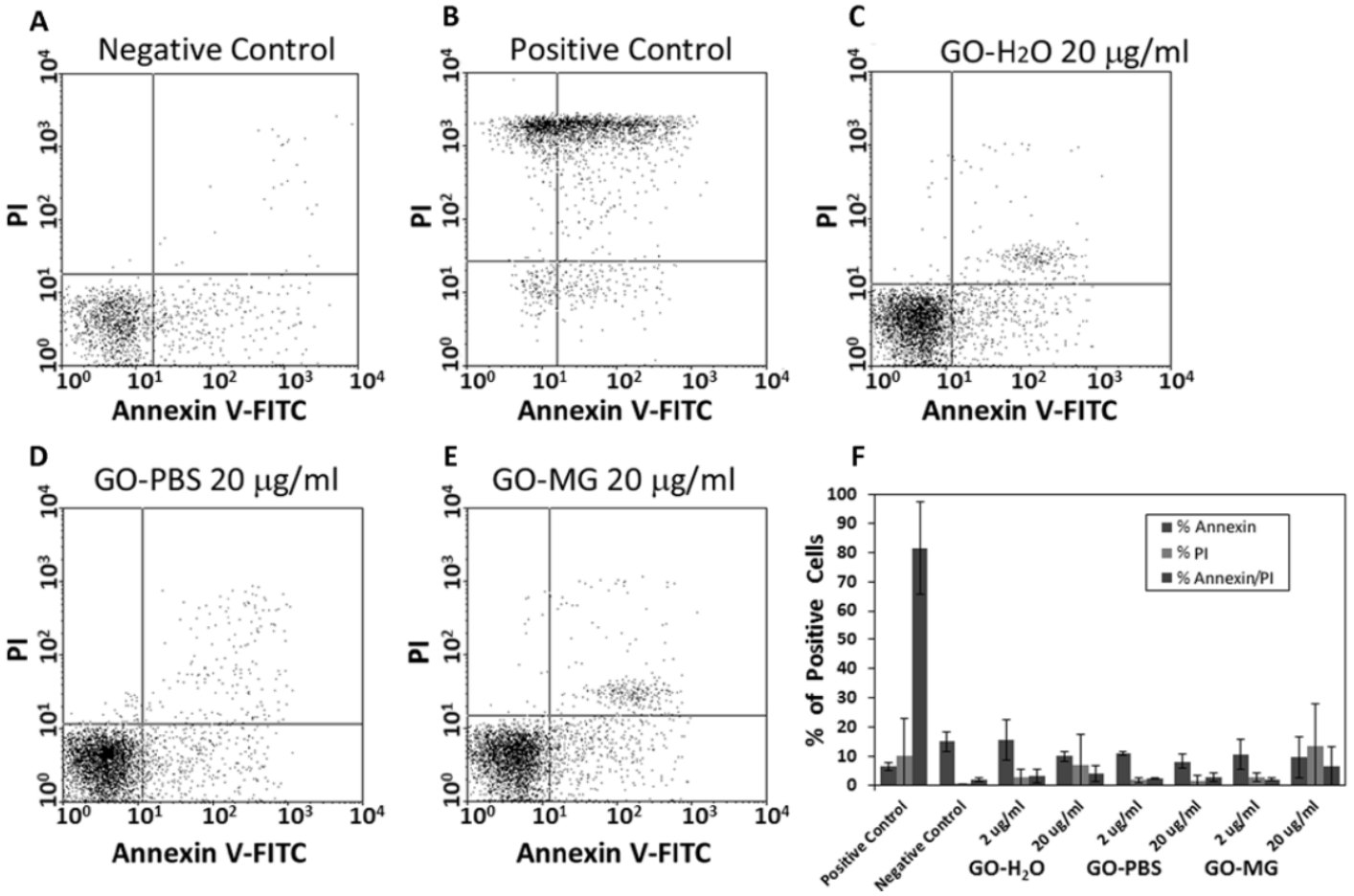

Fig. 5 - Results of the annexin V-FITC and propidium iodide (PI) assay. Representative scatter diagrams of peripheral blood mononuclear cells (PBMCs): (**A**) negative control, (**B**) positive control, (**C-E**) exposed to 20 µg/mL of graphene oxide (GO)-H_2O, GO–phosphate-buffered saline (GO-PBS) and GO manually ground and dispersed in water (GO-MG), respectively; (**F**) summary of the percentage of positive cells for annexin, PI and annexin/PI.

"Supplementary material"). The availability of nutrient molecules from the growth medium opens the possibility of absorption of proteins into the GO basal plane masking thus its toxic effect. To investigate this possibility, new sets of experiments are being designed and performed, in which exposure of GO samples to PBMCs is carried out in the absence of nutrient molecules, as in the case of bacteria.

Discussion

We performed a complete characterization of 3 different GO samples and tested their toxicity to bacteria and PBMCs. GO-H_2O and GO-PBS were obtained by the same preparation method from GtO; a 6-hour sonication treatment produced GO dispersed in water (GO-H_2O) and in PBS (GO-PBS). These samples had 2D dimensions of ~100 nm, consisted of 1-2 staked layers, had sp^3 hybridization and were bonded to oxygen species. GO-MG was derived from GtO by manual grinding and dispersed in water. This preparation led to a material of 1-2 layers with 2D dimensions of several microns possessing many in-plane defects, along with sp^3 hybridization and reactive oxygen species. Our experiments in suspension proved that GO-H_2O and GO-PBS did not show an antibacterial effect to *E. coli*, while the presence of 200 µg/mL of GO-MG decreased its specific growth rate. It is thus evident that not every type of GO will present antibacterial activity; this effect is size-dependent, and small sheets do not interfere with bacteria growth, while large sheets (several microns) tend to inhibit it. We proved as well that the protocol followed for exposure of GO-MG to bacteria was vital for the outcome. While direct exposure of bacteria to all concentrations of GO-MG in LB media did not show an adverse effect; if the first contact was carried out in saline solution for 1-3 hours, then the presence of GO-MG at 200 µg/mL would decrease the specific growth rate of *E. coli*. This observation is in accordance with the results of Hui et al (17) and explains previous contradictory results on the toxicity of GO to bacteria due to protocol discrepancies. Experiments with PBMCs exposed to our GO materials indicated that no adverse effect was observed after 24 hours, in good agreement with previous studies; however, further studies are underway to account for the effect in the absence of nutrient molecules that could be absorbed on the basal planes of GO (22, 27). For

the applications of GO in biology, and in particular, if its antibacterial properties are to be potentiated, it is thus very important to perform a characterization of the material, giving special attention to its dimensions and homogeneity, as well as to the protocol for exposure.

Acknowledgement

We thank B. Archanjo, M. Pojucan, M. Gutiérrez-Hernández and E. H. Ferreira for technical assistance.

Disclosures

Financial support: J.C.-D. is thankful to CONACYT for funding.
Conflict of interest: None of the authors has any financial interest related to this study to disclose.

References

1. Novoselov KS, Geim AK, Morozov SV, et al. Electric field effect in atomically thin carbon films. Science. 2004;306(5696): 666-669.
2. Ferrari AC, Bonaccorso F, Fal'ko V, et al. Science and technology roadmap for graphene, related two-dimensional crystals, and hybrid systems. Nanoscale. 2015;7(11):4598-4810.
3. Chung C, Kim Y-K, Shin D, Ryoo S-R, Hong BH, Min D-H. Biomedical applications of graphene and graphene oxide. Acc Chem Res. 2013;46(10):2211-2224.
4. Sun X, Liu Z, Welsher K, et al. Nano-graphene oxide for cellular imaging and drug delivery. Nano Res. 2008;1(3):203-212.
5. Hu W, Peng C, Luo W, et al. Graphene-based antibacterial paper. ACS Nano. 2010;4(7):4317-4323.
6. Zhang L, Xia J, Zhao Q, Liu L, Zhang Z. Functional graphene oxide as a nanocarrier for controlled loading and targeted delivery of mixed anticancer drugs. Small. 2010;6(4):537-544.
7. Akhavan O, Ghaderi E. Toxicity of graphene and graphene oxide nanowalls against bacteria. ACS Nano. 2010;4(10):5731-5736.
8. Liu S, Zeng TH, Hofmann M, et al. Antibacterial activity of graphite, graphite oxide, graphene oxide, and reduced graphene oxide: membrane and oxidative stress. ACS Nano. 2011;5(9): 6971-6980.
9. Ruiz ON, Fernando KAS, Wang B, et al. Graphene oxide: a nonspecific enhancer of cellular growth. ACS Nano. 2011;5(10): 8100-8107.
10. Das MR, Sarma RK, Saikia R, Kale VS, Shelke MV, Sengupta P. Synthesis of silver nanoparticles in an aqueous suspension of graphene oxide sheets and its antimicrobial activity. Colloids Surf B Biointerfaces. 2011;83(1):16-22.
11. Santos CM, Tria MC, Vergara RA, Ahmed F, Advincula RC, Rodrigues DF. Antimicrobial graphene polymer (PVK-GO) nanocomposite films. Chem Commun (Camb). 2011;47(31):8892-8894.
12. Liao K-H, Lin YS, Macosko CW, Haynes CL. Cytotoxicity of graphene oxide and graphene in human erythrocytes and skin fibroblasts. ACS Appl Mater Interfaces. 2011;3(7):2607-2615.
13. Wojtoniszak M, Chen X, Kalenczuk RJ, et al. Synthesis, dispersion, and cytocompatibility of graphene oxide and reduced graphene oxide. Colloids Surf B Biointerfaces. 2012;89:79-85.
14. Liu S, Hu M, Zeng TH, et al. Lateral dimension-dependent antibacterial activity of graphene oxide sheets. Langmuir. 2012;28(33): 12364-12372.
15. Mangadlao JD, Santos CM, Felipe MJ, de Leon AC, Rodrigues DF, Advincula RC. On the antibacterial mechanism of graphene oxide (GO) Langmuir-Blodgett films. Chem Commun (Camb). 2015;51(14):2886-2889.
16. Akhavan O, Ghaderi E, Esfandiar A. Wrapping bacteria by graphene nanosheets for isolation from environment, reactivation by sonication, and inactivation by near-infrared irradiation. J Phys Chem B. 2011;115(19):6279-6288.
17. Hui L, Piao J-G, Auletta J, et al. Availability of the basal planes of graphene oxide determines whether it is antibacterial. ACS Appl Mater Interfaces. 2014;6(15):13183-13190.
18. Zhang L, Xia J, Zhao Q, Liu L, Zhang Z. Functional graphene oxide as a nanocarrier for controlled loading and targeted delivery of mixed anticancer drugs. Small. 2010;6(4):537-544.
19. Sasidharan A, Panchakarla LS, Chandran P, et al. Differential nano-bio interactions and toxicity effects of pristine versus functionalized graphene. Nanoscale. 2011;3(6):2461-2464.
20. Wang K, Ruan J, Song H, et al. Biocompatibility of graphene oxide. Nanoscale Res Lett. 2011;6:1-8.
21. Chang Y, Yang S-T, Liu JH, et al. In vitro toxicity evaluation of graphene oxide on A549 cells. Toxicol Lett. 2011;200(3): 201-210.
22. Sasidharan A, Panchakarla LS, Sadanandan AR, et al. Hemocompatibility and macrophage response of pristine and functionalized graphene. Small. 2012;8(8):1251-1263.
23. Pinto AM, Gonçalves IC, Magalhães FD. Graphene-based materials biocompatibility: a review. Colloids Surf B Biointerfaces. 2013;111:188-202.
24. Yang K, Li Y, Tan X, Peng R, Liu Z. Behavior and toxicity of graphene and its functionalized derivatives in biological systems. Small. 2013;9(9-10):1492-1503.
25. Seabra AB, Paula AJ, de Lima R, Alves OL, Durán N. Nanotoxicity of graphene and graphene oxide. Chem Res Toxicol. 2014;27(2):159-168.
26. Zhang W, Yan L, Li M, et al. Deciphering the underlying mechanisms of oxidation-state dependent cytotoxicity of graphene oxide on mammalian cells. Toxicol Lett. 2015;237(2): 61-71.
27. Paul W, Sharma CP. Blood compatibility and biomedical applications of graphene. Trends Biomater. Artif. Organs. 2011;25(3): 91-94.
28. Singh SK, Singh MK, Nayak MK, et al. Thrombus inducing property of atomically thin graphene oxide sheets. ACS Nano. 2011;5(6):4987-4996.
29. Jastrzębska AM, Kurtycz P, Olszyna AR. Recent advances in graphene family materials toxicity investigations. J Nanopart Res. 2012;14(12):1320-1341.
30. Guo X, Mei N. Assessment of the toxic potential of graphene family nanomaterials. J Food Drug Anal. 2014;22(1):105-115.
31. Estrade-Szwarckopf H. XPS photoemission in carbonaceuous materials: a "defect" peak beside the asymmetric peak. Carbon. 2004;42(8-9):1713-1721.
32. Rozada R, Paredes JI, Villar-Rodil S, Martínez-Alonso A, Tascón JM. Towards full repair of defects in reduced graphene oxide films by two-step graphitization. Nano Res. 2013;6(3): 216-233.
33. Yang D, Velamakanni A, Bozoklu G, et al. Chemical analysis of graphene oxide films after heat and chemical treatments by X-ray photoelectron and micro-Raman spectroscopy. Carbon. 2009;47(1):145-152.